Linear and Nonlinear Electrochemical Impedance Spectroscopy for Lithium-ion Batteries

Matthew D. Murbach

A dissertation
submitted in partial fulfillment of the
requirements for the degree of

Doctor of Philosophy

University of Washington

2018

Reading Committee:

Daniel T. Schwartz, Chair
David A. C. Beck
Venkat R. Subramanian

Program Authorized to Offer Degree:
Chemical Engineering

University of Washington

Abstract

Linear and Nonlinear Electrochemical Impedance Spectroscopy for Lithium-ion Batteries

Matthew D. Murbach

Chair of the Supervisory Committee:
Professor Daniel T. Schwartz
Chemical Engineering

Whole cell, *in situ* diagnostics capable of sensitive and selective characterization of the physicochemical processes governing lithium-ion battery performance are critical for improving battery safety, cost, and lifetime. Electrochemical impedance spectroscopy (EIS) is a powerful and widely used technique for noninvasively characterizing many electrochemical systems including lithium-ion batteries; however, the restriction of probing only the linearized physics artificially limits the information that can be extracted from an inherently nonlinear system. Here we describe a natural extension to EIS, called nonlinear EIS (NLEIS), which can break the degeneracy of linearization and provide complementary information to EIS.

In this work, the initial theoretical and experimental groundwork for NLEIS as a powerful characterization method for lithium-ion batteries is developed. A physics-based mathematical model describing the fundamental (linear) and higher harmonic (nonlinear) response of a lithium-ion battery is used to analyze the first experimentally measured full-frequency second harmonic NLEIS spectra. Modeling results indicate that the information contained in NLEIS spectra compliments EIS characterization of charge-transfer kinetics (through the sensitivity of the second harmonic to reaction symmetry) and thermodynamic and transport processes (through a more distinct and sensitive low frequency response). Experimentally, we show that NLEIS and EIS are able to characterize early degradation (<1% capacity loss)

in commercially available (1.5 Ah LiNMC|C) batteries. While NLEIS shows that fresh cells have high symmetry charge transfer ($\alpha_a = \alpha_c = 0.5$), a shift toward kinetics that favor oxidation on the positive electrode ($\alpha_{a,pos} > 0.5$, $\alpha_{c,pos} < 0.5$) occurs as the cell is aged. Furthermore, modeling insights and experimental measurements of linear EIS and second harmonic NLEIS spectra at different states-of-charge (SoC) and states-of-health (SoH) suggest that combining EIS and NLEIS shows promise for improved battery characterization, parameter estimation, and model validation.

To accelerate the adoption and reproducibility of experimental EIS and NLEIS analysis, several open software tools are also presented in this work. In particular, the Randles equivalent circuit model is extended to account for nonlinearities in charge transfer kinetics and thermodynamics to create a second harmonic NLEIS equivalent circuit. We show that EIS and NLEIS Randles circuits can be used to easily capture reaction asymmetry via the ratio of arc widths in the linear EIS and second harmonic NLEIS spectra. Analysis of experimental EIS and NLEIS measurements at different SoC for an aged, commercially available battery indicate that positive electrode charge transfer is more asymmetric at low SoCs ($\alpha_{a,pos}^{50\%\ \mathrm{SoC}} = 0.49$, $\alpha_{a,pos}^{10\%\ \mathrm{SoC}} = 0.68$). We also describe a web-based platform, the ImpedanceAnalyzer, for the easy-to-use estimation of physics-based parameters from experimental linear EIS spectra. We show that an a priori computed dataset can be used to quickly and robustly provide a best-matching spectrum that can be further explored with interactive visualizations or local parameter optimization. A global sensitivity analysis shows the increased sensitivity and complementary information content of second harmonic NLEIS spectra. The implications of NLEIS as a sensitive, whole-cell, *in situ* diagnostic for studying typically hard to detect degradation modes, such as lithium plating, are also discussed.

TABLE OF CONTENTS

LIST OF FIGURES

LIST OF TABLES

ACKNOWLEDGMENTS

I'd like to thank the many, many people who have supported me throughout the course of graduate school. In particular, I want to start by thanking my committee members Dan Schwartz (Chair), David Beck, Venkat Subramanian, and Devin MacKenzie for the advice and feedback (and for being flexible in scheduling!).

An extra thank you to Dan Schwartz for the inspiration and mentorship. Your enthusiasm for electrochemistry, for clean energy, for science is truly infectious. Thank you for the guidance. I may have caught the can't-say-no "disease" from you, but I've also been incredibly fortunate in the opportunities I've had in my time here.

Another huge thank you to all the friends I've made throughout the course of graduate school. You've been an amazing support group through all the "wonderful" ups and downs of grad school. I'm forever grateful for those before me who made Seattle feel welcome (Trevor, Elisa, Ed, Willy, Kelly, Matt, Honorio, Andrew, Janet, John, Mark, Greg), those who I got to know so well in our cohort (Barry, David, Jac, Karl, Jessica, Jared, Erik, Michael, Kiran, Joe D., and Manan), and those who joined the department after me who have made these last few years great (Victor, Monica, Neal, Elena, Evan, Yi-Ting, Jerry, Yanbo, Erica, Linnette, Brian, Jon, Wes).

I'm particularly thankful to Trevor Braun for welcoming me to the group, introducing me to the magic of electrochemistry, and setting a truly fantastic example for me to try to work towards. I'm also thankful for the chance to work with Victor Hu these last two years — thanks for bringing the fun back both in and out of the lab!

Special thanks for last:

To my family — my sister, Cherie, my parents, Dave and Cindy, all the cousins and family. The visits, the cousin's weeks, the phone calls all served as constant reminders that I had the support to get through. I am truly thankful for the love.

To Jenny, I can't imagine having done this without your constant support, confidence boosts, jokes, and love. I'm beyond excited to marry you in a few weeks.

DEDICATION

To my parents, thank you for everything.

Chapter 1
INTRODUCTION

Electrochemical impedance spectroscopy (EIS) is a commonly used technique for the noninvasive characterization of many electrochemical systems.[1–3] EIS works by applying a small-amplitude current or voltage perturbation to an electrochemical cell and measuring the voltage or current response. In a galvanostatic (current-controlled) EIS experiment, an input current, $\tilde{I}(t) = \Delta I \cos(\omega_1 t)$, of perturbation amplitude, ΔI, and frequency, ω_1, is applied and the resulting voltage response, $\tilde{V}(t) = \Delta V \cos(\omega_1 t + \theta)$, with amplitude, ΔV, and phase shift, θ, is measured. The relationship between input and output signals as a function of the input frequency, ω_1, is defined as the impedance,

$$Z(\omega_1) = \frac{\tilde{V}(t)}{\tilde{I}(t)}. \tag{1.1}$$

The impedance, $Z(\omega_1)$, can be written in polar coordinates with a magnitude and phase, $Z(\omega_1) = |Z(\omega_1)|e^{j\theta}$, or Cartesian coordinates with real and imaginary components, $Z(\omega_1) = Z'(\omega_1) + jZ''(\omega_1)$.

In general, the impedance of an electrochemical system is frequency dependent and the response over a wide range of frequencies is measured in a single experiment to capture an impedance spectrum, $Z(\omega_1)$. The impedance spectrum is a powerful signature of an electrochemical system because the varying frequencies can separate the complex overall system response into individual physicochemical processes via their characteristic timescales. That is, the impedance response is governed by the physical processes which occur on the same timescale as the perturbation frequency; phenomena that occur faster than the input perturbation will have reached their steady state values, while slower processes will not

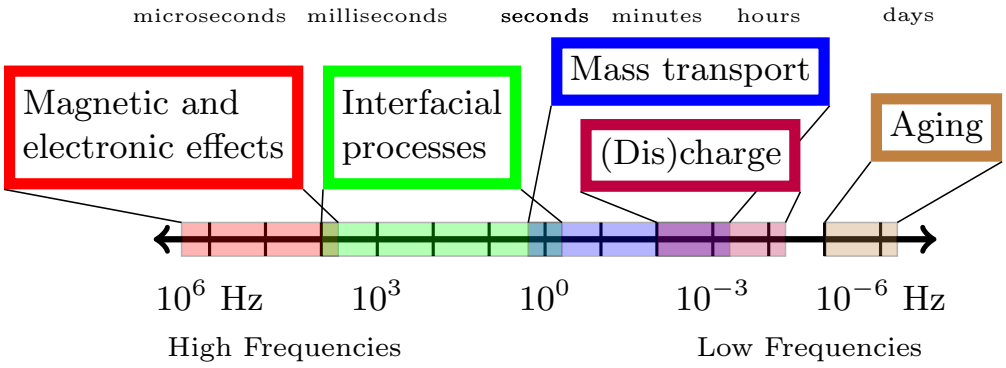

Figure 1.1: Timescales in a lithium-ion battery

have time to respond. The separation of processes via their characteristic timescales makes EIS a powerful tool for studying physical phenomena such as electron transport,[4,5] reaction rates and mechanisms,[6,7] intercalation processes,[8] mass transport,[9,10] as well as electrode structure.[11,12] In addition to characterizing the fundamental physical processes occurring in a system, the noninvasive and sensitive signature of impedance spectra are useful in prognostic applications such as fuel cell health estimations[13,14] or prediction of remaining useful lifetime in batteries.[15,16]

1.1 Electrochemical impedance of lithium-ion batteries

Lithium-ion batteries are complex electrochemical systems with many different materials, interfaces, and physicochemical processes performing in concert to efficiently charge, store, and discharge energy over many thousands of cycles. Characterizing each of the kinetic, mass-transport, and thermodynamic processes and their contribution to the overall battery response is important for both improving battery materials as well as monitoring and operating commercial batteries more effectively. The separation of processes via characteristic timescales makes EIS a good tool for characterizing lithium-ion batteries. A graphical representation of the range of timescales in a lithium-ion battery, is shown in Figure 1.1. Of particular interest to EIS measurements, the interfacial processes — lithium intercalation into the electrodes, degradative side reactions, double-layer capacitance, etc. — typically occur

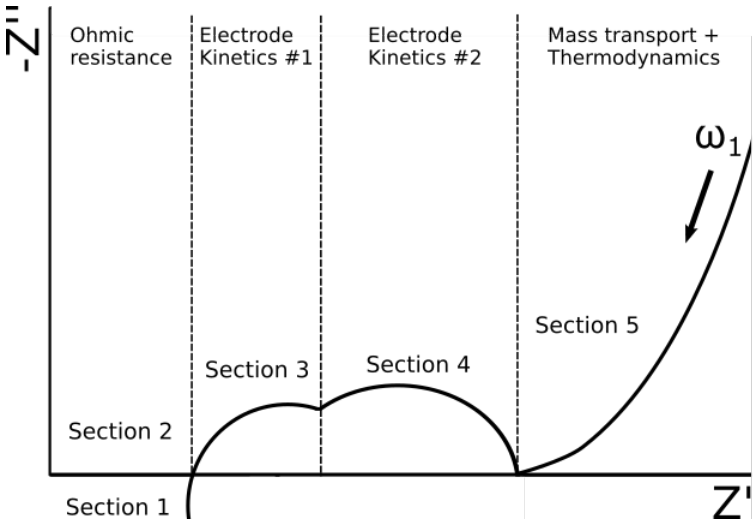

Figure 1.2: Typical EIS spectrum for Li-ion battery

on a faster timescale than the mass transport and thermodynamics of the system. Thus, in a typical EIS spectrum for a lithium-ion battery (Figure 1.2), there are several characteristic shapes in the Nyquist diagram. At low frequencies, mass transport and thermodynamics dominate the system response and a low-frequency "tail" (Section 5) is measured. As the perturbation frequency is increased, the transport in the system is slow relative to the interfacial kinetics and one or more depressed mid-frequency arcs (Sections 3 and 4) linked to interfacial processes are typically found. At high enough frequencies, the double-layer capacitance shorts out any diffusion or intercalation of lithium ions, and the battery (ideally) acts as a resistor with a purely real impedance equal to the internal (ohmic) resistance (Section 2). Experimental noise at very high frequencies in real systems caused by inductance in the wire leads often means the spectrum has a positive imaginary impedance (Section 1). While a real battery is rarely as well separated in timescales as Figure 1.2, the varying sensitivities to different physical phenomena as the frequency is swept can be incredibly useful in characterizing battery behavior.

Typically, the experimental measurement of an impedance spectrum is relatively straightforward and EIS is a standard option on commercially available potentiostats. The analysis

of the resulting data, however, can vary widely from qualitative to quantitative. Qualitative analysis of EIS spectra generally involves assessing the shape of Nyquist plot features to determine the relative importance of different physicochemical processes.[17,18] In contrast, quantitative analysis relies on fitting a model to the data in order extract values for specific thermodynamic, transport, and/or kinetic parameters. The use of small-amplitude perturbations ensures that the system response is linear and allows for the application of a linear model to interpret impedance spectra. Fitting an equivalent circuit model is particularly common in the quantitative analysis of experimental spectra. In an equivalent circuit for an electrochemical system, the overall current flowing through the system and the associated voltage polarizations are attributed to a linear combination of circuit elements. These elements can be combined in series (equal current flow) or parallel (equal voltage drop). Moreover, circuit elements can be passive elements like resistors and capacitors, more complex transfer functions derived from the solution of linearized equations governing mass transport or multi-step reactions, or even empirical functions that fit the data well.[3]

While the linear nature of EIS makes analysis with equivalent circuits straightforward, it restricts EIS to probing only the linear regime despite the inherent *nonlinear* nature of many electrochemical systems. Linearization intrinsically reduces the information content of a given EIS measurement. One practical consequence of this information loss is model degeneracy, in that, one EIS dataset can be represented equally well by different physical models[19] and different circuit analogs.[20]

1.2 Nonlinear Electrochemical Impedance Spectroscopy (NLEIS)

A natural extension to EIS that breaks this linearization is to use moderate-amplitude perturbations to drive the system into a weakly-nonlinear response. In the weakly-nonlinear regime, a single-frequency sinusoidal input of current or voltage produces one or more small higher harmonics of the fundamental frequency in the output Fourier spectrum. Harmonics in the output signal have often been treated as evidence of a "corrupted" linear response to be eliminated from EIS measurements;[21–26] however, harmonics are signatures of the nonlinear-

ity in the physicochemical phenomena and, given the right framework for interpretation, can provide additional sensitivity and information about the system's internal state.[27] In fact, the information-rich signatures of nonlinearly generated harmonics are the basis of entire fields such as nonlinear optics.[28,29]

Early research into characterizing the nonlinearity of electrochemical systems using *ac* techniques focused on measuring changes in the impedance response as the perturbation amplitude is increased.[30–36] In particular, Darowicki and Orlikowski focused on simultaneously determining corrosion current and Tafel coefficients by measuring the distortion of the fundamental frequency impedance spectrum.[31,33] A challenge with probing nonlinear effects by measuring the changes in the fundamental impedance spectra was the necessity of using large-amplitude perturbations (100s of mV) in order to produce a measurable change on top of the large fundamental frequency signal. As a result, the system was not in the weakly nonlinear regime and analysis relying on Taylor-series expansions of the corrosion current could no longer be reliably used.[37]

These early challenges highlight that amplitude selection is just as crucial for nonlinear impedance techniques as for ensuring linearity in EIS measurements. That is, driving a system into the weakly-nonlinear regime enables a theoretical framework for modeling the harmonic response, while the use of larger-amplitude perturbations makes physics-based interpretation more difficult. For example, Devay and MeÌĄszaÌĄros derived the theoretical weakly-nonlinear harmonic response of a corrosion system and showed that the polarization resistance and Tafel coefficients could be accurately measured via a single frequency measurement capturing the first three harmonics.[38,39]

The measurement of the nonlinear response at a single frequency had the significant benefit of being faster than a full frequency impedance spectrum; however, in complex systems with different kinetic, transport, and thermodynamic processes choosing the correct amplitude frequency remains a challenge.[40] Despite these challenges, the measurement of single frequency nonlinear response has been used as a characteristic signature for chemical sensors.[41–45]

More recently, full-spectrum nonlinear analysis techniques and a theoretical framework for analyzing the harmonic spectra have been employed to study a wide variety of electrochemical systems.[19,46–51] Many of these techniques take advantage of the underlying structure of the weakly nonlinear response to derive mathematical models for the harmonic response. In particular, Medina and Schwartz laid out an elegant formalism for frequency domain mathematical modeling and experimental analysis of the nonlinear dynamics of oscillating flow in a uniform-injection cell.[48] Wilson et al. relied on a similar analytic-numeric formulation to distinguish between several proposed reaction mechanisms for SOFC cathodes which were degenerate in the linear regime.[19] The work in this thesis also takes advantage of the structure of a weakly-nonlinear response to develop physics-based mathematical models in order to interpret experimentally measurable frequency dependent dispersion coefficients in lithium-ion batteries. Mathematical analysis based on the Volterra kernel, exploits the same underlying structure of the weakly-nonlinear regime, and has also been used to model harmonic response of fuel cells.[50,51]

A different, large-amplitude method has recently been used by Harting et al. to study lithium-ion battery performance.[52–55] It should be noted that (like the early work of Darowicki[31,33,37]) neither the Fourier-Perturbation analysis used in this work[19,46–49] or the Volterra series approach[50,51] for theoretical modeling are applicable outside the weakly nonlinear regime.

1.3 Physics-based analysis of impedance spectra

While EIS is a widely utilized technique, NLEIS has historically had several perceived challenges in its widespread adoption. One potential critique is the high demand on the equipment to both generate harmonic-free, moderate-amplitude input perturbations and simultaneously measure the small harmonics (relative to the fundamental frequency) in the response. Perhaps more importantly, however, is the lack of a simple method for interpreting NLEIS spectra. That is, while EIS has equivalent circuits (and software for performing the fitting is provided with many instruments), NLEIS has required using more sophisticated methods

to quantitatively analyze the resulting harmonics. An alternative to the fitting of equivalent circuits in the qualitative analysis of experimental EIS and NLEIS spectra is the direct application of a physics-based electrochemical model. Many years of electrochemical modeling research have laid the groundwork for the physics-based analysis of impedance in a wide variety of fields including corrosion,[6] hydrodynamic systems,[46,56] fuel cells,[19,57] and lithium-ion batteries.[58–60] Parameter estimation by fitting a physics-based model to experimental EIS data is complicated by the fact that electrochemical models often contain a combination of coupled differential equations, algebraic equations, and dozens of unknown parameters. For complex physics-based models, convergence to a global best fit is rarely assured, even with an excellent initial guess for the unknown parameters. As a result, parameter estimation methods often need to rely on many independent measurements to drastically narrow the number of fitted parameters.[61] In short, today there is gap between the desire to use physics-based models to estimate parameters in EIS and NLEIS, and the actual (routine) use of physics-based models for parameter estimation from data.

In particular, while there are thousands of papers using the pseudo-two-dimensional (P2D) battery model and three of the top seven most cited papers of all time in the *Journal of the Electrochemical Society* (as of June 2018) are the foundational papers, only a handful of examples of using these physics based models for the analysis of experimental impedance spectra exist. The earliest uses of physics-based, lithium-ion battery impedance models have been to inform the analysis of experimental EIS data. For example, Doyle et al.[59] used physics-based EIS simulations to show that the low frequency portion of a lithium-ion battery's impedance spectrum appears (qualitatively) to be interpretable as a Warburg impedance, but using a Warburg plot can produce erroneous (quantitative) diffusivity estimates. Subsequently, additional physics has been added to the original P2D model to aid in the interpretation of EIS data. For example, a surface oxide model was added to the positive electrode particles by Dees et al.[61] to understand the increase in interfacial impedance with aging of $LiNi_{0.8}Co_{0.15}Al_{0.05}O_2$-based (NCA) positive electrodes. Abraham et al.[62] extended the model further to interpret the changing impedance response at different voltages in NCA

electrodes.

To truly utilize the value of these models, however, a different, more open, approach to the integration of modeling and experimental analysis is required. In particular, the development of open-source models that can be used as diagnostic tools for experimental data has the potential to significantly improve the reproducibility of and accelerate both modeling and experimental research efforts.

1.4 Electrochemistry + Data Science

Incorporating data science tools into the classical Chemical Engineering toolbox has the potential to change the types of questions that can be asked in the course of research, speed up the iterative processes required to tackle hard problems, and enable more effective sharing of results.[63] While popular usage of the term "data science" is relatively new, the underlying statistical analysis, visualization, and data management skills have long been useful to Chemical Engineers. In particular, using statistical models to better predict variables of interest and elucidate structure in a set of data have been key to Chemical Engineering research for decades.

For some perspective on this history, just within the Chemical Engineering department at the University of Washington, there are several examples of statistical learning methods being developed and used over the past 20 years. Professor N. Lawrence Ricker's research on process control led to his work in developing algorithms for partial least squares (PLS) regression.[64] PLS regression is an example of a supervised machine learning method in which inputs are mapped to outputs using a labeled set of input-output pairs.[65] Additionally, in a move towards reproducibility and open science, the new, faster algorithm for PLS in continuum regression was made available alongside the paper. Similarly, research in Professor Dave Castner's group has long used multivariate analysis techniques to characterize surface analytical data.[66] In 2002, Sanni et al. showed the effectiveness of classifying proteins from ToF-SIMS spectra using both principal component analysis (PCA) and neural networks (NN).[67] Around the same time, Professor Schwartz' research group was also using principal

component analysis (PCA) to understand the underlying structure in Raman spectra.[68] PCA is an example of an unsupervised machine learning algorithm which, given a set of inputs, attempts to find "interesting" patterns in the data.[65] From these examples in the early 2000s to the ongoing research leveraging machine learning,[69,70] big datasets,[71–73] and data visualization tools,[74] Chemical Engineers at the UW are continuing to applying the power of computing and big data to the advancement of chemical engineering.

In addition to developing the initial models and experimental procedures for NLEIS for lithium-ion batteries, the work presented here attempts to move beyond the deterministic approach (systematically varying a single parameter to understand it's effects, for example) commonly employed in the physics-based modeling community. By leveraging the statistical analysis, visualization, and data management toolbox commonly referred to as data science, this work aims to build open-source tools and datasets, improve the sharing of research with interactive visualizations and reproducible publishing practices, and approach complex problems from a non-deterministic point of view. Finally, cultivating a community around data science in the electrochemical research community has also been a goal at both the University of Washington and beyond through the organization of data science tutorials and two ECS Data Science Hack Week events.

1.5 Thesis Roadmap

The work in this thesis largely contributes to two broad themes: (i) the development of NLEIS as a characterization technique for lithium-ion batteries and (ii) a focus on making physics-based analysis of experimental impedance spectra easier to use in an open and reproducible way. The first two chapters describe the initial development of both the experimental procedures and modeling framework for measuring and interpreting the application of NLEIS to lithium-ion batteries. The next two chapters focus on building the framework for open and reproducible analysis of linear and nonlinear impedance spectra. In particular, Chapter 2 describes an extension of the widely used pseudo-two-dimensional (P2D) model to include the higher harmonic response of a lithium-ion battery subjected to moderate-amplitude si-

nusoidal current modulations. The analytic-numerical approach in this work enables the computationally efficient evaluation of EIS and NLEIS impedance spectra. The effects of kinetic, transport, and thermodynamic processes on EIS and NLEIS spectra were explored using this model for the linear as well as second- and third-harmonic response. Interestingly, the results show the strong dependence of the second harmonic on the symmetry of the system and that, by breaking degeneracy, NLEIS has the potential to increase the number of physicochemical parameters that can be assessed in experiments similar in complexity to standard EIS measurements. Chapter 3 then describes the first, full-spectrum experimental measurements of NLEIS spectra for lithium-ion batteries. Working with Victor Hu, we show that the measurement of lithium-ion battery NLEIS spectra is straightforward using commercially available potentiostat/FRA instruments. The effects of state-of-charge as well as state-of-health on commercial LiNMC-graphite batteries are presented and the model developed in Chapter 2 is used to begin understanding these effects. In the process of developing and sharing our work on NLEIS, it became clear that sophisticated, reproducible analysis of impedance spectra was an important topic for the electrochemical community. Chapter 4 describes an open-software platform, the ImpedanceAnalyzer, for easily integrating more sophisticated, physics-based analysis into the experimental impedance analysis workflow. In this work, a large dataset (38,800 spectra — 2.9M total computations) of linear EIS and nonlinear harmonic spectra over a wide frequency and parameter range were generated. The dataset of linear impedance spectra was used in the ImpedanceAnalyzer to find the best matches to experimental data. Section 5.1 explores the use of this dataset-approach to calculate global parameter sensitivity. Section 5.2 leverages the above modeling and experimental insights to present the initial results and development of an equivalent circuit model for the second harmonic NLEIS response. Finally, Chapter 6 explores the overall impact of impedance-based diagnostics and open-software tools as well as future research opportunities.

Chapter 2

SIMULATING THE NONLINEAR IMPEDANCE RESPONSE FOR LITHIUM-ION BATTERIES USING THE PSEUDO-TWO-DIMENSIONAL MODEL

Note: this chapter was published as an article

- Matthew D. Murbach and Daniel T. Schwartz. Extending Newman's Pseudo-Two-Dimensional Lithium-Ion Battery Impedance Simulation Approach to Include the Nonlinear Harmonic Response. *Journal of The Electrochemical Society*, 164(11):E3311–E3320, 2017. DOI: 10.1149/2.0301711jes

Abstract

The pseudo-two-dimensional (P2D) model of lithium-ion batteries couples a volume-averaged treatment of transport, reaction, and thermodynamics to solid-state lithium diffusion in electrode particles. Here we harness the linear and nonlinear physics of the P2D model to evaluate the fundamental (linear) and higher harmonic (nonlinear) response of a $LiCoO_2|LiC_6$ cell subject to moderate-amplitude sinusoidal current modulations. An analytic-numeric approach allows the evaluation of the linearized frequency dispersion function that represents electrochemical impedance spectroscopy (EIS) and the higher harmonic dispersion functions we call nonlinear electrochemical impedance spectroscopy (NLEIS). Base case simulations show, for the first time, the full spectrum second and third harmonic NLEIS response. The effect of kinetic, mass-transport, and thermodynamic parameters are explored. The nonlinear interactions that drive the harmonic response break some of the degeneracy found in linearized models. We show that the second harmonic is sensitive to the symmetry of the charge transfer reactions in the electrodes, whereas EIS is not. At low frequencies, NLEIS probes aspects of the cell thermodynamics that are not accessible with EIS. In short, NLEIS has the potential to increase the number of physicochemical parameters that can be assessed in experiments similar in complexity to standard EIS measurements.

2.1 Introduction

Electrochemical impedance spectroscopy (EIS) is a commonly utilized tool for the noninvasive analysis of a wide range of electrochemical systems. Using a sufficiently small perturbation amplitude simplifies the interpretation of the impedance response because the system under analysis can be approximated as linear.[2,3] The condition of linearity and ease of fitting equivalent circuit analogs has led to the widespread adoption of EIS for both characterization[76–78] and prognostic[15,16,79] applications within lithium-ion battery research. In particular, EIS has been used to garner insight into important physicochemical processes including the growth of the solid electrolyte interphase (SEI) layer,[80] mass transfer and kinetics in electrode materials,[81] as well as other degradative and capacity loss mechanisms.[82] The challenge with EIS, however, is that the analysis is restricted to probing the linear regime, despite the inherently nonlinear nature of the electrochemical system. Fundamentally, linearization reduces the information content of a given EIS measurement. The consequence of linearization is model degeneracy, in that, one EIS dataset can be represented equally well by different physical models[19] and different circuit analogs,[20] because of the loss of information inherent with linearization. This degeneracy and loss of information may be an especially important limitation for the study of lithium-ion batteries if we hope to carefully dissect degradative interfacial processes.[83,84]

The issue of linear EIS model degeneracy and information loss is particularly challenging for sealed batteries. Analytical solutions for the pseudo-two-dimensional (P2D) model impedance response under stationary conditions show that linearized EIS is unable to uniquely determine many of the model parameters needed for simulating charge-discharge curves.[85,86] For example, the anodic and cathodic transfer coefficients, α_a and α_c, respectively, cannot be uniquely determined; only the sum $(\alpha_a + \alpha_c)$ appears in the linearized solution. Changes to the battery potential (state of charge) do not alter the inaccessibility of unique transfer coefficients. Alternative ways to measure unique transfer coefficients using EIS, such as passing a mean current that drives the electrode kinetics into the Tafel

regime, introduce the challenge of maintaining a stationary state during EIS measurements in a sealed cell.

An approach that breaks some of the degeneracy of linearized EIS without violating the requirement for stationarity is the use of moderate-amplitude current modulations around a zero-mean current. Moderate-amplitude modulations are used to drive a weakly nonlinear response, as evidenced by higher harmonics in the frequency response of the system. Typically, higher harmonics in impedance experiments have been treated as noise, to be eliminated as a way of ensuring the linearity of EIS measurements.[21,23–25] However, measuring the nonlinear harmonic response of an electrochemical system has been used to study corrosion,[31,87,88] fuel cells,[19,49,50] and mass transport controlled hydrodynamic systems[46–48] as well as in chemical sensing applications.[41–43] The increased informational power of nonlinear EIS (NLEIS) measurements enabled Wilson et al. to distinguish between physical models which were degenerate in the linear regime,[19] while Nakata et al. used the sensitivity of the nonlinear response to distinguish between different chemical targets for improved sensor selectivity.[42]

Extending EIS to probe the full-spectrum nonlinear response requires a more sophisticated approach than fitting lumped-parameter equivalent circuit analogs. Physics-based models of the full electrochemical system offer the flexibility and interpretability required for a meaningful analysis. Here we extend the P2D impedance model developed by Newman et al.[58,59] to include the linear and nonlinearly-generated higher order harmonic response generated by a lithium-ion battery system. As with EIS measurements, NLEIS is a "local" probe of the battery around a single state of charge, so EIS and NLEIS experiments will typically involve a sequence of measurements at various open circuit potentials (states of charge) to parameterize the full battery behavior. Later papers show that the extra information available in an NLEIS experiment comes at a modest increase in experimental difficulty. To the best of our knowledge, full-spectrum nonlinear EIS has not been applied to the study of lithium-ion batteries. Yet, the ability to distinguish between different physical models, noninvasively probe nonlinear internal states, and investigate the symmetry and reversibility

of degradative reactions make NLEIS a candidate for providing information-rich insights that can move the field forward.

2.2 The Mathematical Model

2.2.1 Pseudo-two-dimensional battery impedance model

The widely adopted P2D battery model has been a powerful tool for understanding,[89] optimizing,[90,91] and controlling[92] lithium-ion batteries for many decades. The P2D model is a physics-based representation of the coupled nonlinear mass transport, thermodynamic, and reaction processes inside a lithium-ion battery. Porous electrode theory treatment of the electrodes requires volume averaging over the particles and electrolyte pores leading to two macrohomogeneous solid- and solution-phase continua superimposed in the x direction across the cell sandwich thickness. The x direction equations are coupled to solid-phase diffusion of lithium inside the electrode particles, governed by,

$$\frac{\partial c^s}{\partial t} = \frac{1}{r^2}\frac{\partial}{\partial r}\left(D_s r^2 \frac{\partial c^s}{\partial r}\right) \tag{2.1}$$

where r is the radial distance from the center of the particle. Here we take the solid-phase diffusivity, D_s, to be independent of concentration in the solid, c^s.

The concentration of lithium in the electrode particles is coupled to the interfacial flux from faradaic charge transfer by the boundary condition at the solid-solution interface, $r = R_p$,

$$-D_s \frac{\partial c^s}{\partial r} = j_f \tag{2.2}$$

where we assume Butler-Volmer kinetics,

$$j_f = \frac{i_0}{F}\left[\exp\left(\frac{\alpha_a F}{RT}\eta\right) - \exp\left(\frac{-\alpha_c F}{RT}\eta\right)\right]. \tag{2.3}$$

The total interfacial flux, j, also has a non-faradaic Helmholtz double layer capacitive

contribution, j_{dl},

$$j = j_f + j_{dl} \tag{2.4}$$

where

$$j_{dl} = \frac{C_{dl}}{F}\frac{\partial\left(\varphi^s - \varphi\right)}{\partial t}. \tag{2.5}$$

Here we follow the convention of Doyle et al.[59] for a simple model of interfacial processes where the double-layer capacitance, C_{dl}, is dominated by cation rearrangement, and both C_{dl} and the exchange-current density, i_0, are independent of concentration.

The current density in the electrolyte, $\mathbf{i}_2$, is related to interfacial processes by Faraday's law,

$$\frac{\partial \mathbf{i}_2}{\partial x} = aFj \tag{2.6}$$

where a is the specific interfacial area of the electrode. Binary electrolyte theory describes the concentration in the electrolyte, c,

$$\epsilon\frac{\partial c}{\partial t} = \frac{\partial}{\partial x}\left(D_{eff}\frac{\partial c}{\partial x}\right) + a\left(1 - t_+^0\right)j \tag{2.7}$$

and solution-phase potential, φ,

$$-\kappa_{eff}\frac{\partial \varphi}{\partial x} = \mathbf{i}_2 - \frac{2\kappa_{eff}RT}{F}(1 - t_+^0)\frac{\partial \ln c}{\partial x} \tag{2.8}$$

where ϵ is the void fraction, D_{eff} is the effective diffusivity, t_+^0 is the transference number of Li^+ in the electrolyte, and κ_{eff} is the effective solution-phase conductivity. The potential in the solid, φ^s, is governed by Ohms' law,

$$-\sigma_{eff}\frac{\partial \varphi^s}{\partial x} = -I - \mathbf{i}_2 \tag{2.9}$$

where σ_{eff} is the effective conductivity in the solid-phase and I is the total current density, $-I = \mathbf{i}_1 + \mathbf{i}_2$.

Zero flux boundary conditions are taken at the positive and negative current-collectors,

$$\frac{\partial c}{\partial x} = \frac{\partial \varphi}{\partial x} = 0 \;\text{ at }\; x = 0 \;\text{ and }\; x = L \tag{2.10}$$

Current only flows in the solution- and solid-phases at the separator-electrode and electrode-current collector interfaces, respectively,

$$\mathbf{i}_2 = 0 \;\text{ and }\; -\sigma_{eff}\frac{\partial \varphi^s}{\partial x} = -I \;\text{ at }\; x = 0 \;\text{ and }\; x = L \tag{2.11}$$

$$\mathbf{i}_2 = -I \;\text{ and }\; -\sigma_{eff}\frac{\partial \varphi^s}{\partial x} = 0 \;\text{ at }\; x = l_{neg} \;\text{ and }\; x = l_{neg} + l_{sep} \tag{2.12}$$

and the solution-phase potential is set to zero ($\varphi = 0$) at the negative current collector as a reference. The equations in the separator are given by Equations 2.6-2.8 with the interfacial flux set to zero ($j = 0$). Continuity of the fluxes across the electrode/separator interfaces is maintained. In all cases, effective transport coefficients (diffusivities, conductivities) are modifications of the intrinsic transport coefficients using a Bruggeman-type tortuosity factor to account for the porous character of the medium. For example, $D_{eff} = D\epsilon^{Brugg}$ for effective diffusivity, where D is the intrinsic diffusivity, and $Brugg$ is the Bruggeman coefficient.

2.2.2 Frequency domain formulation

The governing equations described above are both coupled and nonlinear. If we assume the system of equations is stable to finite amplitude current perturbations, then nonlinear theory suggests a pure single frequency sinusoidal input perturbation will generate an output response with spectral components at the excitation frequency (fundamental or 1^{st} harmonic) and integer higher harmonics (2^{nd}, 3^{rd}, and 4^{th} harmonic of the fundamental frequency). We have shown previously that a fast-computing analytic-numeric method can be used for analyzing the linear and nonlinear response of many different electrochemical and transport-reaction systems when they are stable to finite amplitude perturbations.[19,47,48,93,94] Here we apply these methods for to the analysis of the nonlinear impedance in a lithium-ion battery

system using the above P2D equations. The key step in the fast analytic-numeric formulation is to expand all dependent variables in the governing equations and boundary condition as a complex Fourier series

$$X\left(\mathbf{x},t;\Delta I,\omega_1\right)=\mathrm{Re}\left\{\sum_{k=0}^{\infty}\tilde{X}_k\left(\mathbf{x};\Delta I,\omega_1\right)\exp\left(jk\omega_1 t\right)\right\} \tag{2.13}$$

where X denotes any of the dependent variables (c^s, c, $\mathbf{i}_2$, φ^s, and φ), $\tilde{X}_k$ are the complex Fourier coefficients, $\tilde{X}_k=\tilde{X}_k'-j\tilde{X}_k''$, for the respective dependent variables, $\mathbf{x}$ is the vector of spatial independent variables (x, r), t is time, ΔI is the current modulation amplitude, ω_1 is the fundamental frequency of the perturbation, and k is an integer that indicates the harmonic number. The notation of $X(a;b,c,\dots)$ is used to show X is the dependent variable, a is an independent variable, and $b,c,\dots$ are parameters.

For the weakly nonlinear, time-periodic (stationary) system studied here, the complex Fourier coefficients can be expressed by a Volterra series expansion in powers of the current modulation amplitude,

$$\tilde{X}_k\left(\mathbf{x};\Delta I,\omega_1\right)=\sum_{r=0}^{\infty}\Delta I^{k+2r}\tilde{X}_{k,k+2r}\left(\mathbf{x};\omega_1\right). \tag{2.14}$$

The resulting double-indexed complex coefficients $\tilde{X}_{k,p}\left(\mathbf{x};\omega_1\right)$ within the summation of Equation 2.14 are the key frequency dispersion coefficients for the Fourier coefficients at harmonic number, k, and order of nonlinear coupling, p. When $k=p=1$, the governing equations and boundary conditions represent the linear response of the system to infinitesimal current modulations (e.g., this is the condition Doyle et al. computed[59] to determine the traditional linear EIS of a half-cell). When $k=p=2$, the governing equations and boundary conditions represent the leading order 2^{nd} harmonic response of the system of equations to a finite perturbation, and so on. Solutions for $p>k$, represent corrections to the leading order $k=p$ solutions. Here, we ignore all correction terms and focus on the leading order ($k=p$) linear and nonlinear harmonics.

2.2.3 Computing the leading order linear and nonlinear spectra

The resulting governing equations are shown in the Appendix. Table A2.1 contains the governing equations and boundary conditions for simulating the linear impedance ($k = p = 1$) response. Tables A2.2 and A2.3 contains the sets of equations for computing the second ($k = p = 2$) and third ($k = p = 3$) harmonic responses. The higher harmonic equations contain terms which depend on the lower harmonic solutions in a hierarchical manner such that the harmonics are solved sequentially (not simultaneously). The full hierarchical set of ordinary differential equations for the first three leading order impedance harmonics was solved using the generic Coefficient Form PDE physics module in COMSOL v4.4. We chose to mesh the solid-phase equations (A2.1, A2.2, and A2.3) instead of using an analytical solution in order to have a general approach for any arbitrary concentration dependent diffusivity parameters. The mesh nodes were spaced using a geometric ratio such that there existed a high concentration of nodes at the interfaces between the solid- and solution-phases (at $r = R_{p,i}$) and at the electrode/separator interfaces (at $x = l_{neg}$ and $x = l_{neg} + l_{sep}$). Mesh refinement in the interfacial regions with high gradients was used so that the solution converged for all parameter and frequency combinations resulting in approximately 9,000 total elements. Further mesh refinement produced negligible changes in the computed results. The frequency parameter, ω_1, was varied logarithmically from 10^{-3} to 10^5 Hz with 10 points per decade. Each full spectrum (with 81 frequencies) required a computational time of around 25 minutes on a Dell Precision T1500 with an Intel Core i7 CPU @ 2.80 GHz and 8 GB RAM using a Windows 7 Professional 64-bit operating system. Parameters were updated and the results were saved to disk using the LiveLink for MATLAB version R2013b.

The leading order whole-cell impedance for the first harmonic ($k = p = 1$), the second harmonic ($k = p = 2$), and the third harmonic ($k = p = 3$) can be directly computed from the simulations as

$$\tilde{Z}_{k,p}(\omega_1) = \tilde{\varphi}^s_{k,p}(x = L; \omega_1) - \tilde{\varphi}^s_{k,p}(x = 0; \omega_1) \tag{2.15}$$

where $\tilde{\varphi}^s_{k,p}(x = L; \omega_1)$ is the computed Fourier coefficient for the solid-state potential eval-

uated at the boundary of the positive current collector ($x = L$) and $\tilde{\varphi}^{s}_{k,p}(x = 0; \omega_1)$ is the computed potential at the negative current collector ($x = 0$). These impedance coefficients are complex with both a real and an imaginary component such that $\tilde{Z}_{k,p}(\omega_1) = \tilde{Z}'_{k,p}(\omega_1) + j\tilde{Z}''_{k,p}(\omega_1)$. The double indexed coefficient $\tilde{Z}_{1,1}(\omega_1)$ is identically equal to the normal (linear) electrochemical impedance of the system. $\tilde{Z}_{2,2}(\omega_1)$ is the leading order nonlinear electrochemical impedance derived from the second harmonic of the voltage response to a pure cosine input current and $\tilde{Z}_{3,3}(\omega_1)$ is the leading order nonlinear electrochemical impedance derived from the third harmonic response.

2.3 Results and Discussion

2.3.1 Simulations of a $LiCoO_2/LiC_6$ cell

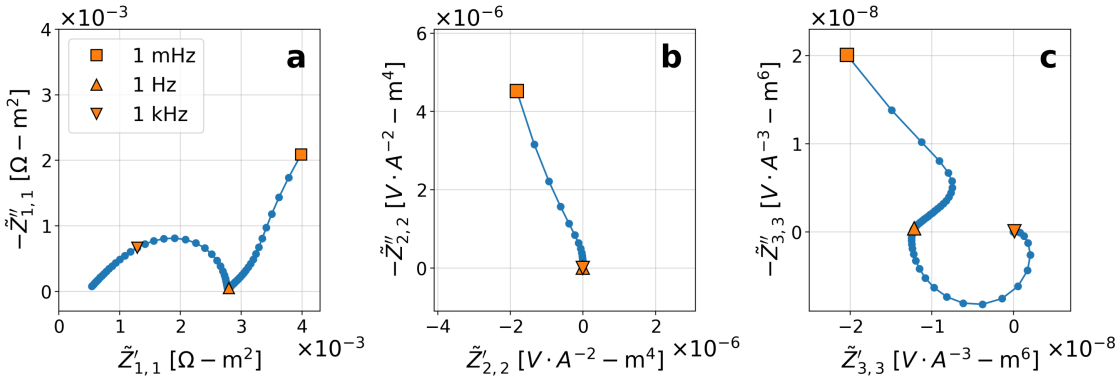

Figure 2.1: Nyquist representations of the (a) linear impedance, (b) second harmonic, and (c) third harmonic spectra for the base parameters given in Table 2.1. The high-frequency kinetics arc and low-frequency mass transport tail are characteristic of a lithium-ion battery. The lack of a second harmonic response (b) in frequencies dominated by the reaction kinetics (1 Hz to 1 kHz) is related to the typical assumption of symmetric transfer coefficients, α_a and α_c.

Figure 2.1 shows Nyquist representations of simulated impedance spectra for a typical $LiCoO_2|LiC_6$ cell using the parameters in Table 2.1. The spectra cover a wide range of frequencies from 1 mHz to 100 kHz logarithmically spaced with 10 points per decade. The linear impedance response, $\tilde{Z}_{1,1}(\omega_1)$, displays the expected characteristics of a lithium-ion

battery with a purely real ohmic resistance at high frequencies, a depressed mid-frequency arc linked to kinetic processes, and a low-frequency mass transport and thermodynamic dominated tail. The high frequency resistance is given by the sum of the ohmic resistances in each region of the cell,

$$R_{ohmic} = \left[\frac{l_{pos}}{\sigma_{eff,pos} + \kappa_{eff,pos}}\right] + \left[\frac{l_{sep}}{\kappa_{eff,sep}}\right] + \left[\frac{l_{neg}}{\sigma_{eff,neg} + \kappa_{eff,neg}}\right] \tag{2.16}$$

which evaluates to 0.467 $m\Omega - m^2$ for the parameters in Table 2.1. The typical characteristic frequencies for the kinetics of each electrode are given by,

$$\omega_{RC,i} = \frac{1}{R_{ct,i}C_{dl,i}} = \frac{(\alpha_a + \alpha_c)\, i_{0,i} F}{RT} \frac{1}{C_{dl,i}} \tag{2.17}$$

which evaluate to 1284.5 Hz and 1428.5 Hz for the negative and positive electrodes, respectively. The two electrodes have a similar contribution to this kinetic arc for the base parameters ($R_{ct,neg} = 7.79\ m\Omega - m^2$ and $R_{ct,pos} = 7.0\ m\Omega - m^2$). The characteristic frequencies for the diffusional processes in the solution- and solid-phases are given by $\omega_{D,i} = \frac{D_{eff,i}}{l_i^2}$ and $\omega_{D_s,i} = \frac{D_{s,i}}{R_{p,i}^2}$, respectively. For the base parameters, the fastest transport process (solution-phase diffusion in the separator) has a characteristic frequency of $\omega_{D,sep} = 0.33$ Hz, and the slowest process (solid-phase diffusion in the positive electrode) has a characteristic frequency of $\omega_{D_{s,pos}} = 2.5$ mHz, with characteristic transport frequencies in the negative electrode falling between them.

If the governing equations and boundary conditions representing the physics of a battery were linear, then the standard electrochemical impedance shown in Figure 2.1a would be the only response of the system to a sinusoidal current perturbation of any magnitude. However, because the P2D model is a coupled nonlinear set, it also produces a frequency-dependent higher harmonic response that we can compute. The five characteristic transport and reaction timescales, and the high frequency ohmic limit, described above, can be used to help interpret the higher order harmonic response. For instance, the second harmonic

impedance, $\tilde{Z}_{2,2}(\omega_1)$, shown in Figure 2.1b, only exhibits an appreciable signal in the characteristic frequency range for mass-transport and thermodynamics ($\omega_1 < 1$ Hz). For the base case parameters used here, there is no appreciable second harmonic response at frequencies in the reaction kinetics regime (1 Hz $-$ 10 kHz). As we will show in the next section, this lack of kinetically-driven second harmonic response is an artifact of the particular literature values used in the base case scenario (symmetric transfer coefficients on both electrodes); under more general conditions, the second harmonic is indeed sensitive to charge transfer.

The base case third harmonic spectrum, shown in Figure 2.1c, exhibits signal in the low-frequency mass-transport and thermodynamic regime as well as the mid-frequency regime dominated by the reaction kinetics, much like the standard linear electrochemical impedance spectrum shown in Figure 2.1a. For both the second and third harmonic, the nonlinear impedance asymptotes to zero in the limit of high frequencies. At high frequencies, the response of the battery is dominated by ohmic processes (that are governed by intrinsically linear physics). As a result, the nonlinear harmonics vanish at high frequencies whereas the linear impedance remains finite.

2.3.2 Effect of charge transfer symmetry

Figure 2.2a shows that changing the positive electrode anodic transfer coefficient, $\alpha_{a,pos}$, in Equation 2.3 has no effect on the linear impedance, $\tilde{Z}_{1,1}(\omega_1)$, response; all five curves lie directly on top of each other. The transfer coefficients, α_a and α_c, for a reaction are a measure of charge transfer symmetry on that electrode. The base case values of 0.5 for α_a and α_c used in Figure 2.1 for both electrodes means there is complete symmetry in oxidation and reduction on both electrodes; i.e. the magnitude of the kinetic overpotential is identical during charge and discharge. There is no intrinsic reason to assume charge transfer symmetry on either electrode. A difference in α_a and α_c for either electrode would reflect asymmetry in the charge transfer processes on that electrode. Mathematically, only the sum $(\alpha_a + \alpha_c)$ appears as a parameter in the linear $k = p = 1$ equations in Table A2.1, and that sum is unity in all cases simulated, resulting in the linear impedance being insensitive to charge transfer

Table 2.1: Basecase parameters for Li_xCoO_2|C simulations[95]

Physicochemical Parameters

Parameter	**Units**	**Value**
$C_{dl,neg}$	$\mu F/cm^2$	10
$C_{dl,pos}$	$\mu F/cm^2$	10
c_0	mol/m^3	1000
D	m^2/s	7.5×10^{-10}
$D_{s,neg}$	m^2/s	3.9×10^{-14}
$D_{s,pos}$	m^2/s	1.0×10^{-14}
$\frac{\partial U_{neg}}{\partial c^s}$	$V \cdot cm^3/mol$	-3.21
$\frac{\partial U_{pos}}{\partial c^s}$	$V \cdot cm^3/mol$	-11.67
$\frac{\partial^2 U_{neg}}{\partial c^{s2}}$	$V \cdot cm^6/mol^2$	-281.56
$\frac{\partial^2 U_{pos}}{\partial c^{s2}}$	$V \cdot cm^6/mol^2$	643.371
$\frac{\partial^3 U_{neg}}{\partial c^{s3}}$	$V \cdot cm^9/mol^3$	2222.82
$\frac{\partial^3 U_{pos}}{\partial c^{s3}}$	$V \cdot cm^9/mol^3$	-177808
$i_{0,neg}$	A/m^2	3.30
$i_{0,pos}$	A/m^2	3.67
t_+^0	—	.364
$\alpha_{a,neg}$	—	0.5
$\alpha_{a,pos}$	—	0.5
κ	S/m	0.2047
σ_{neg}	S/m	100
σ_{pos}	S/m	100

Geometric Parameters

Parameter	**Units**	**Value**
a_{neg}	m^{-1}	723600
a_{pos}	m^{-1}	885000
$Brugg$	—	4
l_{neg}	μm	88
l_{sep}	μm	25
l_{pos}	μm	80
$R_{p,neg}$	μm	2
$R_{p,pos}$	μm	2
$\epsilon_{f,neg}$	—	0.0326
$\epsilon_{f,pos}$	—	0.025
ϵ_{neg}	—	0.485
ϵ_{sep}	—	0.724
ϵ_{pos}	—	0.385

symmetry and the overlapping spectra in Figure 2.2a. Figure 2.2b shows that symmetry in charge transfer is clearly important for the second harmonic response. The solid curve in Figure 2.2b is the same case as shown Figure 2.1b, with symmetric transfer coefficients in the battery ($\alpha_a = \alpha_c = 0.5$ for both electrodes). Mathematically, symmetric transfer coefficients nullify terms in the kinetic contributions to the second harmonic ($k = p = 2$) equations. When we break the symmetry of charge transfer in Figure 2.2b — making the positive electrode have more facile oxidation ($\alpha_a > 0.5$) or more facile reduction ($\alpha_a < 0.5$) — we see a second harmonic arc arise at frequencies that correspond to kinetic processes.

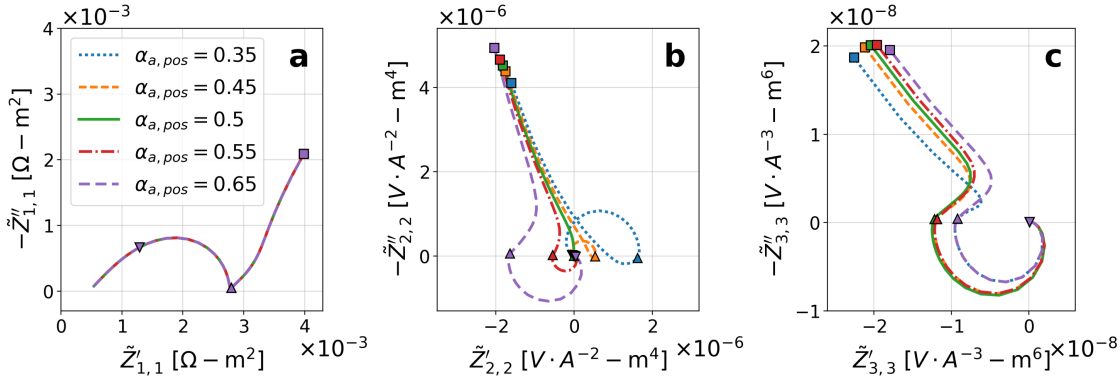

Figure 2.2: Nyquist representations of the (a) linear impedance, (b) second harmonic, and (c) third harmonic spectra for varying values of the positive electrode transfer coefficient, $\alpha_{a,pos}$. The linear response is insensitive to the transfer coefficients with all five curves superimposed upon one another. The second harmonic response is very sensitive to the asymmetry of the transfer coefficients with the presence of a kinetic arc only when $\alpha_a \neq 0.5$. While only the reaction symmetry of the positive electrode was varied here, a similar dependence on the negative electrode charge transfer symmetry also exists. The ■, ▲, and ▼ symbols indicate 1 mHz, 1 Hz, and 1 kHz, respectively.

Moreover, the direction of the kinetic arc depends on the direction of the charge transfer asymmetry. When the transfer coefficients promote more facile battery discharge ($\alpha_{a,pos} < 0.5$ and $\alpha_{a,neg} > 0.5$), the second harmonic kinetic arc moves towards the first quadrant in the Nyquist plot. In contrast, if the charge transfer asymmetry makes battery charging more facile ($\alpha_{a,pos} > 0.5$ and $\alpha_{a,neg} < 0.5$), the second harmonic response shifts to the third quadrant.

The mathematical origins of these second harmonic simulation results are given by the governing equations for $k = p = 2$. The real and imaginary oscillations in the second harmonic flux density at the solid/electrolyte interface are given by Equations A2.6r and A2.6i in Table A2.2,

$$j_f'_{2,2} = \frac{i_0 \left(\alpha_a + \alpha_c\right)}{RT} \eta'_{2,2} + \frac{i_0 \left(\alpha_a^2 - \alpha_c^2\right) F}{4R^2T^2} \left({\eta'_{1,1}}^2 - {\eta''_{1,1}}^2 \right) \tag{A2.6r}$$

and

$$j_{f\,2,2}'' = \frac{i_0\,(\alpha_a + \alpha_c)}{RT}\eta_{2,2}'' + \frac{i_0\,(\alpha_a^2 - \alpha_c^2)\,F}{2R^2T^2}\left(\eta_{1,1}'\eta_{1,1}''\right). \tag{A2.6i}$$

We find that terms involving oscillations in the overpotential at the fundamental frequency, $\eta_{1,1}$, are significantly larger than the oscillating overpotential at the second harmonic, $\eta_{2,2}$. As a result, the second term on the right-hand side (RHS) of both equations dominates the harmonic response in the second order flux density. The second term of the RHS disappears if $\alpha_a = \alpha_c$. This sensitivity to reaction asymmetry has been demonstrated experimentally by Xu and Riley[96] who studied the ferri-ferrocyanide redox couple as well as Heubner et al.[97] who used second harmonic measurements to determine the transfer coefficients in the charge transfer kinetics of $LiFePO_4$. The third harmonic shown in Figure 2.2c is also sensitive to charge transfer symmetry, but in an inverse sense from the second harmonic. The largest third harmonic kinetic loop is observed when there is symmetry and it shrinks as the symmetry is broken. It is also noteworthy that the shift in third harmonic is insensitive to whether the charge transfer asymmetry favors oxidation or reduction. Thus, Figure 2.2c produces overlapping curves for $\alpha_a = 0.45$ and $\alpha_a = 0.55$, and a different set of overlapping curves for $\alpha_a = 0.35$ and $\alpha_a = 0.65$. The results of Figure 2.2 show that there is new information to be gleaned by measuring the second and third harmonics. In the case of the transfer coefficients, the standard linear EIS spectra (Figure 2.2a) are insensitive to the specific values, whereas the second harmonic provides information about the magnitude of the asymmetry and direction (charge or discharge) that is kinetically more facile. The third harmonic just gives insights into the magnitude of the asymmetry.

2.3.3 Effect of kinetic parameters

Figure 2.3 shows the effect of the exchange current densities, $i_{0,i}$, and double-layer capacitances, $C_{dl,i}$, for the positive and negative electrodes. An asymmetric set of transfer coefficients ($\alpha_{a,neg} = 0.45$ and $\alpha_{a,pos} = 0.55$) has been assumed to ensure there is a kinetic arc in the second harmonic. The remaining discussion of individual parameter effects on the linear

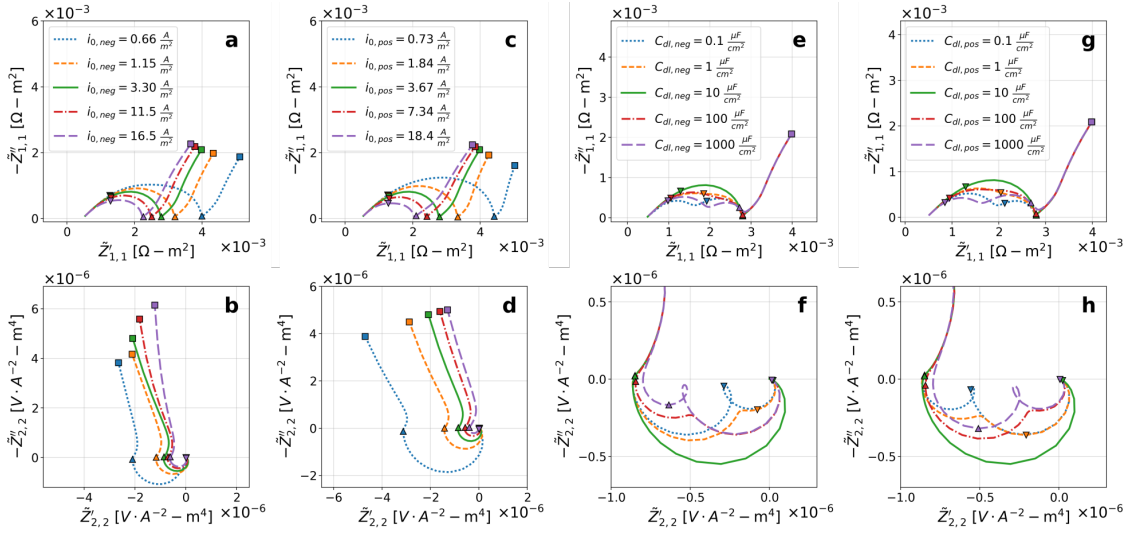

Figure 2.3: Nyquist representations of the first (a, c, e, g) and second (b, d, f, h) harmonic impedance spectra for different values of exchange current density, i_0 and double-layer capacitance, C_{dl}. The characteristic timescales of the system result in changes to these kinetic parameters only affecting the mid-frequency arc in both the first and second harmonic response. All other parameters were held constant at the values given in Table 2.1 except $\alpha_{a,neg} = 0.45$ and $\alpha_{a,pos} = 0.55$. The ■, ▲, and ▼ symbols indicate 1 mHz, 1 Hz, and 1 kHz, respectively.

and nonlinear harmonic response will focus on only the first and second harmonic, for clarity.

The linear impedance spectra in Figure 2.3a and 2.3c show the sensitivity of the kinetic arc width to the changes in exchange current density on each electrode. The increasing size of the kinetic arc is normally interpreted through the charge transfer resistances, R_{ct}, with smaller exchange current densities resulting in larger R_{ct}. Similar to the linear response, the second harmonic spectra in Figure 2.3b and 2.3d show a growing kinetic arc (at frequencies in excess of 1 Hz) as the exchange-current density is decreased. The width of the second harmonic kinetic arc is dependent on both the asymmetry of the charge transfer as well as on the value of the exchange current density.

Varying the double-layer capacitance, C_{dl}, changes the characteristic frequency for each electrode without changing the overall charge transfer resistance of the electrode. Figures 2.3e-h show that independently varying the capacitances by four orders of magnitude

separates the timescales for each electrode kinetic process and introduces distinct arcs for the two electrodes. In many ways, the linear and second harmonic show similar behaviors, namely, they go from being one distinctive arc to two clear arcs. Because the timescales between the kinetic, transport, and thermodynamic regimes are well separated for the base case parameters, changing either the exchange-current densities or the double-layer capacitances has little effect on the low frequency response of any of the harmonics for the values shown here.

2.3.4 Effect of mass transport

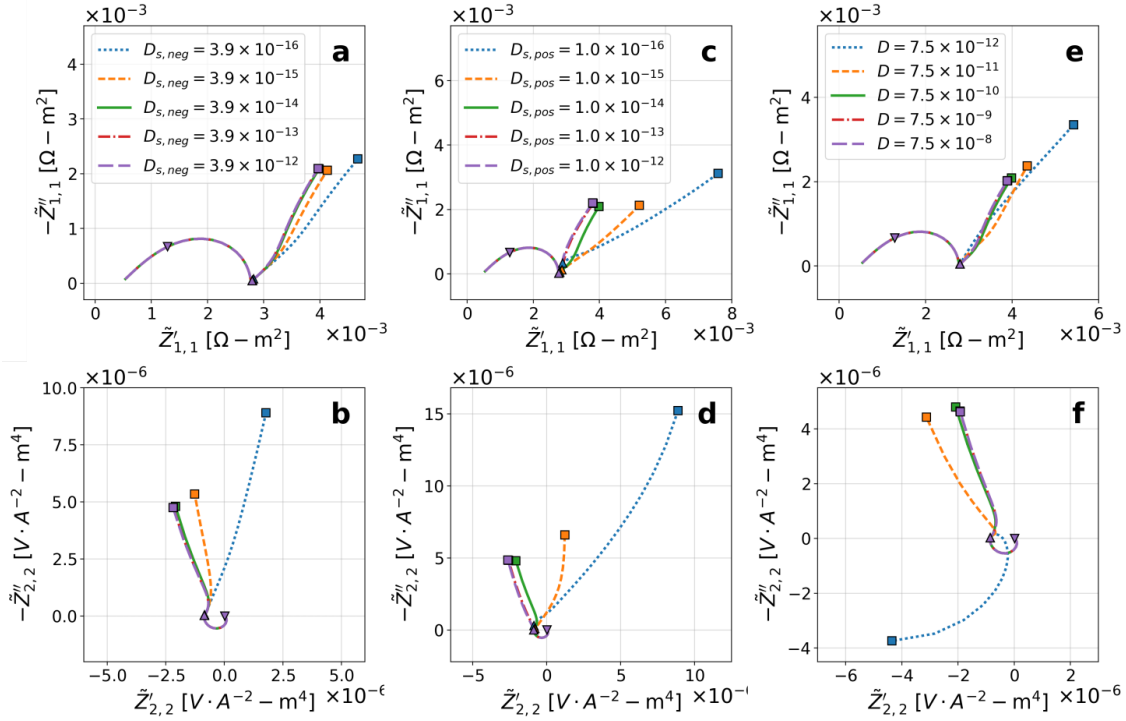

Figure 2.4: Nyquist representations of the first (a, c, e) and second (b, d, f) harmonic impedance spectra for different values of solution- and solid-phase diffusion coefficients, D and $D_{s,i}$. The second harmonic shows a more exaggerated response to changes in the mass-transport parameters. All other parameters were held constant at the values given in Table 2.1 except $\alpha_{a,neg} = 0.45$ and $\alpha_{a,pos} = 0.55$. The ■, ▲, and ▼ symbols indicate 1 mHz, 1 Hz, and 1 kHz, respectively.

In equivalent circuit approaches to impedance analysis, the low frequency tail of the linear EIS response is often used to extract information about the diffusional processes. In their original description of the P2D impedance model on which this work builds, Doyle et al.[59] noted that lithium-ion batteries have many different diffusional impedances, and for simple analysis, the low frequency spectrum must be dominated by a transport process in order for Warburg plots to be accurate. The overlapping diffusional time constants remain a challenge for extracting individual coefficients from impedance spectra. Here we explore if the nonlinear second harmonic spectra may offer more sensitivity.

Figure 2.4 shows the effects of varying the solution- and solid-phase diffusion coefficients over several orders of magnitude. The characteristic "wagging" of the low frequency linear impedance tail shown in Figures 2.4a,c,e makes clear the difficulty in extracting a single diffusion coefficient from a Warburg analysis, since all three diffusional impedance responses manifest similarly. Figures 2.4b,d,f shows the effect of the mass-transport parameters on the second harmonic response. Similarly to the linear impedance response, the high frequency arc remains constant due to the well separated timescales between the kinetic and diffusion regimes. Figure 2.4b and 2.4d show that varying either the negative or positive solid-phase diffusion coefficients has the effect of changing the magnitude and phase of the low frequency response like the linear impedance. For particularly low values of the solution-phase diffusivity, however, Figure 2.4f shows that the structure of the low frequency second harmonic rearranges as this diffusional impedance dominates the response. In nearly all cases, the low frequency changes in second harmonic impedance are more dramatic than in the linear response, suggesting a full physics analysis of experimental linear and second harmonic data may result in a much greater ability to fit low frequency processes. We are exploring this currently.

2.3.5 Effect of thermodynamic parameters

The thermodynamics of the cell determine the impedance response as the frequency goes to zero. The important thermodynamic parameters in the low frequency range are the

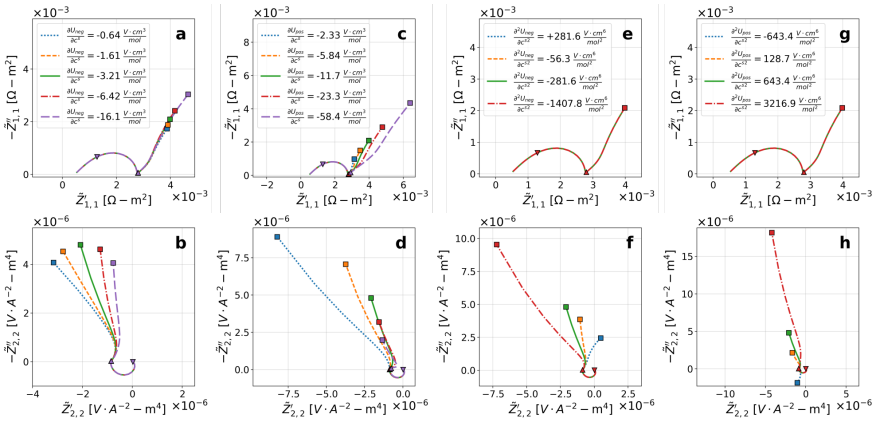

Figure 2.5: Nyquist representations of the first (a, c, e, g) and second (b, d, f, h) harmonic impedance spectra for different values of the first and second open-circuit derivatives, $\frac{\partial U}{\partial c^s}$ and $\frac{\partial^2 U}{\partial c^{s\,2}}$. As the first derivative is varied (a) - (d), a similar effect is seen in the linear and second harmonic response, with a slight exaggeration in the second harmonic response. The linear impedance is insensitive to the changing second derivative. All other parameters were held constant at the values given in Table 2.1 except $\alpha_{a,neg} = 0.45$ and $\alpha_{a,pos} = 0.55$. The ■, ▲, and ▼ symbols indicate 1 mHz, 1 Hz, and 1 kHz, respectively.

derivatives of the open circuit potential, $U(c^s)$, with respect to the concentration of lithium in the electrodes. Mathematically, the linear response shows a sensitivity to only the first derivative, $\frac{\partial U}{\partial c^s}$, while the second and higher harmonics depend on the second, $\frac{\partial^2 U}{\partial c^{s\,2}}$, and higher order derivatives, respectively. Each of these derivatives are evaluated at the lithium concentration in the solid present at the particular state of charge being evaluated, c_0^s.

The sensitivity to second and higher order derivatives could be useful for applications such as estimation of state of charge or probing fundamental thermodynamic models predictions for lithium intercalation. The sign of the second derivative (the curvature of $U(c^s)$) changes in between different phase-change plateaus in the open circuit potential. Figure 2.5 shows the dependence of these open circuit potential derivatives around the base case parameters on the linear and second harmonic spectra. As with the mass transfer case, one sees similar effects between the linear and second harmonic impedance spectra, though with exaggerated effects in the second harmonic, when the first derivative of the open circuit potential is varied (Figure 2.5a-d). In contrast, the first harmonic is completely insensitive to

the second derivative of open circuit potential, whereas the second harmonic is sensitive at low frequencies.

2.4 Conclusions and future implications

Physics-based impedance models are an important component of understanding and interpreting impedance spectra due to their flexibility and physically meaningful parameters. Here, we presented an extension of Newman's P2D impedance model for a lithium-ion battery cell sandwich and demonstrated the simulated linear and harmonic response for a $LiCoO_2|LiC_6$ cell. The strong dependence of the second harmonic on the symmetry of the reaction kinetics for each electrode was demonstrated and the individual effects of many kinetic, mass transport, and thermodynamic parameters were shown.

Introducing higher harmonic spectra into the analysis of an electrochemical system provides additional informational content over the linear response alone. Expanding the model to introduce additional nonlinear contributions to the physics (concentration dependence of parameters like the diffusion coefficients, exchange-current densities, and double-layer capacitances, for example) could lead to the generation of additional insight into the P2D model and its parameters. Quantifying the sensitivity of the model to the many different physicochemical and geometric parameters could provide insight into the experimentally measurable information in the linear and harmonic spectra. Preliminary experimental data indicate that these higher harmonic signatures are easily measurable for commercial lithium-ion cells using standard potentiostats and frequency response analyzers. These results will be explored in the near future.

2.5 Appendix

Table A2.1: Governing equations for the linear impedance response of the P2D model

Solid-phase material balance

Real: $$\epsilon\omega_1 {c^s_{1,1}}'' = \frac{1}{r^2}\frac{\partial}{\partial r}\left(D_s r^2 \frac{\partial {c^s_{1,1}}'}{\partial r}\right) \tag{A1.1r}$$

Imaginary: $$-\epsilon\omega_1 {c^s_{1,1}}' = \frac{1}{r^2}\frac{\partial}{\partial r}\left(D_s r^2 \frac{\partial {c^s_{1,1}}''}{\partial r}\right) \tag{A1.1i}$$

BC at $r = R_p$: $\quad -D_s \frac{\partial {c^s_{1,1}}'}{\partial r} = {j_f}'_{1,1} \qquad -D_s \frac{\partial {c^s_{1,1}}''}{\partial r} = {j_f}''_{1,1}$

BC at $r = 0$: $\quad \frac{\partial {c^s_{1,1}}'}{\partial r} = 0 \qquad \frac{\partial {c^s_{1,1}}''}{\partial r} = 0$

Solution-phase Material Balance

Real: $$\frac{\partial}{\partial x}\left(D_{eff}\frac{\partial {c_{1,1}}'}{\partial x}\right) = \epsilon\omega_1 {c_{1,1}}'' - a\left(1-t^0_+\right)\left({j_f}'_{1,1} + {j_{dl}}'_{1,1}\right) \tag{A1.2r}$$

Imaginary: $$\frac{\partial}{\partial x}\left(D_{eff}\frac{\partial {c_{1,1}}''}{\partial x}\right) = -\epsilon\omega_1 {c_{1,1}}' - a\left(1-t^0_+\right)\left({j_f}''_{1,1} + {j_{dl}}''_{1,1}\right) \tag{A1.2i}$$

BC at $x = 0$ and $x = L$: $\quad \frac{\partial {c_{1,1}}'}{\partial x} = 0 \qquad \frac{\partial {c_{1,1}}''}{\partial x} = 0$

Faraday's Law

Real: $$\frac{\partial {\mathbf{i}_2}'_{1,1}}{\partial x} = aF\left({j_f}'_{1,1} + {j_{dl}}'_{1,1}\right) \tag{A1.3r}$$

Imaginary: $$\frac{\partial {\mathbf{i}_2}''_{1,1}}{\partial x} = aF\left({j_f}''_{1,1} + {j_{dl}}''_{1,1}\right) \tag{A1.3i}$$

BC at $x = 0$ and $x = L$: $\quad {\mathbf{i}_2}'_{1,1} = 0 \qquad {\mathbf{i}_2}''_{1,1} = 0$

BC at $x = l_{neg}$ and $x = l_{neg} + l_{sep}$: $\quad {\mathbf{i}_2}'_{1,1} = -1 \qquad {\mathbf{i}_2}''_{1,1} = 0$

Solid-phase Potential

Real: $$-\sigma_{eff}\frac{\partial {\varphi^s_{1,1}}'}{\partial x} = -1-{\mathbf{i}_2}'_{1,1} \tag{A1.4r}$$

Imaginary: $$-\sigma_{eff}\frac{\partial {\varphi^s_{1,1}}''}{\partial x} = -{\mathbf{i}_2}''_{1,1} \tag{A1.4i}$$

BC at $x = 0$ and $x = L$: $\sigma_{eff}\frac{\partial {\varphi^s_{1,1}}'}{\partial x} = 1$ $\frac{\partial {\varphi^s_{1,1}}''}{\partial x} = 0$
BC at $x = l_{neg}$ and $x = l_{neg} + l_{sep}$: $\frac{\partial {\varphi^s_{1,1}}'}{\partial x} = 0$ $\frac{\partial {\varphi^s_{1,1}}''}{\partial x} = 0$

Solution-phase Potential

Real: $$-\kappa_{eff}\frac{\partial \varphi'_{1,1}}{\partial x} = {\mathbf{i}_2}'_{1,1} - \frac{2\kappa_{eff}RT}{c_0F}(1-t^0_+)\frac{\partial c'_{1,1}}{\partial x} \tag{A1.5r}$$

Imaginary: $$-\kappa_{eff}\frac{\partial \varphi''_{1,1}}{\partial x} = {\mathbf{i}_2}''_{1,1} - \frac{2\kappa_{eff}RT}{c_0F}(1-t^0_+)\frac{\partial c''_{1,1}}{\partial x} \tag{A1.5i}$$

BC at $x = 0$: $\varphi'_{1,1} = 0$ $\varphi''_{1,1} = 0$
BC at $x = l_{neg} + l_{neg} + l_{sep}$: $\frac{\partial {\varphi_{1,1}}'}{\partial x} = 0$ $\frac{\partial {\varphi_{1,1}}''}{\partial x} = 0$

Faradaic Flux

Real: $${j_f}'_{1,1} = \frac{i_0(\alpha_a + \alpha_c)}{RT}\eta'_{1,1} \tag{A1.6r}$$

Imaginary: $${j_f}''_{1,1} = \frac{i_0(\alpha_a + \alpha_c)}{RT}\eta''_{1,1} \tag{A1.6i}$$

Double-layer Flux

Real: $${j_{dl}}'_{1,1} = \omega_1\frac{C_{dl}}{F}\left({\varphi^s_{1,1}}'' - {\varphi_{1,1}}''\right) \tag{A1.7r}$$

Imaginary: $${j_{dl}}''_{1,1} = \omega_1\frac{C_{dl}}{F}\left({\varphi_{1,1}}' - {\varphi^s_{1,1}}'\right) \tag{A1.7i}$$

Overpotential

Real: $$\eta'_{1,1} = {\varphi^s_{1,1}}' - \varphi'_{1,1} - \frac{dU}{dc^s}{c^s_{1,1}}' \tag{A1.8r}$$

Imaginary: $$\eta''_{1,1} = {\varphi^s_{1,1}}'' - \varphi''_{1,1} - \frac{dU}{dc^s}{c^s_{1,1}}'' \tag{A1.8i}$$

Table A2.2: Governing equations for the 2^{nd} harmonic response of the P2D model

Solid-phase material balance

Real: $$2\epsilon\omega_1 {c_{2,2}^s}'' = \frac{1}{r^2}\frac{\partial}{\partial r}\left(D_s r^2 \frac{\partial {c_{2,2}^s}'}{\partial r}\right) \tag{A2.1r}$$

Imaginary: $$-2\epsilon\omega_1 {c_{2,2}^s}' = \frac{1}{r^2}\frac{\partial}{\partial r}\left(D_s r^2 \frac{\partial {c_{2,2}^s}''}{\partial r}\right) \tag{A2.1i}$$

BC at $r = R_p$: $-D_s \frac{\partial {c_{2,2}^s}'}{\partial r} = {j_f}'_{2,2}$ $\quad -D_s \frac{\partial {c_{2,2}^s}''}{\partial r} = {j_f}''_{2,2}$
BC at $r = 0$: $\frac{\partial {c_{2,2}^s}'}{\partial r} = 0$ $\quad \frac{\partial {c_{2,2}^s}''}{\partial r} = 0$

Solution-phase Material Balance

Real: $$\frac{\partial}{\partial x}\left(D_{eff}\frac{\partial {c_{2,2}}'}{\partial x}\right) = 2\epsilon\omega_1 {c_{2,2}}'' - a\left(1-t_+^0\right)\left({j_f}'_{2,2} + {j_{dl}}'_{2,2}\right) \tag{A2.2r}$$

Imaginary: $$\frac{\partial}{\partial x}\left(D_{eff}\frac{\partial {c_{2,2}}''}{\partial x}\right) = -2\epsilon\omega_1 {c_{2,2}}' - a\left(1-t_+^0\right)\left({j_f}''_{2,2} + {j_{dl}}''_{2,2}\right) \tag{A2.2i}$$

BC at $x = 0$ and $x = L$: $\frac{\partial {c_{2,2}}'}{\partial x} = 0$ $\quad \frac{\partial {c_{2,2}}''}{\partial x} = 0$

Faraday's Law

Real: $$\frac{\partial {\mathbf{i}_2}'_{2,2}}{\partial x} = aF\left({j_f}'_{2,2} + {j_{dl}}'_{2,2}\right) \tag{A2.3r}$$

Imaginary: $$\frac{\partial {\mathbf{i}_2}''_{2,2}}{\partial x} = aF\left({j_f}''_{2,2} + {j_{dl}}''_{2,2}\right) \tag{A2.3i}$$

BC at $x = 0$ and $x = L$: ${\mathbf{i}_2}'_{2,2} = 0$ $\quad {\mathbf{i}_2}''_{2,2} = 0$
BC at $x = l_{neg}$ and $x = l_{neg} + l_{sep}$: ${\mathbf{i}_2}'_{2,2} = 0$ $\quad {\mathbf{i}_2}''_{2,2} = 0$

Solid-phase Potential

Real: $$-\sigma_{eff}\frac{\partial {\varphi_{2,2}^s}'}{\partial x} = -{\mathbf{i}_2}'_{2,2} \tag{A2.4r}$$

Imaginary: $$-\sigma_{eff}\frac{\partial {\varphi_{2,2}^s}''}{\partial x} = -{\mathbf{i}_2}''_{2,2} \tag{A2.4i}$$

BC at $x = 0$ and $x = L$: $\sigma_{eff}\frac{\partial {\varphi_{2,2}^s}'}{\partial x} = 0$ $\quad \frac{\partial {\varphi_{2,2}^s}''}{\partial x} = 0$
BC at $x = l_{neg}$ and $x = l_{neg} + l_{sep}$: $\frac{\partial {\varphi_{2,2}^s}'}{\partial x} = 0$ $\quad \frac{\partial {\varphi_{2,2}^s}''}{\partial x} = 0$

Solution-phase Potential

Real:
$$-\kappa_{eff}\frac{\partial\varphi'_{2,2}}{\partial x} = \mathbf{i}'_{2,2} - \frac{\kappa_{eff}RT}{{c_0}^2F}(1-t^0_+)\left(2c_0\frac{\partial c'_{2,2}}{\partial x} - c'_{1,1}\frac{\partial c'_{1,1}}{\partial x} + c''_{1,1}\frac{\partial c''_{1,1}}{\partial x}\right) \tag{A2.5r}$$

Imaginary:
$$-\kappa_{eff}\frac{\partial\varphi''_{2,2}}{\partial x} = \mathbf{i}''_{2,2} - \frac{\kappa_{eff}RT}{{c_0}^2F}(1-t^0_+)\left(2c_0\frac{\partial c''_{2,2}}{\partial x} - c'_{1,1}\frac{\partial c''_{1,1}}{\partial x} - c''_{1,1}\frac{\partial c'_{1,1}}{\partial x}\right) \tag{A2.5i}$$

BC at $x = 0$: $\quad \varphi'_{2,2} = 0 \qquad \varphi''_{2,2} = 0$

BC at $x = l_{neg} + l_{neg} + l_{sep}$: $\quad \frac{\partial {\varphi_{2,2}}'}{\partial x} = 0 \qquad \frac{\partial {\varphi_{2,2}}''}{\partial x} = 0$

Faradaic Flux

Real:
$$j_f{}'_{2,2} = \frac{i_0(\alpha_a+\alpha_c)}{RT}\eta'_{2,2} + \frac{i_0\left({\alpha_a}^2-{\alpha_c}^2\right)F}{4R^2T^2}\left({\eta'_{1,1}}^2 - {\eta''_{1,1}}^2\right) \tag{A2.6r}$$

Imaginary:
$$j_f{}''_{2,2} = \frac{i_0(\alpha_a+\alpha_c)}{RT}\eta''_{2,2} + \frac{i_0\left({\alpha_a}^2-{\alpha_c}^2\right)F}{2R^2T^2}\left(\eta'_{1,1}\eta''_{1,1}\right) \tag{A2.6i}$$

Double-layer Flux

Real:
$$j_{dl}{}'_{2,2} = 2\omega_1\frac{C_{dl}}{F}\left({\varphi^s_{2,2}}'' - {\varphi_{2,2}}''\right) \tag{A2.7r}$$

Imaginary:
$$j_{dl}{}''_{2,2} = 2\omega_1\frac{C_{dl}}{F}\left({\varphi_{2,2}}' - {\varphi^s_{2,2}}'\right) \tag{A2.7i}$$

Overpotential

Real:
$$\eta'_{2,2} = {\varphi^s_{2,2}}' - \varphi'_{2,2} - \frac{dU}{dc^s}{c^s_{2,2}}' - \frac{1}{4}\frac{d^2U}{{dc^s}^2}\left({c^s{}'_{1,1}}^2 - {c^s{}''_{1,1}}^2\right) \tag{A2.8r}$$

Imaginary:
$$\eta''_{2,2} = {\varphi^s_{2,2}}'' - \varphi''_{2,2} - \frac{dU}{dc^s}{c^s_{2,2}}'' - \frac{1}{2}\frac{d^2U}{{dc^s}^2}\left(c^s{}'_{1,1}c^s{}''_{1,1}\right) \tag{A2.8i}$$

Table A2.3: Governing equations for the 3^{rd} harmonic response of the P2D model

Solid-phase material balance

Real: $$3\epsilon\omega_1 {c_{3,3}^s}'' = \frac{1}{r^2}\frac{\partial}{\partial r}\left(D_s r^2 \frac{\partial {c_{3,3}^s}'}{\partial r}\right) \tag{A3.1r}$$

Imaginary: $$-3\epsilon\omega_1 {c_{3,3}^s}' = \frac{1}{r^2}\frac{\partial}{\partial r}\left(D_s r^2 \frac{\partial {c_{3,3}^s}''}{\partial r}\right) \tag{A3.1i}$$

BC at $r = R_p$: $\quad -D_s \frac{\partial {c_{3,3}^s}'}{\partial r} = {j_f}'_{3,3} \qquad -D_s \frac{\partial {c_{3,3}^s}''}{\partial r} = {j_f}''_{3,3}$

BC at $r = 0$: $\quad \frac{\partial {c_{3,3}^s}'}{\partial r} = 0 \qquad \frac{\partial {c_{3,3}^s}''}{\partial r} = 0$

Solution-phase Material Balance

Real: $$\frac{\partial}{\partial x}\left(D_{eff}\frac{\partial {c_{3,3}}'}{\partial x}\right) = 3\epsilon\omega_1 {c_{3,3}}'' - a\left(1-t_+^0\right)\left({j_f}'_{3,3} + {j_{dl}}'_{3,3}\right) \tag{A3.2r}$$

Imaginary: $$\frac{\partial}{\partial x}\left(D_{eff}\frac{\partial {c_{3,3}}''}{\partial x}\right) = -3\epsilon\omega_1 {c_{3,3}}' - a\left(1-t_+^0\right)\left({j_f}''_{3,3} + {j_{dl}}''_{3,3}\right) \tag{A3.2i}$$

BC at $x = 0$ and $x = L$: $\quad \frac{\partial {c_{3,3}}'}{\partial x} = 0 \qquad \frac{\partial {c_{3,3}}''}{\partial x} = 0$

Faraday's Law

Real: $$\frac{\partial {\mathbf{i}_2}'_{3,3}}{\partial x} = aF\left({j_f}'_{3,3} + {j_{dl}}'_{3,3}\right) \tag{A3.3r}$$

Imaginary: $$\frac{\partial {\mathbf{i}_2}''_{3,3}}{\partial x} = aF\left({j_f}''_{3,3} + {j_{dl}}''_{3,3}\right) \tag{A3.3i}$$

BC at $x = 0$ and $x = L$: $\quad {\mathbf{i}_2}'_{3,3} = 0 \qquad {\mathbf{i}_2}''_{3,3} = 0$

BC at $x = l_{neg}$ and $x = l_{neg} + l_{sep}$: $\quad {\mathbf{i}_2}'_{3,3} = 0 \qquad {\mathbf{i}_2}''_{3,3} = 0$

Solid-phase Potential

Real: $$-\sigma_{eff}\frac{\partial {\varphi_{3,3}^s}'}{\partial x} = -{\mathbf{i}_2}'_{3,3} \tag{A3.4r}$$

Imaginary: $$-\sigma_{eff}\frac{\partial {\varphi_{3,3}^s}''}{\partial x} = -{\mathbf{i}_2}''_{3,3} \tag{A3.4i}$$

BC at $x = 0$ and $x = L$: $\quad \sigma_{eff}\frac{\partial {\varphi_{3,3}^s}'}{\partial x} = 0 \qquad \frac{\partial {\varphi_{3,3}^s}''}{\partial x} = 0$

BC at $x = l_{neg}$ and $x = l_{neg} + l_{sep}$: $\quad \frac{\partial {\varphi_{3,3}^s}'}{\partial x} = 0 \qquad \frac{\partial {\varphi_{3,3}^s}''}{\partial x} = 0$

Solution-phase Potential

Real:
$$-\kappa_{eff}\frac{\partial \varphi'_{3,3}}{\partial x} = \mathbf{i}_2{}'_{3,3} - \frac{\kappa_{eff}RT}{2{c_0}^3F}(1-t_+^0)\Big[4{c_0}^2\frac{\partial c'_{3,3}}{\partial x} + 2c_0\Big(c''_{1,1}\frac{\partial c''_{2,2}}{\partial x} - c'_{1,1}\frac{\partial c'_{2,2}}{\partial x} + c''_{2,2}\frac{\partial c''_{1,1}}{\partial x} - c'_{2,2}\frac{\partial c'_{1,1}}{\partial x}\Big) + \frac{\partial c'_{1,1}}{\partial x}\left({c'_{1,1}}^2 - {c''_{1,1}}^2\right) - 2c'_{1,1}c''_{1,1}\frac{\partial c''_{1,1}}{\partial x}\Big] \tag{A3.5r}$$

Imaginary:
$$-\kappa_{eff}\frac{\partial \varphi''_{3,3}}{\partial x} = \mathbf{i}_2{}''_{3,3} - \frac{\kappa_{eff}RT}{2{c_0}^3F}(1-t_+^0)\Big[4{c_0}^2\frac{\partial c''_{3,3}}{\partial x} - 2c_0\Big(c'_{1,1}\frac{\partial c''_{2,2}}{\partial x} + c''_{1,1}\frac{\partial c'_{2,2}}{\partial x} + c''_{2,2}\frac{\partial c'_{1,1}}{\partial x} + c'_{2,2}\frac{\partial c''_{1,1}}{\partial x}\Big) + \frac{\partial c''_{1,1}}{\partial x}\left({c'_{1,1}}^2 - {c''_{1,1}}^2\right) + 2c'_{1,1}c''_{1,1}\frac{\partial c'_{1,1}}{\partial x}\Big] \tag{A3.5i}$$

BC at $x = 0$: $\quad \varphi'_{3,3} = 0 \qquad \varphi''_{3,3} = 0$

BC at $x = l_{neg} + l_{neg} + l_{sep}$: $\quad \frac{\partial {\varphi_{3,3}}'}{\partial x} = 0 \qquad \frac{\partial {\varphi_{3,3}}''}{\partial x} = 0$

Faradaic Flux

Real:
$$j_f{}'_{3,3} = \frac{i_0(\alpha_a+\alpha_c)}{RT}\eta'_{3,3} + \frac{i_0\left({\alpha_a}^2-{\alpha_c}^2\right)F}{2R^2T^2}\left(\eta'_{1,1}\eta'_{2,2} - \eta''_{1,1}\eta''_{2,2}\right) + \frac{i_0\left({\alpha_a}^3+{\alpha_c}^3\right)F^2}{24R^3T^3}\left({\eta'_{1,1}}^3 - 3\eta'_{1,1}{\eta''_{1,1}}^2\right) \tag{A3.6r}$$

Imaginary:
$$j_f{}''_{3,3} = \frac{i_0(\alpha_a+\alpha_c)}{RT}\eta''_{3,3} + \frac{i_0\left({\alpha_a}^2-{\alpha_c}^2\right)F}{2R^2T^2}\left(\eta'_{1,1}\eta''_{2,2} + \eta''_{1,1}\eta'_{2,2}\right) + \frac{i_0\left({\alpha_a}^3+{\alpha_c}^3\right)F^2}{24R^3T^3}\left(3\eta''_{1,1}{\eta'_{1,1}}^2 - {\eta''_{1,1}}^3\right) \tag{A3.6i}$$

Double-layer Flux

Real:
$$j_{dl}{}'_{3,3} = 3\omega_1\frac{C_{dl}}{F}\left({\varphi^s}''_{3,3} - \varphi''_{3,3}\right) \tag{A3.7r}$$

Imaginary:
$$j_{dl}{}''_{3,3} = 3\omega_1\frac{C_{dl}}{F}\left({\varphi^s}'_{3,3} - \varphi'_{3,3}\right) \tag{A3.7i}$$

Overpotential

Real:
$$\eta'_{3,3} = {\varphi^s}'_{3,3} - \varphi'_{3,3} - \frac{\partial U}{dc^s}{c^s}'_{3,3} - \frac{1}{2}\frac{d^2U}{dc^{s2}}\left({c^s}'_{1,1}{c^s}'_{2,2} - {c^s}''_{1,1}{c^s}''_{2,2}\right) - \frac{1}{24}\frac{d^3U}{dc^{s3}}\left({{c^s}'_{1,1}}^3 - 3{c^s}'_{1,1}{{c^s}''_{1,1}}^2\right) \tag{A3.8r}$$

Imaginary:
$$\eta''_{3,3} = {\varphi^s_{3,3}}'' - \varphi''_{3,3} - \frac{dU}{dc^s}{c^s_{3,3}}'' - \frac{1}{2}\frac{d^2U}{dc^{s2}}\left({c^s}'_{1,1}{c^s}''_{2,2} + {c^s}''_{1,1}{c^s}'_{2,2}\right) - \frac{1}{24}\frac{\partial^3U}{dc^{s3}}\left(3{c^s}''_{1,1}{{c^s}'_{1,1}}^2 - {{c^s}''_{1,1}}^3\right) \tag{A3.8i}$$

Chapter 3

NONLINEAR EIS FOR LITHIUM-ION BATTERIES: EXPERIMENTAL APPROACH, ANALYSIS, AND INITIAL FINDINGS

Note: this chapter has been submitted as a preprint and an article

- Matthew D. Murbach[‡*], Victor W. Hu[‡*], and Daniel T. Schwartz. Nonlinear electrochemical impedance spectroscopy of lithium-ion batteries: Experimental approach, analysis, and initial findings. *Open Science Framework*, 2018. DOI: https://osf.io/tdnwa/

A preprint as well as all data and code can be found on the OSF project page.[98]

Abstract

Nonlinear electrochemical impedance spectroscopy (NLEIS) is a moderate-amplitude extension to linear EIS that provides a sensitive and complementary whole-battery diagnostic for charge transfer kinetics, mass transport, and thermodynamics. We present the first full-frequency, second harmonic NLEIS spectra for lithium-ion batteries using commercially available, 1.5 Ah LiNMC|C cells. The mathematical framework for NLEIS shows, and experiments confirm, that moderate-amplitude input modulations can generate a second harmonic output that does not intrinsically corrupt the linear EIS response. Experimental measurements at varied states-of-charge (SoC) and states-of-health (SoH) are used to illustrate and compare NLEIS and EIS data. At low frequencies, the second harmonic NLEIS spectrum is shown to produce a more distinct response to SoC dependent thermodynamic and diffusion processes than linear EIS. By combining NLEIS and EIS, we are able to characterize degradation in early cell cycling (where cells lost <1% of initial capacity). Second harmonic NLEIS is shown to be sensitive to degradation in charge transfer symmetry whereas linear EIS is mainly sensitive to changes in charge transfer rates. For example, NLEIS shows that fresh cells have high symmetry charge transfer ($\alpha_a = \alpha_c = 0.5$) on both electrodes, whereas early

in the cycling there is a shift toward kinetics that favor oxidation on the positive electrode ($\alpha_{a,pos} > 0.5, \alpha_{c,pos} < 0.5$). Combined analysis of EIS and NLEIS spectra shows promise for improved parameter estimation and model validation. All experimental data and analysis code for this manuscript can be found on ECSar$X$iv.

3.1 Introduction

The unrelenting drive for higher energy and power dense lithium-ion batteries means the quantity of active materials is increasing at the same time separator thickness and electrolyte volume is decreasing.[99] Under these conditions, chemical and electrochemical interactions across the whole cell are critical for understanding and optimizing battery performance. Thus, there is a growing need for sensitive and selective *in situ* diagnostics that support fundamental studies of whole cells. Electrochemical impedance spectroscopy (EIS) is a powerful, noninvasive technique that works by applying a small current or voltage modulation and measuring the linear voltage or current response.[3] EIS has been used to characterize lithium-ion battery properties such as the solid-electrolyte interphase (SEI) layers,[80,100] mass transfer and kinetics of the electrode materials,[10,81] and degradative and capacity loss mechanisms.[82,101] EIS experiments are traditionally analyzed using equivalent circuit analogs, but linearized physics-based models are also available.[59,73,102] While EIS is a widely used and valuable technique, batteries are inherently *nonlinear* systems, and the linear nature of EIS can lead to degeneracy; that is, a single EIS dataset can often be represented equally well by different linear models[19] and circuit analogs.[20]

A natural extension to EIS uses moderately larger amplitude perturbations of current or voltage to drive the battery into a weakly nonlinear regime. This variant of EIS, which we call nonlinear EIS (NLEIS), breaks the degeneracy of linearization and contains complementary information to EIS.[19] In the weakly nonlinear regime, a moderate-amplitude, single-sine input of current or voltage produces one or more measurable (but small) higher harmonics of the fundamental frequency in the output Fourier spectrum. These higher harmonics have often been treated as evidence of a "corrupted" linear response to be eliminated from EIS measurements;[21,23–26] however, NLEIS spectra can be used to elucidate information about the nonlinear dynamics of a system that cannot be probed with EIS alone. NLEIS has previously been used in studies of corrosion,[31,87,88] fuel cell mechanisms,[19,50,103] mass transport-controlled systems,[46–48] chemical sensing,[41,42,45] as well as lithium-ion batteries.[52,75] Lvovich

and Smiechowski were able to characterize degradation in industrial lubricants through monotonic trends in the second harmonic NLEIS responses, despite no noticeable trend in the linear responses.[44] Wilson et al. used physical models to distinguish the rate determining mechanism of the oxygen-reduction reaction on solid oxide fuel cell electrodes, despite the models being degenerate in their linear response.[19] Xu and Riley demonstrated that the transfer coefficients, which have typically been experimentally difficult to determine, can be found through the use of even harmonics in the well-characterized ferri-ferrocyanide redox couple.[96] Heubner et al., further used the same principles to determine the transfer coefficients in lithium iron-phosphate electrodes.[97] Recently, higher harmonic responses in lithium-ion batteries have been studied through a total-harmonic distortion analysis to examine nonlinear Faradaic processes and battery degradation.[52–55]

In these past studies, it is important to make distinctions between nonlinear measurements in the weakly nonlinear regime, where the measurable harmonics are few in number and the voltage modulation is less than the thermal voltage, $\frac{RT}{nF}$ (approximately 25 mV for a single electron transfer at room temperature),[19,31,46–48,50,75,87,88] versus those studies that use much larger modulations of current or voltage and produce many harmonics.[52–55] The NLEIS analysis presented here is only appropriate for the weakly nonlinear response.

NLEIS measurements are an interesting complement to EIS, in part, because the measurements do not necessarily require new equipment from traditional EIS.[23,96] Here we show how small changes in the experimental procedures and signal processing for EIS can allow researchers to calculate higher harmonic NLEIS spectra. These results are used in conjunction with an extension of the pseudo-two-dimensional (P2D) impedance battery model that includes the nonlinear harmonic response[75] to gain insight into the physicochemical behavior of commercial Samsung 18650 lithium-ion cells.

3.2 Methods

3.2.1 Cycling procedure of the lithium-ion battery

Cycling measurements on commercially available Samsung 1.5 Ah LiNMC|C cells (INR 18650-15M) were made using a Maccor 4000M battery cycler in a controlled temperature environment of 25^{o}C using a Maccor MTC-020 chamber. In these experiments, all cells were first subjected to five formation cycles using a C/2 charge and discharge rate within the specified voltage window (2.5 V to 4.2 V). To study the effects of aging, NLEIS measurements were conducted on new cells and cells that had been cycled for 100 cycles. The full cycles consisted of a 2C (3 A) constant current charge from 2.5 V (0% SoC) to 4.2 V (100% SoC), a constant voltage at 4.2 V until a 100 mA current cutoff was reached, and a constant current discharge at 2C.

3.2.2 Measuring the nonlinear impedance of a lithium-ion battery

We demonstrate the full-spectrum application of nonlinear electrochemical impedance spectroscopy for batteries using an Autolab PGSTAT128N potentiostat/galvanostat with the frequency response analyzer module (Autolab FRA32). The measurements were made at a controlled temperature of 25^{o}C and used a four-electrode configuration with voltage sensing at the cell terminals.

A single cosine current modulation waveform with frequency ω_1 and amplitude ΔI was sent to the galvanostat

$$\hat{I}(t;\Delta I,\omega_1) = \Delta I \mathrm{Re}\left\{\exp\left(j\omega_1 t\right)\right\}, \tag{3.1}$$

where $j = \sqrt{-1}$ and Re denotes the real component of the bracketed function. The notation $I(t;\Delta I,\omega_1)$ can be generalized as $X(a;b,c,\dots)$ to show X is the dependent variable, a is an independent variable, and $b, c, \dots$ are experimental parameters of the solution. The actual time domain current perturbation applied to the battery by the galvanostat, $I(t;\Delta I,\omega_1)$, and the measured voltage response, $V(t;\Delta I,\omega_1)$, were recorded using input modulations of

0.3, 0.4, and 0.5 A over a logarithmically spaced frequency range from 10 kHz to 3.16 mHz. Time domain data were recorded after the system had reached a steady-periodic state. A minimum of 10 steady-periodic cycles were logged with $N = 4096$ synchronous time domain measurements for both current and voltage. A rest time of 30 minutes was provided between each frequency sweep to provide a consistent baseline.

Measurements at specific states-of-charge were carried out by adding a specified amount of charge to a fully discharged battery (discharged to 2.5 V and held until the current reached 1 mA). The amount of charge to add was determined by capacity measurements at C/10 cycling. The voltages of specific states-of-charge were recorded after a four-hour rest to allow the cell to equilibrate.[104] For subsequent NLEIS experiments, each cell was charged to the desired voltage designated by the baseline (summarized in Table A1) through a C/10 rate, and then subjected to a two-hour constant voltage charge at the desired voltage. The cells were then allowed to equilibrate for an additional two hours at open circuit.

Fast Fourier transformation (FFT) of a steady-periodic input current of the form given by Equation 3.1, theoretically results in a very simple spectrum,

$$\mathrm{FFT}\left\{I(t;\Delta I,\omega_1)\right\} = \Delta I, \tag{3.2}$$

at the frequency ω_1, and zero at all other frequencies. The resulting voltage spectrum, however, often contained complex Fourier coefficients at integer multiples, k, of the fundamental frequency, ω_1,

$$\mathrm{FFT}\left\{V(t;\Delta I,\omega_1)\right\} = \tilde{V}(k\omega_1;\Delta I). \tag{3.3}$$

The experimental reality of our galvanostat was that harmonic distortions were introduced into the ideal input current spectrum given by Equation 3.2 when operated at high frequencies and amplitudes, leading to an actual input current spectrum of the form:

$$\mathrm{FFT}\left\{I(t;\Delta I,\omega_1)\right\} = \tilde{I}'(1\omega_1;\Delta I) + THD \tag{3.4}$$

where THD is the total harmonic distortion of the single sine input signal and $\tilde{I}'(1\omega_1; \Delta I)$ is the real Fourier coefficient at the fundamental frequency of the current perturbation (closely approximating ΔI). To ensure nonlinear experimental results presented here are from nonlinearity in the battery, not the power amplifier, we only report second harmonic data up to a frequency of 10 Hz for this instrument, where THD in the input was always below 1.0%. Linear EIS is reported for the entire frequency range.

The complex Fourier voltage spectrum had a pure harmonic structure comprised of signals at integer k values of the fundamental frequency ω_1. The lack of sub-harmonic ($0 < k < 1$) or anharmonic (non-integer k) signals in the output voltage spectrum indicated that the batteries (and measurement instrument) were stable, in all cases, to the finite amplitude current modulations. However, noise and imperfect sampling did lead to a small, continuous baseline in the spectrum. The baselines for the linear ($k = 1$) and second harmonic ($k = 2$) peaks were subtracted using a quadratic polynomial fit to several anharmonic baseline points adjacent to each harmonic peak of interest.

The amplitude of each voltage harmonic depends on the current modulation amplitude, ΔI. Prior research has shown that the weakly nonlinear response of the battery can be expressed as a power series in modulation amplitude such that,[19,47,48]

$$\tilde{V}(k\omega_1; \Delta I) = \sum_{r=0}^{\infty} \Delta I^{k+2r} \tilde{Z}_{k,k+2r}(\omega_1) \tag{3.5}$$

where the resulting double-indexed coefficients, $\tilde{Z}_{k,p}(\omega_1)$, are pure frequency dispersion coefficients — we will call them linear and nonlinear impedance coefficients — corresponding to harmonic number, k, and order, p. The double-indexed coefficient $\tilde{Z}_{1,1}(\omega_1)$ is identically equal to the normal (linear) electrochemical impedance of the system. $\tilde{Z}_{2,2}(\omega_1)$ is the leading order nonlinear electrochemical impedance derived from the second harmonic of the voltage response to a pure cosine input current. The impedance coefficients for $p > k$, represent higher order corrections to the leading order $k = p$ solutions. In this work, we present an

experimental and computational evaluation of the leading order terms in Equation 3.5,

$$\tilde{V}(1\omega_1; \Delta I) = \Delta I \tilde{Z}_{1,1}(\omega_1) \tag{3.6}$$

$$\tilde{V}(2\omega_1; \Delta I) = \Delta I^2 \tilde{Z}_{2,2}(\omega_1). \tag{3.7}$$

From the complete form of Equation 3.5, it is possible to estimate how error scales when we truncate the series and use Equation 3.6 to determine the traditional linear electrochemical impedance, and Equation 3.7 to find the second harmonic NLEIS spectrum. Specifically, the error associated with using Equation 3.6 scales as $\sim O(\Delta I^3)$ and the error from using Equation 3.7 scales as $\sim O(\Delta I^4)$. Consequently, the perturbation amplitudes used here are bounded by being large enough to generate a measurable second harmonic response and small enough that systematic error from the higher order correction terms, $p > k$, are unimportant compared to experimental noise.

All of the data presented in this paper, additional data showing reproducibility across several identical Samsung cells, data for additional states-of-charge, data used to analyze the harmonic distortion of the galvanostat, as well as all of the software used for signal processing and analysis, can be found in the archived files and Supplementary Jupyter Notebook.[105]

3.3 Results

3.3.1 Current modulation and voltage response signals

Typical time domain measurements of the input current and output voltage response from a Samsung high-power LiNMC|C cell are shown for a frequency of $\omega_1 = 0.5$ Hz in Figure 3.1a and 3.1b, respectively, for three different current modulation amplitudes ($\Delta I = 0.1$ A, 0.3 A, and 0.5 A). Time domain data of this nature, measured at different states-of-charge, frequencies, and amplitudes, are the raw data for our method.

In the time domain, the current (Figure 3.1a) appears to be a pure cosine. The output voltage response (Figure 3.1b) also appears to be a sinusoidal signal, with a phase and

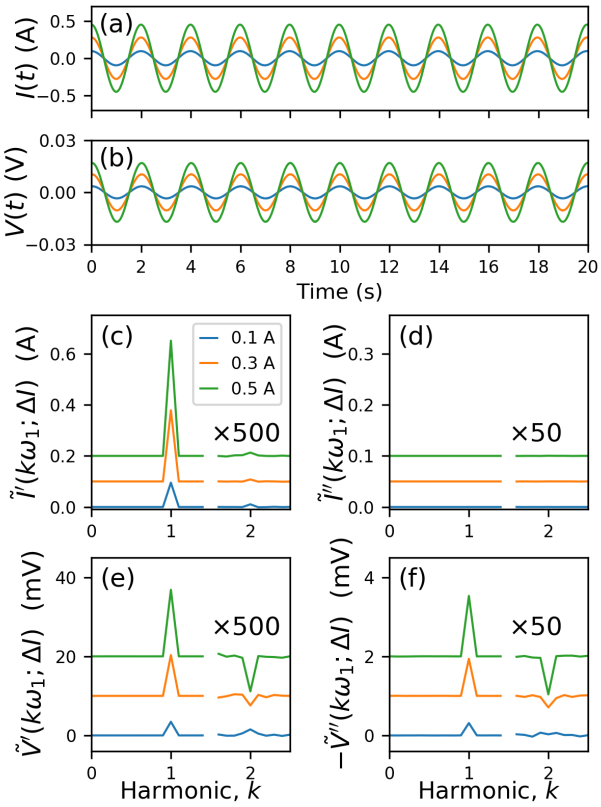

Figure 3.1: Measured time domain current (a) and voltage (b) response for a commercial 1.5 Ah LiNMC|C cell excited by a $\omega_1 = 0.5$ Hz current perturbation of varying amplitudes (ΔI) ranging from 0.1 A to 0.5 A. These signals are transformed into the frequency domain to enable analysis of the real (c, e) and imaginary (d, f) components at different harmonics, k. Offsets are added for clarity and the real and imaginary values for $k > 1.5$ are multiplied by 500× and 50×, respectively, to be on the same scale. Voltage signal has mean open circuit value of 3.643 V substracted.

amplitude that depends on the input frequency and amplitude of the modulated current. For these high-power 1500 mAh cells, a current modulation of 100 mA is seen to produce a voltage modulation of about 4 mV around the open circuit voltage, whereas the largest current modulation of 500 mA produces roughly 20 mV of voltage modulation around the open circuit voltage. In EIS, a 4 mV modulation would be expected to fall in the linear response regime of nearly any electrochemical system. In contrast, a 20 mV modulation would generally be considered large enough to drive a weakly nonlinear response. For all of the NLEIS experiments reported here, we use current modulations between 300 and 500 mA; for the Samsung cells under test, the modulated voltages are in the 10s of millivolts, or weakly nonlinear. We also do select experiments with 33 mA current modulation to determine impedances under traditional, very small amplitude linear conditions.

Details of the phase, amplitude, and harmonic content of the input current and output voltage signals are more evident in frequency domain spectra determined through FFT of the time domain signals, as shown in Figures 3.1c-3.1f. The real and imaginary current spectra (Figure 3.1c and 3.1d, respectively) show that the input is a purely real signal. A tiny amplifier-induced second harmonic signal ($k = 2$) is made evident by multiplying that portion of the spectrum by 500×, demonstrating that the actual galvanostat amplifier has a spectrum represented by Equation 3.4, but it is close to the ideal input given by Equation 3.2. In all that follows, we use the measured value $\tilde{I}'(1\omega_1; \Delta I)$ rather than the ideal value ΔI, when computing experimental impedances via Equations 3.6 and 3.7. As noted, the difference between the measured $\tilde{I}'(1\omega_1; \Delta I)$ and ΔI is generally small.

The real and imaginary frequency domain voltage spectra (Figures 3.1e and 3.1f, respectively) show several features not easily seen in time domain measurements. In the frequency domain, the phase shift and magnitude of each harmonic in the voltage spectra can be quantified based by the magnitudes of the real and imaginary components. Qualitatively, one can see that the first harmonic ($k = 1$) in voltage grows linearly with $\tilde{I}'(1\omega_1; \Delta I)$ values from Figure 3.1c, as predicted by Equation 3.6. Likewise, the second harmonic ($k = 2$) in voltage appears to grow at a super-linear rate with $\tilde{I}'(1\omega_1; \Delta I)$; Equation 3.7 suggests a quadratic

dependence. The signs and ratios of the real and imaginary components for the $k = 2$ peaks are different than the $k = 1$ peaks at the fundamental frequency.

3.3.2 Amplitude dependence of voltage harmonics

To calculate the linear (traditional EIS) and nonlinear second harmonic impedance coefficients for the data in Figure 3.1, at frequency $\omega_1 = 0.5$ Hz, we use the real and imaginary $k = 1$ and $k = 2$ data along with Equations 3.6 and 3.7. Figure 2 shows the amplitude dependence of the voltage harmonics in Figures 3.1e and 3.1f as a function of $\tilde{I}'(1\omega_1; \Delta I)$, the $k = 1$ peak in Figure 3.1c. The impedance coefficients $\tilde{Z}_{1,1}(\omega_1)$ and $\tilde{Z}_{2,2}(\omega_1)$ are the best-fit coefficients from the polynomials in Equations 3.6 and 3.7, where $\tilde{I}'(1\omega_1; \Delta I)$ rather than ΔI is used. To retain the phase information in the double-indexed impedance coefficients, the real (Figure 3.2a) and imaginary (Figure 3.2b) components of the harmonic response are fit separately.

The solid lines in Figure 3.2 are the best-fit curves, and the dashed regions represent the extrapolations outside the three fit data points. The $k = 1$ line shows an independent, very small amplitude data point at 0.033 A, representing a measurement taken under conditions well away from any experimentally detectable voltage second harmonic. The 0.033 A points are seen to lie on the extrapolated linear fit made from the 0.3, 0.4, and 0.5 A data. The calculated $\tilde{Z}_{1,1}$ value from fitting the three larger amplitude points in Figure 3.2a is $\tilde{Z}_{1,1} = 37.31 \pm 0.17 m\Omega$. The value measured from the traditional small amplitude 0.033 A modulation, where there is no $k = 2$ peak, is $\tilde{Z}_{1,1} = 37.37 m\Omega$, well within the confidence interval of the larger amplitude value. Moreover, all $\tilde{Z}_{1,1}(\omega_1)$ linear impedances calculated from the 0.3, 0.4, and 0.5 A points were found to satisfy Kramers-Kronig relations[106] to within 1.0% (see the Supplementary Jupyter Notebook).[105]

The results shown in Figure 3.2 are consistent across our wide range of frequency response data, and they support the hierarchical mathematical structure of Equation 3.5. Specifically, our results and the math show it is possible to *simultaneously, self-consistently, and accurately* determine the $\tilde{Z}_{1,1}$ spectrum from $k = 1$ voltage data (that scale with ΔI) and the

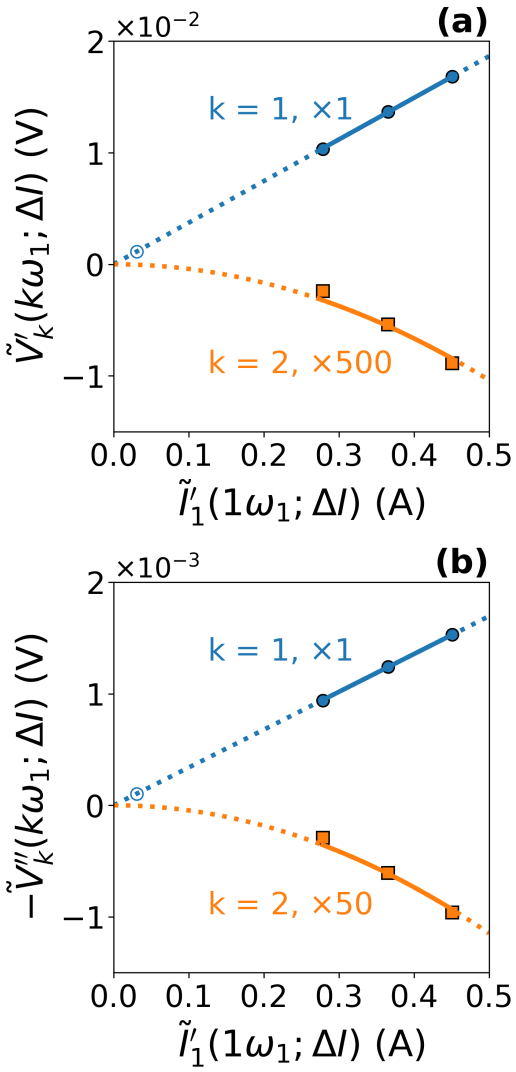

Figure 3.2: Amplitude dependence of the real (a) and imaginary (b) components of the Fourier transformed voltage response ($\omega_1 = 0.5$ Hz) as a function of the current perturbation amplitude, ΔI. The first ($k = 1$, ●) and second (k = 2, ■) voltage harmonics are fit to linear, $\tilde{I}'(1\omega_1;\Delta I)\tilde{Z}_{1,1}(\omega_1)$, and quadratic, $\tilde{I}'(1\omega_1;\Delta I)^2\tilde{Z}_{2,2}(\omega_1)$, functions of the measured perturbation amplitude, respectively. The real and imaginary second harmonic data are multiplied by 500 and 50, respectively, to place them on the same scale as the linear response. The data shown are for cell 5 at 30% SoC.

$\tilde{Z}_{2,2}$ spectrum from $k = 2$ voltage data (that scales with ΔI^2), because the leading order truncation error in $\tilde{Z}_{1,1}$ scales with $\sim O(\Delta I^3)$. Stated another way, there is no fundamental reason the presence of an easily detected second harmonic in the voltage spectrum is indicative that the linear impedance is corrupted by nonlinear effects. Instead, the math suggests that a cautionary signature of nonlinearity corrupting EIS is the presence of a third harmonic in the voltage spectrum (i.e., $k = 3$ signature), because that harmonic scales with ΔI^3, just like the truncation error in $\tilde{Z}_{1,1}$. The experimental implication is that we chose current modulation amplitudes of 0.3, 0.4, and 0.5 A for the battery under test, because these values are a good compromise between measurable second harmonics but negligible third harmonics in the voltage spectra. Systematic deviations from linear or quadradic dependences on perturbation amplitude would necessitate the inclusion of additional higher order terms in Equations 3.6 or 3.7, respectively.

As noted in the discussion of Equation 3.4, the galvanostat (like all amplifiers) is imperfect and generates harmonic distortions; these instrument-induced signals are expected to appear in the input current and output voltage spectra. To assess the magnitude and remove galvanostat-generated second harmonic in the voltage output, we use a $\tilde{Z}'_{1,1} = 21\ m\Omega$ resistive wire that is comparable in magnitude to the impedance of the batteries under test, but has no intrinsic nonlinear harmonic generating behavior. Using the same analysis of $k = 2$ voltage spectra as shown in Figure 3.2, we find the purely linear resistor produced a frequency invariant $\tilde{Z}'^{in}_{2,2} = 4.56 \times 10^{-5}\ \frac{\Omega}{A}$ that is associated with the instrument. In all of the second harmonic NLEIS spectra we report, this instrument value is subtracted from each $\tilde{Z}_{2,2}(\omega_1)$ point to remove the small instrument offset.

3.3.3 Nyquist representation of linear and nonlinear EIS spectra

Measuring the linear and nonlinear impedance coefficients over a range of frequencies provides insights into the system at different physicochemical timescales. Figure 3.3 shows a Nyquist representation of the experimentally measured linear EIS spectrum, $\tilde{Z}_{1,1}(\omega_1)$, and second harmonic NLEIS spectrum, $\tilde{Z}_{2,2}(\omega_1)$, for a fresh cell at 50% state-of-charge (SoC). The linear

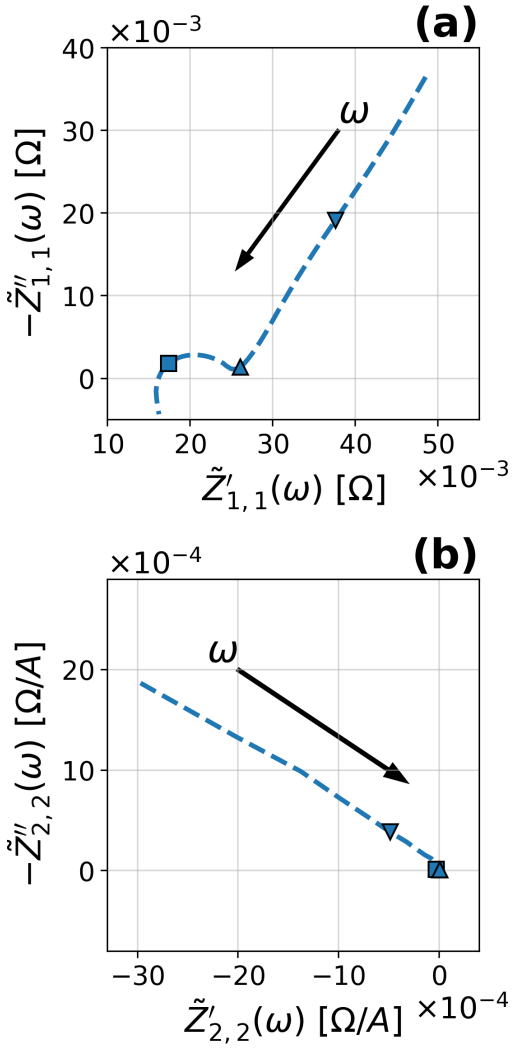

Figure 3.3: Nyquist plots of measured first (a) and second (b) harmonic coefficients, $\tilde{Z}_{1,1}(\omega_1)$ and $\tilde{Z}_{2,2}(\omega_1)$ of "fresh" battery at 50% SoC. The data at 1 kHz (■), 1 Hz (▲), and 10 mHz (▼) are labeled for clarity.

response shown in Figure 3.3a is a typical EIS spectrum for a lithium-ion battery. Figure 3.3a has a high frequency real-axis intercept (>1 kHz) related to the internal resistance of the battery, a mid-range frequency arc (∼1 kHz to 1 Hz) attributable to the coupled charge transfer kinetics and double-layer capacitance of the porous electrodes, and a low frequency tail (<1Hz) attributable to diffusive transport and thermodynamics. The linear EIS spectra we are measuring can be thought of as the sum of two half-cell impedances for the positive and negative electrodes,

$$\tilde{Z}_{1,1} = \tilde{Z}^{+}_{1,1} + \tilde{Z}^{-}_{1,1} \tag{3.8}$$

where each half cell is defined at the mid-plane of the separator. Analysis of linear EIS spectra using equivalent circuit modeling is common in the literature, where circuit elements can be related to characteristics of the electrodes and separator.[3,102,107,108]

Prior work[75] shows that the second harmonic response is highly sensitive to several forms of symmetry in the system under test. The second harmonic NLEIS spectra we are measuring can be thought of as the difference between the half-cell impedances for the positive and negative electrodes,

$$\tilde{Z}_{2,2} = \tilde{Z}^{+}_{2,2} - \tilde{Z}^{-}_{2,2} \tag{3.9}$$

In a symmetric cell, where the positive and negative electrodes are identical, $\tilde{Z}_{2,2}$ will be identically zero for all frequencies. Of course, a functional battery is not a symmetric cell because thermodynamic differences in each electrode material largely defines the battery. Figure 3.3b shows that essentially all of the $\tilde{Z}_{2,2}$ response, for a fresh cell at 50% SoC, occurs at frequencies below 1 Hz, where cell thermodynamics and diffusive transport are expected to be the dominating physics.

In the mid-frequency regime (>1 Hz), where interfacial kinetic/capacitive processes dominate the linear EIS spectrum of Figure 3.3a, we see negligible $\tilde{Z}_{2,2}$ second harmonic response. In our full-physics model of lithium ion batteries, the lack of kinetic/capacitive response in $\tilde{Z}_{2,2}$ was attributed to high symmetry charge transfer where $\alpha_a = \alpha_c$ in the Butler-Volmer expression.[75] To get a basic understanding of charge transfer symmetry in the linear and

nonlinear impedance, we carry out a Taylor series expansion of the Butler-Volmer equation,

$$j = i_0 \left[\exp\left(\frac{\alpha_a F}{RT}\eta\right) - \exp\left(\frac{-\alpha_c F}{RT}\eta\right) \right] \tag{3.10}$$

and include the first two terms

$$j = \left[\frac{i_0(\alpha_a + \alpha_c)F}{RT}\right]\eta + \left[\frac{i_0(\alpha_a^2 - \alpha_c^2)F^2}{2R^2T^2}\right]\eta^2 + O(\eta^3) \tag{3.11}$$

where i_0 is the exchange current density, α_a and α_c are the anodic and cathodic transfer coefficients, and F, R, and T are Faraday's constant, the gas constant, and the temperature, respectively. The first term on the right-hand side of Equation 3.11 is the inverse of the classic linear charge transfer resistance whereas the second term describes the leading order nonlinear behavior. Note that the second term is zero when charge transfer is symmetric with $\alpha_a = \alpha_c$, but can be either positive or negative when $\alpha_a \neq \alpha_c$.

The classic, linear charge transfer resistance in EIS is insensitive to symmetry because $\alpha_a + \alpha_c$ is a constant (the number of electrons transferred) for each electrode. On the other hand, the second term of Equation 3.11, when combined with Equation 3.9, provides a symmetry-dependence that is consistent with our full-physics battery model behavior when $\alpha_a = \alpha_c$, $\alpha_a > \alpha_c$ or $\alpha_a < \alpha_c$ for either or both electrodes.[75] Thus, we can think of the second term in Equation 3.11 as being related to a "second harmonic charge transfer resistance" for each electrode. The absence of second harmonic NLEIS features at interfacial kinetic/capacitive frequencies in Figure 3.3b suggests charge transfer on both "fresh" electrodes is symmetric.

3.3.4 State-of-Charge (SoC) dependence for fresh cells

The full physics theory for linear EIS and second harmonic NLEIS includes explicit state-of-charge (SoC) dependence through derivatives of the open circuit potential of each electrode, and implicit dependence on parameters such as diffusivities, interfacial capacitances, and

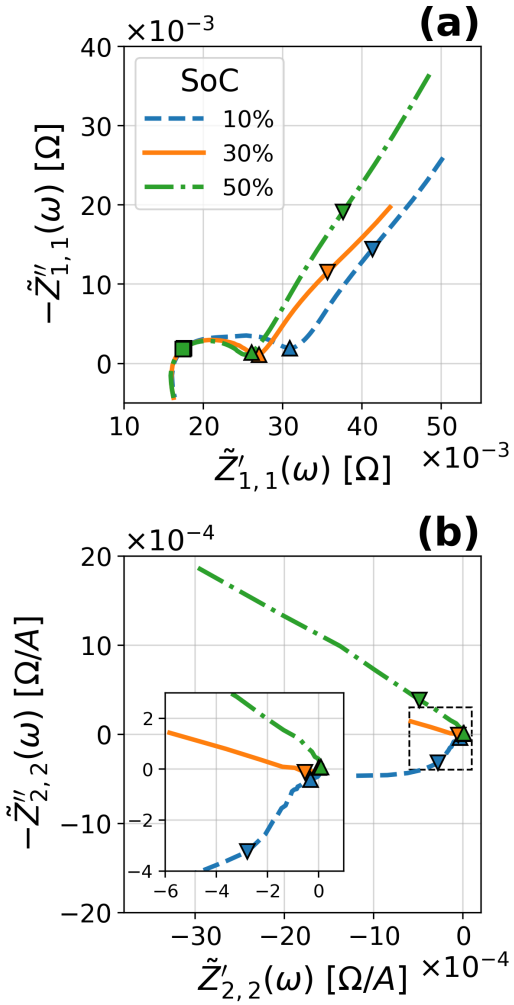

Figure 3.4: Nyquist plots of measured first (a) and second (b) harmonic coefficients, $\tilde{Z}_{1,1}(\omega_1)$ and $\tilde{Z}_{2,2}(\omega_1)$, for a "fresh" cell at several states-of-charge. The data at 1 Hz (▲) and 10 mHz (▼) are labeled for clarity and the inset in (b) shows the region near the origin in more detail.

charge transfer parameters.[75] Specifically, linear EIS response depends on the first derivatives of the open circuit voltages with respect to intercalated lithium content; the first derivative is always negative for either electrode, but the magnitudes can vary widely by material and SoC. The second harmonic NLEIS response depends on both the first and second derivative with respect to intercalated lithium content; the second derivative can be positive, negative, or zero for either electrode. As a result of the additional parameters, their varied signs, and the fact the response comes from differences between electrodes, per Equation 3.9, our theory suggests that the thermodynamics/diffusion dominated regions of second harmonic NLEIS spectra can display a much richer set of SoC-dependent behaviors compared to the Warburg-like behavior expected for linear EIS.[75]

Figure 3.4 shows the linear EIS and second harmonic NLEIS spectra as the SoC is varied from 50% (same as Figure 3.3) to 10% in a fresh cell. The accompanying Supplemental Jupyter Notebook includes data for other SoCs, but they are excluded from Figure 3.4 for clarity.[105] The series of linear EIS spectra in Figure 3.4a all have characteristic mid-frequency arcs associated with interfacial kinetic/capacitive behavior ($\omega_1 >$ 1 Hz) and low frequency thermodynamic/diffusive tails ($\omega_1 <$ 1 Hz). The interfacial charge transfer impedance grows systematically as the SoC is reduced. The low frequency EIS tail displays subtle changes in length with state-of-charge, being longest at 50% SoC, shortest at 30%, and longer again at 10%. Based on the full physics EIS model presented elsewhere, the mid-frequency changes are likely to be driven by SoC-dependent changes in exchange current density (i_0) and double-layer capacitance (C_{dl}) on one or both electrodes. The low frequency response is typically driven by SoC-dependent changes in the first derivative of open circuit voltage and solid-state diffusivity on one or both electrodes, though other transport processes can also come into play.[59,75] The effects of these changes are additive, per Equation 3.8.

The second harmonic spectra in Figures 3.4b show much greater variation in behavior than the linear EIS as the SoC changes. Despite large variation in the low-frequency region, no spectra show significant responses in the interfacial kinetic/capacitive regime ($\omega_1 >$ 1 Hz), see inset in Figure 3.4b. As discussed above, the lack of significant second harmonic

response in the mid-frequency regime indicates symmetry of charge transfer over all states-of-charge tested. The complexity of the low-frequency second harmonic NLEIS response is not surprising given the increased number of parameters controlling the behavior, as described above. Moreover, the fact that the NLEIS spectrum results from differences in each electrode, Equation 3.9, means that subtle changes in one electrode can be amplified. In theory, this increased sensitivity to parameter changes improves parameter identifiability, but the more complex dependencies of NLEIS means that more sophisticated analysis is required. We will explore detailed SoC-dependent analysis and parameter estimation of NLEIS spectra in future work.

3.3.5 State-of-Health (SoH)

We have begun to explore the sensitivity of second harmonic NLEIS as a method for state-of-health (SoH) assessments. Figure 5 shows the linear EIS and second harmonic NLEIS spectra at 30% SoC for the fresh Samsung power cells and cells that have been charged and discharged at 2C for 100 cycles. The measured capacity loss from this cycle-dependent aging is small, only 0.8%, implying small changes to physicochemical processes in the battery.

EIS is valuable for prognostic and diagnostic analysis of battery aging.[16] Here we see the linear EIS response in Figure 3.5a is noticeably changed in the mid-frequency kinetic/capacitive regime, despite less than 1% degradation of capacity. In particular, the mid-frequency impedance has grown, and two distinct arcs are now visible in the aged cell. For LiNMC|C cells, the growth of a second mid-frequency kinetic/capacitive arc from cycling is typically attributed to an increase in the positive NMC electrode charge transfer resistance.[101] The highest frequency arcs for fresh and aged cells continue to overlap in Figure 3.5a, suggesting negligible changes to the negative electrodes from 100 cycle aging. Likewise, aging related changes in the low frequency tail are extremely subtle.

While linear EIS provides useful insights, Figure 3.5b shows second harmonic NLEIS produces much greater changes from 100 cycle aging than linear EIS; we find all measurable frequencies are distinctly altered in the aged cell. In particular, the emergence of a

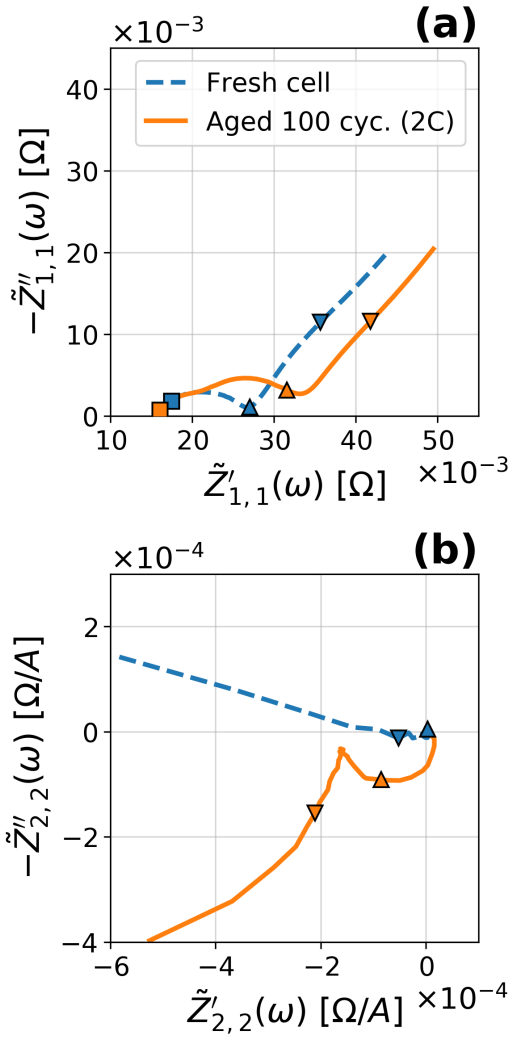

Figure 3.5: Nyquist plots of measured first (a) and second (b) harmonic coefficients, $\tilde{Z}_{1,1}(\omega_1)$ and $\tilde{Z}_{2,2}(\omega_1)$ for a fresh cell and a cell which has been cycled 100 times at 2C. The data at 1 kHz (■), 1 Hz (▲), and 10 mHz (▼) are labeled for clarity. The second harmonic data is truncated at 10 Hz. Cells are at 30% SoC.

mid-frequency response in the aged cell indicates a breaking of charge-transfer symmetry for at least one electrode. Combining the EIS interpretation with the new NLEIS results here suggests the positive NMC electrode ages with an increase in linear charge transfer resistance (i.e., decreasing i_0) and that change is accompanied by a breaking of charge transfer symmetry (i.e.,$\alpha_a \neq \alpha_c$).

Previous full-physics theory results show that the "second harmonic charge transfer resistance," as we called it above, can be either positive or negative depending on the direction of charge transfer asymmetry and the electrode where that asymmetry arises.[75] Using these prior results, and attributing all the degradation to the positive electrode, means the charge transfer arc in Figure 3.5b arises from the anodic transfer coefficient, $\alpha_{a,pos}$, being larger than the cathodic transfer coefficient, $\alpha_{c,pos}$. For a positive electrode with $\alpha_{a,pos} > \alpha_{c,pos}$, oxidation (charging) is relatively easier (requires lower overpotential) than the equivalent reduction (discharging). This new insight into mechanistic changes in charge transfer cannot be determined from EIS alone, as linearization of the governing equations (and the governing physics) makes EIS wholly insensitive to charge transfer symmetry in either electrode.

As described in Figure 3.4b, the low frequency tail is sensitive to subtle changes in several thermodynamic and diffusive transport parameters for either or both electrodes. As noted above, the sensitive, multi-parameter nature of the NLEIS low frequency domain makes attention to modeling more essential for interpretation. Overall, second harmonic NLEIS appears to complement linear EIS as a method for probing degradation processes at the earliest stages of cycling.

3.3.6 Physics-based modeling of the EIS and NLEIS spectra

All of the experimental observations we have made in Figures 3.3-3.5 can be represented by our previously developed pseudo 2-dimensional (P2D) physics-based model for the linear EIS and second harmonic NLEIS response of a lithium-ion battery.[73] We are currently building up the computational tools needed for multi-parameter estimation of linear EIS and second harmonic NLEIS based on full-physics parameter estimation fit to experiments.[109] However, even without best-fit parameters, it is possible to qualitatively demonstrate that important characteristics of the linear and nonlinear response for the battery can be captured by the model. For example, Figure 3.6 shows simulated spectra that qualitatively mirror the EIS and NLEIS aging results presented in Figure 3.5; the two sets of model parameters are given in Table A3.2.

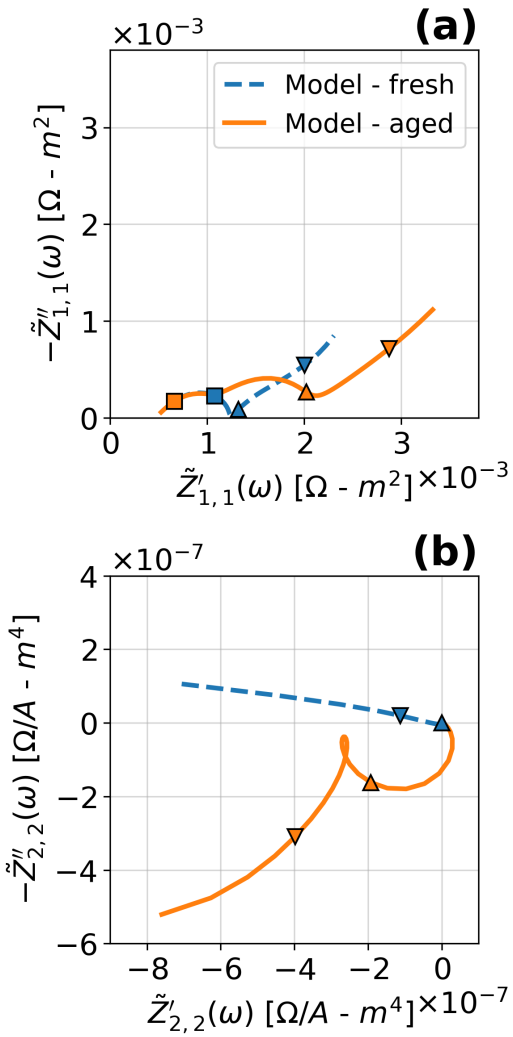

Figure 3.6: Nyquist plots of computed first (a) and second (b) harmonic coefficients, $\tilde{Z}_{1,1}(\omega_1)$ and $\tilde{Z}_{2,2}(\omega_1)$ from 3.16 mHz to 10kHz. The data at 1 kHz (■), 1 Hz (▲), and 10 mHz (▼) are labeled for clarity.

In the aged cell experiments, the appearance of two distinct kinetic/capacitive arcs in the EIS spectrum was attributable to growth of the charge transfer resistance and an increase in the characteristic "RC" time constants for the positive electrode. The main way the model captures this aging affect is by a large reduction in positive electrode i_0 and large increase in double-layer capacitances C_{dl} for both electrodes. Changes to the charge transfer symmetry have no effect on the linear EIS. Further, looking at Table A3.2, we see that many of the thermodynamic and diffusion parameters are changed for the aged cell, but these changes only produce subtle differences in the linear EIS spectrum at low frequencies, similar to the experimental observations in Figure 3.5a.

As noted in the discussion of Figure 3.5b, aging qualitatively changes everything about the second harmonic NLEIS spectrum; that behavior is mirrored by our model. As expected, symmetric charge transfer coefficients ($\alpha_a = \alpha_c = 0.5$), for both electrodes, produce a low frequency curve that goes straight toward the origin, as seen with the "fresh cell" model parameters. In this case, there are no mid-frequency kinetic/capacitive features. Introducing asymmetry in the transfer coefficients of the positive electrode, ($\alpha_{a,pos} = 0.55$, $\alpha_{c,pos} = 0.45$) results in the characteristic second harmonic kinetics arc seen in Figures 3.5b and 3.6b. At low frequencies, the changes in thermodynamic and diffusion coefficients for both electrodes drive a radically different low frequency second harmonic NLEIS response, despite having only modest impact on the linear EIS response. The impact of charge transfer symmetry on the second harmonic signature is further illuminated in Figure 3.7. The effect of varying the positive electrode anodic transfer coefficient, $\alpha_{a,pos}$, for three cases where $\alpha_{a,pos} = \alpha_{c,pos}$, $\alpha_{a,pos} > \alpha_{c,pos}$ and $\alpha_{a,pos} < \alpha_{c,pos}$, is shown. The result shows that, depending on the nature of the asymmetry, the "second harmonic charge transfer resistance" can be positive or negative and its sign defines the quadrant of the resulting kinetic/capacitive arc. A similar, but inverted, dependence on symmetry exists for the negative electrode, because of the effect Equation 3.9 has on the total cell response. We are exploring scaling relationships and analytical approaches for relating the second term of Equation 3.11 to the quantity we refer to as the "second harmonic charge transfer resistance", which we think of as a nonlinear

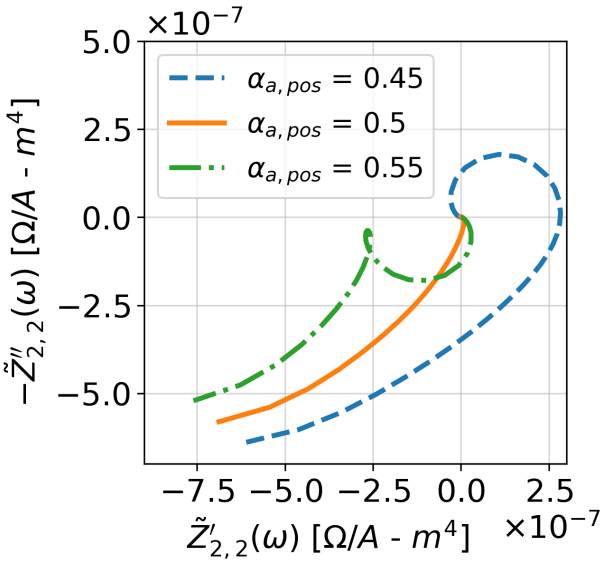

Figure 3.7: Nyquist plots of simulated second harmonic spectra, $\tilde{Z}_{2,2}(\omega_1)$ for varying positive electrode anodic transfer coefficients, $\alpha_{a,pos}$ (with $\alpha_{c,pos} = 1 - \alpha_{a,pos}$).

analog to the Randles circuit; we will report on those results later.

3.4 Conclusions and Implications

Nonlinear electrochemical impedance spectroscopy (NLEIS) can be implemented as an add-on to traditional linear EIS by using a modestly larger input current or voltage modulation and advanced signal processing. Our experiments and analysis show that NLEIS provides complementary information to EIS; this new information helps unlock insights into the charge-transfer kinetics, thermodynamics, and mass transport processes that govern lithium-ion batteries. We lay out the experimental method and complications, as well as the mathematical framework for analysis of NLEIS. State-of-charge and state-of-health data for a fresh and cycled commercial Samsung LiNMC|C cell is used to illustrate the sensitivity of NLEIS.

There is a general notion that the existence of higher harmonics in the output voltage or current spectrum necessarily means EIS data is corrupted by nonlinear phenomenon.[21,23–26] Instead, we show that the general mathematical form of the weakly nonlinear regime does

not support this as a universal premise. Specifically, assuming current is modulated with amplitude ΔI, the mathematical truncation error associated with a linear impedance measurement is $\sim O(\Delta I^3)$, whereas the second harmonic output is an $\sim O(\Delta I^2)$ signal. Thus, it is generally possible to find input modulation amplitudes where first order (EIS) and second order (second harmonic NLEIS) effects dominate third order effects (error in the EIS signal and third harmonic NLEIS). Of course, the exception to this statement is a symmetric electrochemical system with identical electrodes; the second harmonic output is identically zero at all frequencies for a symmetric cell. Fortunately, functional whole batteries are always asymmetric cells. For our experiments with 1500 mAh power cells, input current modulations up to 500 mA produced fundamental peaks on the order of 10s of millivolts, second harmonics several orders of magnitude smaller, and no measurable third harmonic. Experiments showed that EIS results acquired under these conditions matched much smaller modulations, and satisfied Kramers-Kronig relationships to within 1% error at all frequencies.

It is worth reiterating here that instrumental limitations constrained the usable frequency range for second harmonic NLEIS spectra to $\omega_1 \leq 10$ Hz because of the total harmonic distortion that was generated by the galvanostat for these low impedance cells. Thus, we were unable to achieve high enough frequencies to fully probe the negative electrode kinetic/capacitive regime. It is worth noting, however, if the higher frequency electrode possessed asymmetric charge transfer, the effect would be reflected in the lower frequency second harmonic as a real axis offset from the origin. Consequently, improvements in instruments that enable larger current modulations for low impedance batteries are crucial for accurately probing smaller, and higher frequency, physicochemical processes with NLEIS.

A tantalizing view into the power of combining NLEIS experiments with NLEIS physics-based models was provided in the analysis of cell aging. We used a previously developed physics-based linear EIS and second harmonic NLEIS model to interpret the second harmonic response's sensitivity to charge transfer symmetry at mid-frequency ranges, as well as thermodynamic and mass transport parameters at low frequencies. The aged batteries, despite losing less than 1% of capacity from cycling, showed a fundamentally different signature in

the nonlinear response due to the presence of asymmetric charge transfer kinetics. The measurable effects of the transfer coefficients, which have not been detectable in standard EIS, can now be monitored with aging, and at various states of the battery. This ability to more completely measure fundamental aspects of charge transfer, such as symmetry coefficients in situ and in whole cells, is a potentially important advance. We are working on the tools to extract quantitative parameters from combined EIS and second harmonic NLEIS.

Finally, it is worth assessing a potential consequence of increasing the current modulation amplitude, namely, the increase in battery temperature rise during test. To estimate this, the time-averaged Joule heating rate, $q_j = \frac{1}{2}\left|\tilde{Z}_{1,1}(\omega_1)\right| \Delta I^2$, is equated to the rate of heat dissipation from Newton's law of cooling, $q_N = hA\langle\Delta T\rangle$, where $\langle\Delta T\rangle$ is the steady-state temperature rise in the cell. Natural and forced convective heat transfer for cylindrical batteries have been reported to have coefficients as low as 10 $\frac{W}{m^2 \cdot K}$ and 100 $\frac{W}{m^2 \cdot K}$, respectively.[110–112] Using conservative parameters that bias toward high temperature rise ($|\tilde{Z}_{1,1}(\omega_1)| = 64\ m\Omega$, $A = 0.00419\ m^2$, and $\Delta I = 0.5\ A$), yields $\langle\Delta T\rangle = 0.19$ °C and 0.019 °C for natural convection and forced convection, respectively. Since the temperature chamber is constantly recirculating air using fans, the steady-state temperature of our battery under test is likely to be within this range. Though the temperature rise estimated here is small, there are many assumptions that underpin this simple analysis. It may be worth looking at more sophisticated thermal models of NLEIS testing in future work.

Acknowledgments.—This work has been partially supported by funding from the Boeing-Sutter Endowment, as well as an U.S. NSF Integrative Graduate Education and Research Training grant fellowship to M.D.M (DGE-1258485) and NSF National Research Training Grant fellowship to V.W.H (DGE-1633216). The authors would like to thank Cleo Tsang and Stephanie Reusch who performed some of the initial experimental work. This work was performed in the advanced characterization labs at the Washington Clean Energy Testbeds, an open access instrumentation facility managed by the University of Washington Clean Energy Institute.

3.5 Appendix

Table A3.1: Voltages for NLEIS measurements

State-of-Charge	10%	30%	40%	50%	60%
Voltage	3.500	3.643	3.706	3.820	3.920

Table A3.2: Parameters for simulating fresh and aged NLEIS spectra

Physicochemical Parameters

Name	**Units**	**Fresh Cell**	**Aged Cell**
$Brugg$	—	4	4
$C_{dl,neg}$	$\mu F/cm^2$	10	50
$C_{dl,pos}$	$\mu F/cm^2$	25	1000
c_0	mol/m^3	1000	1000
D	m^2/s	1.5×10^{-10}	7.5×10^{-10}
$D_{s,neg}$	m^2/s	3.9×10^{-14}	9.8×10^{-15}
$D_{s,pos}$	m^2/s	1×10^{-14}	2.5×10^{-15}
$\frac{\partial U_{neg}}{\partial c^s}$	$V \cdot cm^3/mol$	0	-3.21
$\frac{\partial U_{pos}}{\partial c^s}$	$V \cdot cm^3/mol$	-10	-11.7
$\frac{\partial^2 U_{neg}}{\partial c^{s2}}$	$V \cdot cm^6/mol^2$	-100	-400
$\frac{\partial^2 U_{pos}}{\partial c^{s2}}$	$V \cdot cm^6/mol^2$	0	-600
$i_{0,neg}$	A/m^2	29.7	14.85
$i_{0,pos}$	A/m^2	33.0	5.51
t_+^0	—	0.364	0.364
$\alpha_{a,neg}$	—	0.5	0.5
$\alpha_{a,pos}$	—	0.5	0.55
$\alpha_{c,neg}$	—	0.5	0.5
$\alpha_{c,pos}$	—	0.5	0.45
κ	S/m	0.205	.205
σ_{neg}	S/m	100	100
σ_{pos}	S/m	100	100

Geometric Parameters

Name	**Units**	**Fresh Cell**	**Aged Cell**
l_{neg}	μm	88	88
l_{sep}	μm	25	25
l_{pos}	μm	80	80
$R_{p,neg}$	μm	2	2
$R_{p,pos}$	μm	2	2
$\epsilon_{f,neg}$	—	0.0326	0.0326
$\epsilon_{f,pos}$	—	0.025	0.025
ϵ_{neg}	—	0.485	0.485
ϵ_{sep}	—	0.724	0.724
ϵ_{pos}	—	0.385	0.385

Chapter 4

OPEN-SOFTWARE TOOLS FOR THE PHYSICS-BASED ANALYSIS OF EXPERIMENTAL IMPEDANCE SPECTRA

Note: this chapter was published as an article

- Matthew D. Murbach and Daniel T. Schwartz. Analysis of Li-ion battery electrochemical impedance spectroscopy data: An easy-to-implement approach for physics-based parameter estimation using an open-source tool. *Journal of The Electrochemical Society*, 165(2):A297–A304, 2018. DOI: 10.1149/2.1021802jes

Supplementary material can be found on Zenodo.[113,114]

Abstract

The quantitative analysis of electrochemical impedance spectroscopy (EIS) data is important for both characterization and prognostic applications in many electrochemical systems. Here we describe an open-source platform, the ImpedanceAnalyzer, for easy-to-use physics-based analysis of experimental EIS spectra. To demonstrate the use of the platform, we explore the basic capabilities of the pseudo two-dimensional (P2D) battery model to predict publicly available experimental EIS data from a 1500mAh commercial lithium-ion ($LiCoO_2$/graphite) cell. An a priori computed dataset of 38,800 P2D-based impedance spectra simulations, covering a wide range of frequencies (1 mHz to 100 kHz) and model parameters, enables a straightforward least squares matching approach for analyzing experimental spectra. We find an average error of 1.73% between the best-matching computed spectrum from the 38,800 member library and the experimental spectrum being analyzed. Our analysis shows there is significant opportunity to improve the fit between experimental data and physics-based impedance simulations by a combination of a larger computed dataset, local optimization, and further additions to the model physics. The approach and open source tools developed here can be easily extended to other electrochemical systems.

4.1 Introduction

Electrochemical impedance spectroscopy (EIS) is a powerful tool for investigating a wide variety of electrochemical systems.[2,3,115] EIS spectra separate individual electrochemical processes by their characteristic timescales, enabling both qualitative and quantitative analysis of electron transport,[4,5] reaction rates and mechanisms,[6,7] intercalation processes,[8] mass transport,[9,10] and electrode structure.[11,12] The noninvasive nature of EIS also makes impedance measurements useful in prognostic applications such as fuel cell health estimations[13,14] or prediction of remaining useful lifetime in batteries.[15,16]

Qualitative analysis of EIS spectra generally involves assessing the shape of Nyquist plot features to determine the relative importance of different physicochemical processes.[17,18] In contrast, quantitative analysis relies on fitting a model to the data in order extract values for specific thermodynamic, transport, and/or kinetic parameters. Most experimental datasets are analyzed quantitatively using an equivalent circuit analog. Fitting an equivalent circuit to EIS data is straightforward using standard least squares regression techniques.[116,117] A good fit can often be found with a relatively simple equivalent circuit, particularly if non-ideal elements like the constant phase element are used. Moreover, many simple equivalent circuits, like the Randles circuit,[118] have physically interpretable parameters based on linearized electrochemical processes. However, as more complex equivalent circuits are derived and utilized, the lumped parameters can lose their direct physical interpretability and the structure of the equivalent circuit analogs themselves can be degenerate.[20]

An alternative to equivalent circuits for quantitative analysis of EIS data is to directly fit the data with a physics-based mathematical model of the electrochemical system. Many years of electrochemical modeling research have laid the groundwork for the physics-based analysis of impedance in a wide variety of fields including corrosion,[6] hydrodynamic systems,[46,56] fuel cells,[19,57] and lithium-ion batteries.[58–60] Parameter estimation by fitting a physics-based model to experimental EIS data is complicated by the fact that electrochemical models often contain a combination of coupled differential equations, algebraic equations, and dozens of

unknown parameters. For complex physics-based models, convergence to a global best fit is rarely assured, even with an excellent initial guess for the unknown parameters. As a result, parameter estimation methods often need to rely on many independent measurements to drastically narrow the number of fitted parameters.[61] In short, today there is gap between the desire to use physics-based models to estimate parameters in EIS, and the actual (routine) use of physics-based models for parameter estimation from data.

Here we demonstrate an easily implemented and extendable approach for leveraging sophisticated physics-based models of EIS spectra to estimate parameters from experimental data. The parameter estimation approach used in this work relies on error minimization between experimental data and a large library of a priori simulated impedance spectra. One benefit of a dataset-based approach is that it always converges and the resulting parameter estimates are guaranteed to be reasonable if the original dataset was constructed from physically reasonable parameters. Another benefit of a dataset-based approach is that global sensitivity analysis can be used to understand the contribution of different parameters to the model variance.[72] On the other hand, a dataset-based approach will generally not provide the parameters with the lowest possible error between model and experiments.

The work and software tool presented here is extendable to a wide range of electrochemical systems, though our first implementation is using the Doyle-Fuller-Newman pseudo two-dimensional (P2D) lithium-ion battery (LIB) model as the basis for analyzing EIS experiments.[90,91] The earliest uses of LIB physics-based impedance models have been to inform the analysis of experimental EIS data. For example, Doyle et al.[59] used physics-based EIS simulations to show that the low frequency portion of a LIB impedance spectrum appears (qualitatively) to be interpretable as a Warburg impedance, but using a Warburg plot can produce erroneous (quantitative) diffusivity estimates. Subsequently, additional physics has been added to the original P2D model to aid in the interpretation of EIS data. For example, a surface oxide model was added to the positive electrode particles by Dees et al.[61] to understand the increase in interfacial impedance with aging of $LiNi_{0.8}Co_{0.15}Al_{0.05}O_2$-based (NCA) positive electrodes. Abraham et al.[62] extended the model further to interpret the changing

impedance response at different voltages in NCA electrodes.

Despite the widespread use of the P2D model for simulating LIBs — 2 of the top 4 most cited papers in the history of the Journal of the Electrochemical Society (as of November 1st, 2017[119]) — the model has seen limited use for quantitative analysis of experimental impedance data. In this work, we present the ImpedanceAnalyzer, an open-source, web-based analysis platform aimed at making physics-based models as easy to use as equivalent circuits for quantitative analysis of EIS experimental data. For the first implementation, we explore the basic capabilities of the original P2D impedance model to predict publicly available experimental EIS data from a commercial cell. We discuss the implications of this work in terms of the next steps for expanding the model dataset, extending the models physics (surface oxide layers, surface-electrolyte interphase (SEI) layers, etc.), and adding gradient-based parameter estimation to the basic Sobol' parameter sampling method[120] that forms the initial backbone of the ImpedanceAnalyzer. As an open source tool, any of these modifications can be added by other researchers to improve performance. Overall, we believe the open source tools and approach presented here has the capability to combine knowledge generated from decades of physics-based impedance modeling research with the deep materials and chemistry insight of experimentalists to accelerate progress in the field.

4.2 Methods

4.2.1 The pseudo two-dimensional (P2D) lithium ion battery model

The pseudo two-dimensional (P2D) lithium ion battery model We have previously detailed the isothermal P2D model and efficient frequency domain computational approach applied here to prepare a library of simulated lithium-ion battery EIS spectra.[75] Briefly, the P2D model is a set of partial differential equations describing the one-dimensional, volume-averaged distribution of lithium ions and potential in the solid and solution phases across a positive electrode, separator, and negative electrode cell sandwich. In each of the porous electrodes, lithium ion intercalation is assumed to be governed by Fickian diffusion into

spherical particles coupled to Faradaic charge transfer via Butler-Volmer kinetics. The non-Faradaic capacitive currents assume a simple Helmholtz double-layer model. The full set of governing equations, boundary conditions, and parameter dependencies are transformed into the frequency domain by assuming a steady periodic solution form for all dependent variables driven by a single-frequency sinusoidal modulation of applied current. We apply a Volterra series to capture the amplitude-dependence for the linear and weakly nonlinear higher harmonics that result from the single-frequency input current perturbation. Further information showing the model equations used for EIS spectra here are presented in the Appendix AI of our prior work.[75]

The generic Coefficient Form PDE physics module in COMSOL v4.4 was used here for all computations. As noted in earlier work,[75] the highest density of nodes were placed at the interfaces between the solid and solution phases and at the electrode/separator interfaces, based on results from preliminary analysis. For all results presented here, the nodes are distributed in a geometric sequence with the node spacing at the electrode/separator interface 25X smaller than at the center of the separator or at the current collector interface. All 38,800 computed spectra in our EIS library had the same mesh with 250 nodes across the cell sandwich and 8000 elements in the particles. Because of the size of the computed EIS library, we did not use mesh refinement to validate that every individual spectrum was converged, as is normal when a small number of simulations (compared to 38,800) are used. We discuss our strategy for validation of the computational results in §4.3.2. For a given set of physicochemical and geometric parameters and single input perturbation frequency, computing the impedance response took approximately 4 seconds on a Dell Precision T1500 with an Intel Core i7 CPU @ 2.80 GHz and 8GB RAM using a Windows 7 Professional 64-bit operating system. Parameters were updated and the results were saved to disk using the LiveLink for MATLAB version R2013b. The 38,800 member library of EIS spectra (with each spectrum having 25 frequencies) required approximately 2 CPU-months to compute, though much of it could be done in parallel.

4.2.2 Creating a large dataset of simulated spectra

The P2D impedance model as implemented here is parameterized with 26 physicochemical and geometric coefficients. To adequately capture the wide variety of impedance spectra one might encounter for the diversity of lithium-ion battery chemistries, a dataset of different simulations was synthesized using a wide, but physically meaningful, range of parameters. The parameters and their ranges are shown in Table A4.1 in the Appendix. Parameters whose ranges spanned more than two orders of magnitude were sampled logarithmically. Sampling the parameter space of the several dozen inputs to the P2D model necessitates a large number of simulations. The Sobol' sampling sequence[120] was used to efficiently explore the high dimensional space and the SALib[121] and savvy[74] python packages were used to generate the sampling sequences.

An important, but subtle, issue in establishing model parameters is that impedance measurements represent a "local" probe of the battery at the state-of-charge being assessed. The most relevant case for understanding the meaning of "local" is the treatment of electrode thermodynamics. The governing equations for the linear electrochemical impedance (or the weakly nonlinear electrochemical impedance, for that matter[75]) do not rely on knowledge of "global" relationship between open circuit voltage and intercalated lithium concentration. Instead, what matters is the local gradient. Thus, Table A4.1 shows the gradient of open circuit potential with intercalated concentration as a parameter influencing the impedance. The local open circuit voltage gradient values for each electrode are constrained by realistic bounds found in the literature for multiple chemistries. As local variables, the thermodynamic gradients in each electrode are taken as independent parameters to be sampled like all others in Table A4.1.

4.2.3 Incorporating physical knowledge into the validation of many computations

The dataset used in this work currently contains 38,800 impedance spectra each containing 25 frequencies. As the number of computations grows to cover a wide range of parameter and

frequency space, deterministic methods for validating model accuracy such as adaptive mesh refinement or manually verifying the number of node points in high gradient regions become impractical. Leveraging the physical understanding of the electrochemical system provides a crucial insight into exploring the tradeoff between computational time and accuracy.

As an example, in any porous electrode, the competing effects of the solid- and solution-phase conductivities and reaction kinetics determine the distribution of current density within the system.[122] That is, for parameter sets with fast kinetics and low effective conductivities, the zone over which the lithium flux occurs is small, and high gradients form. The location of the reaction zone is driven by the ratio of solid- and solution-phase conductivities. Consequently, for the lithium ion battery system, where electrode conductivities are typically higher than electrolyte conductivity, the region of significant lithium flux density in the porous electrodes tends to be shifted towards the electrode/separator interfaces. Similar considerations occur in the diffusive flux of the oscillating lithium ion concentrations within the solid electrode particles. The penetration depth is governed by Fickian mass transport in the system,

$$\delta_D \approx \sqrt{\frac{D_s}{\omega_1}} \tag{4.1}$$

where D_s is the solid-phase diffusivity and ω_1 is the perturbation frequency. The boundary layer thickness decreases for lower mass transport coefficients and higher frequencies. To account for these regions of high gradients in the concentrations, potentials, and current densities in the system, a high number of node points at the interface between the solid and solution phases and the electrode/separator interfaces were used.

To establish confidence in the large EIS dataset we have produced, we explore the most challenging computational limit (high frequencies) and compare it with the easily calculable analytic limits of infinite frequency. In the limit of infinite frequency, the only contributor to the impedance response is the combined ohmic drop across each of the electrodes and

separator. The internal resistance of the cell has the analytical solution,

$$R_{ohmic} = \left[\frac{l_{pos}}{\sigma_{eff,pos} + \kappa_{eff,pos}}\right] + \left[\frac{l_{sep}}{\kappa_{eff,sep}}\right] + \left[\frac{l_{neg}}{\sigma_{eff,neg} + \kappa_{eff,neg}}\right] \tag{4.2}$$

where l_i is the thickness of the region, and $\sigma_{eff,i}$ and $\kappa_{eff,i}$ are the effective solid- and solution-phase conductivities (given by $\sigma(1-\epsilon_i-\epsilon_{f,i})^{Brugg}$ and $\kappa\epsilon_i^{Brugg}$ where ϵ_i and $\epsilon_{f,i}$ are the void- and filler-fractions and $Brugg$ is a Bruggeman-type tortuosity factor, respectively). Equation 4.2 sets a theoretical lower bound for the computed electrochemical impedance for any set of parameters. Comparisons of high frequency computed solutions to Equation 4.2 for the same parameter set is one way we will assess the numerical accuracy of our large computed dataset over the wide parameter range used.

4.2.4 Fitting computational spectra to experimental data

To directly compare a computed EIS spectrum to an experimental EIS spectrum from a battery with unknown electrode area requires a self-consistent method to determine the superficial electrode area, A_{sup}^m, for every computed spectrum m (here, our computed library has $1 \leq m \leq 38,800$). Superficial area is needed because the computations provide area normalized impedances, with units in $\Omega - m^2$, whereas EIS experimental measurements have units in Ω. For self-consistency, the area used to normalize EIS simulation results must produce a cell capacity that matches the experimentally determined capacity of the battery under test, C_{data} (in Ah), which is a universally measured or reported value. Thus, for every computed spectrum m, the basic procedure is to calculate each electrode's capacity, C_{pos}^m and C_{neg}^m, according to

$$C_i^m = A_{sup}^m l_i^m \left(1 - \epsilon_i^m - \epsilon_{f,i}^m\right) V_i \tag{4.3}$$

where the subscript index i is either pos or neg, A_{sup}^m is the unknown superficial area (in m^2), and V_i is the volumetric capacity (in Ah/m^3) of the material in each electrode. The self-consistent superficial area is the only unknown when the capacity-limiting electrode from

each computed spectrum m is equated to the experimental capacity data by

$$C_{data} = \min\left(C^m_{pos}, C^m_{neg}\right). \tag{4.4}$$

One last factor often found in experimental data, but absent from computed spectra, is contact resistances ($R_{contact}$ in Ω). Uncompensated contact resistance leads to a shift along the real axis that will produce poor or erroneous fits to experiments. Thus, we use contact resistance as a free parameter to minimize the residual error E^m between the experimental data and an area-scaled spectrum from the computed EIS dataset,

$$E^m = \frac{1}{N}\sum_j^N \sqrt{\left(\left(\frac{Z'_m(\omega_j)}{A^m_{sup}} + R^m_{contact}\right) - Z'_{data}(\omega_j)\right)^2 + \left(\frac{Z''_m(\omega_j)}{A^m_{sup}} - Z''_{data}(\omega_j)\right)^2} \tag{4.5}$$

where $R^m_{contact}$ is the error-minimizing contact resistance for spectrum m, $Z'_m(\omega_j)$ and $Z''_m(\omega_j)$ are the real and imaginary components of the computed impedance values for spectrum m at frequencies ω_j, $Z'_{data}(\omega_j)$ and $Z''_{data}(\omega_j)$ are the experimentally measured real and imaginary impedance data at frequencies ω_j, and N is the total number of frequencies being fit. No weighting of the data with frequency is currently implemented.

Because $R^m_{contact}$ is the only fit parameter to minimize error, it can be aphysical. We eliminate any spectrum from consideration if the best-fitting $R^m_{contact}$ is negative and appreciable (here appreciable is taken to mean a magnitude greater than 10% of the high frequency limit). The residual error for all simulated spectra can then be ranked from lowest to highest error to determine the top matches for an experimental spectrum.

4.3 Results

4.3.1 Flexibility of physics-based modeling

Due to the large ranges over which the physicochemical and geometric parameters were sampled, the resulting dataset of simulated impedance responses contains spectra of a wide variety of shapes in the Nyquist diagram. Figure 4.1 shows some of the variation among the

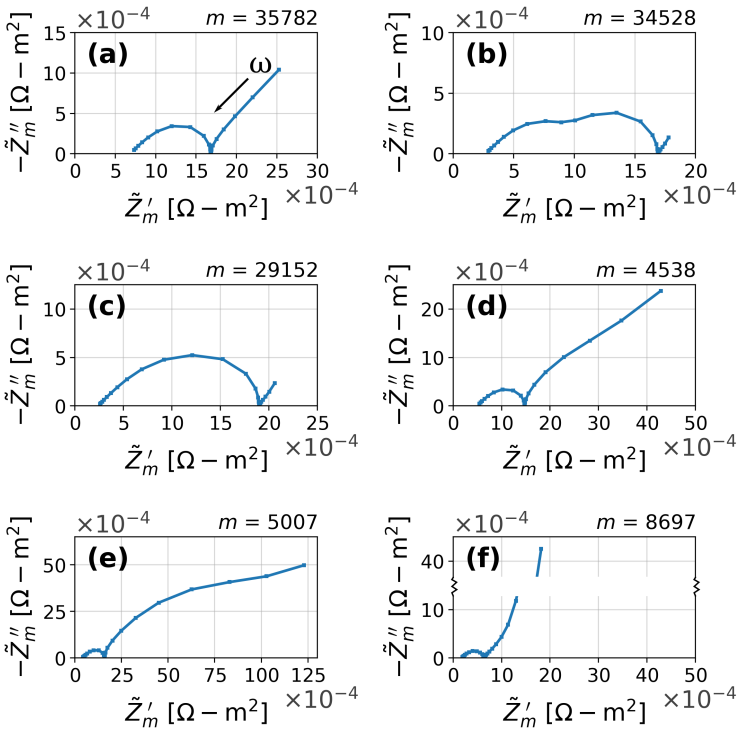

Figure 4.1: Nyquist plots for six of the 38,800 simulated impedance spectra. The spectra shown represent a wide range of impedance responses across the input parameter space with (a) small and (b) large separation between the kinetic arcs, (c) small and (d) large low frequency Warburg-like "tails", and (e) flat and (f) steep low frequency responses. All spectra are shown with 25 logarithmically spaced frequencies from 10^5 Hz to 10^{-3} Hz.

38,800 computed spectra demonstrating the flexibility of the P2D model to capture distinct impedance responses. Figure 4.1a and 4.1b show the Nyquist representation of the simulated spectra with one overlapping (Fig. 4.1a) or two separable (Fig. 4.1b) kinetic arcs. The arcs are related to the interfacial charge transfer resistance and double-layer capacitance at the two electrodes. When the two kinetic impedance responses are similar in magnitude, but differ in characteristic time constants, separate arcs (or a flat long arc) are visible. When either a single electrode has extremely facile kinetics (low charge transfer resistance) or the electrodes have similar kinetic time constants, a single arc defines the mid-frequency impedance response. Consequently, a wide range of high- to mid-frequency responses are seen in the simulated dataset without the requirement on introducing unphysical or nonideal

circuit elements like the constant phase element. Similarly, despite the typical treatment of fitting a single Warburg element, the low-frequency response also encompasses a diverse range of features. Figure 4.1c shows an impedance spectrum with a small low-frequency response while Figure 4.1d shows an impedance spectra with a comparatively large contribution in the same frequency range. In the low-frequency regime, solid- and solution-phase mass transport as well as thermodynamics (derivatives in the open circuit potential) interact to generate distinct variations in the impedance responses. As an example, Figure 4.1e and Figure 4.1f show the effect of an impedance spectrum with a relatively flat low-frequency feature and a steeply sloped feature, respectively. It should be noted that there is no need for the spectra in Figure 4.1 to be scaled by superficial area or shifted by inclusion of uncompensated contact resistance since we are not comparing to experimental results, and therefore, the figure units are $\Omega - m^2$.

4.3.2 Assessing the quality of the simulation library

Preliminary studies were carried out to determine a meshing strategy that worked for a wide range of parameters and frequencies. The goal of the preliminary work was to balance the number of mesh nodes and their spatial distribution, with the computational time required to compute a converged solution. Given the wide range of parameters used, and the 38,800 unique parameter combinations explored at 25 frequencies (970,000 computations of the governing equations and boundary conditions), it was not easy to evaluate the accuracy of every computation. Nonetheless, we had a strategy to ensure the numerical approach and meshing was appropriate. In particular, we explored the hardest-to-converge limit of the governing equations, high frequencies, by comparing the simulated high-frequency data to the analytical high-frequency limit given by Equation 4.2.

Figure 4.2 shows a comparison of the simulated high-frequency real impedance at 10^5 Hz and the analytically predicted value of the ohmic resistance. An initial indicator of computational quality is seen immediately; Equation 4.2 is the theoretical lower bound for the real impedance, and we see that all simulations lie on or above the diagonal line, with none

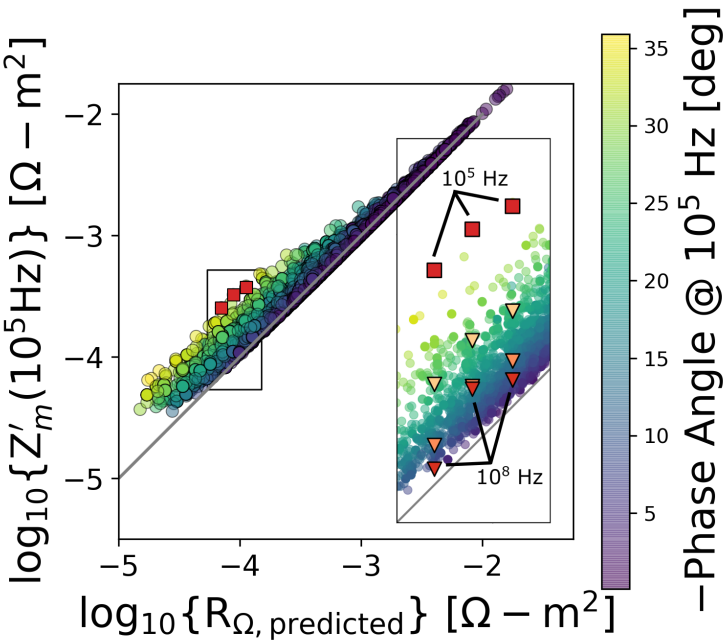

Figure 4.2: Comparison between the 38,800 simulated data points for the highest frequency used here, $Z'(10^5 Hz)$, and the analytic ohmic resistance for the same parameters, $R_{\Omega,\text{predicted}}$. The marker color indicates the simulated phase angle at 10^5 Hz. Inset shows that some combinations of parameters require a much higher simulated frequency to achieve a purely ohmic response.

below. There are two possible reasons for the simulated impedance at 10^5 Hz to be above the analytically-predicted ohmic (real) resistance: (i) the simulated frequency (10^5 Hz) is insufficient to reach a purely ohmic response for the set of parameters or (ii) numerical errors associated with inadequate meshing. Understanding the origin of the upward deviations we see in Figure 4.2 at low cell resistances is aided by coloring the markers to indicate the computed phase of the calculated impedance at 10^5 Hz for all 38,800 simulations. We see a consistent trend of higher phase angles resulting in greater deviation from the diagonal line which is consistent with the deviation being associated with 10^5 Hz as too low of a frequency to reach the real axis. We can explore this effect statistically. The average deviation from the predicted value for all 38,800 high frequency points is 12.9%, while the error for all spectra with less than a 5.7^o phase angle at 10^5 Hz (68% of the spectra) is 5.0%. In short, the closer

a point at 10^5 Hz is to a purely real number, the more accurately Equation 4.2 predicts the value. This may seem obvious, but there is no reason to believe that inadequate mesh refinement would produce this systematic behavior across such a diverse set of parameters.

To further test the idea that the meshing and computations are adequate, and deviations arise predominantly from the selection of 10^5 Hz as the highest frequency, we further evaluated some of the largest deviating points. The inset in Figure 4.2 shows the decrease in error resulting from increasing the highest simulated frequency from 100kHz to 100MHz, while keeping the grid mesh fixed. We see that all three points move toward the diagonal line, further validating that it is primarily the frequency range used, for certain parameter combinations, not numerical error.

Based on these high frequency and other tests, we have confidence that the systematic deviations seen in Figure 4.2 are not primarily due to numerical error. Moreover, given that we primarily tested the most difficult-to-compute frequency limit of the library, we are confident that meshing-produced numerical errors are at least an order of magnitude below the 5.0% systematic deviation seen for the low phase angle points in Figure 4.2, for all frequencies. Of course, adaptive methods for increasing the density of node points within the high gradient regions would lower the numerical error further, albeit at the significant cost of increased computational time, but there appears little reason to pursue that based on these results.

4.3.3 Using the ImpedanceAnalyzer: A physics-based fit of a $LiCoO_2$/graphite cell spectra

The input panel for the web-based, ImpedanceAnalyzer tool is shown in Figure 4.3. To fit an experimental spectrum, a user would browse for a file on their computer containing a comma delimited file where the first column contains frequency, the second contains the real impedance, and the third contains the imaginary impedance. The type of analysis to be performed is then selected and any additional input (battery capacity for scaling according to Equation 4.4, for example) is entered before clicking the "Go" button to transmit the data to the server for the spectrum matching and ranking process described above.

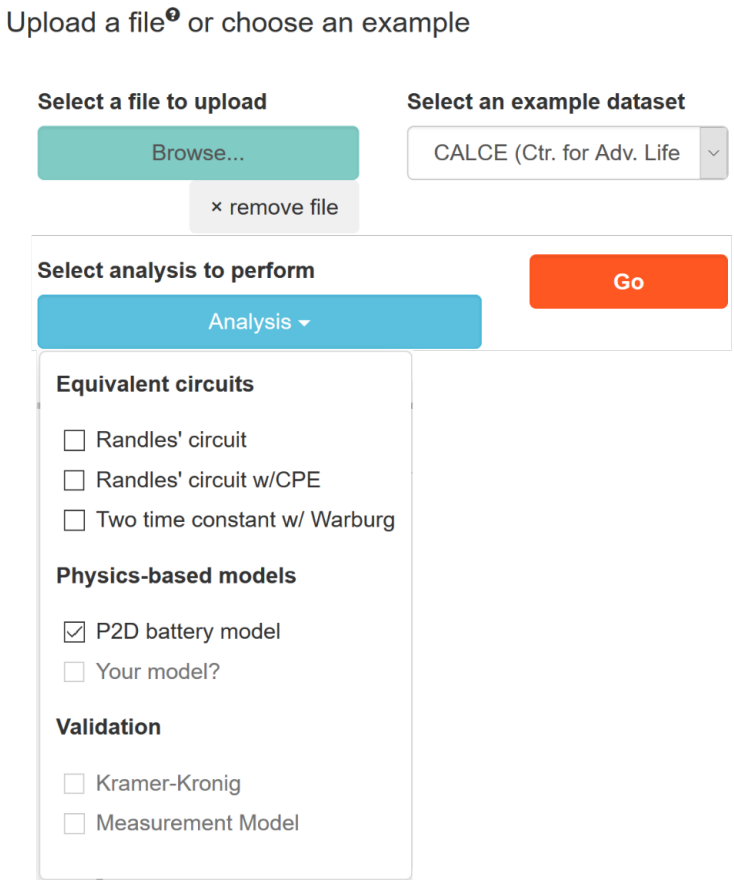

Figure 4.3: Input panel of the ImpedanceAnalyzer. Users would select a file to upload or an example dataset as well as analysis to perform before selecting "Go"

To demonstrate the process, an example experimental impedance spectrum is taken from the University of Maryland's Center for Advanced Life Cycle Engineering (CALCE) Battery Data Archive.[123] The spectrum shown here comes from the initialization impedance measurements on a 1500mAh LiCoO2/graphite battery cell (Cell 41 in the PLN Initialization Dataset).[124] The impedance response of the pouch cell was measured from 1.64 kHz to 12.5 mHz. The Nyquist representation of the raw experimental data is shown in Figure 4.4a. The spectrum consists of a depressed semicircle in the frequency range associated with interfacial processes and a low-frequency tail in the region associated with mass transport and thermodynamic processes. As a part of the spectrum ranking process, the experimentally sampled

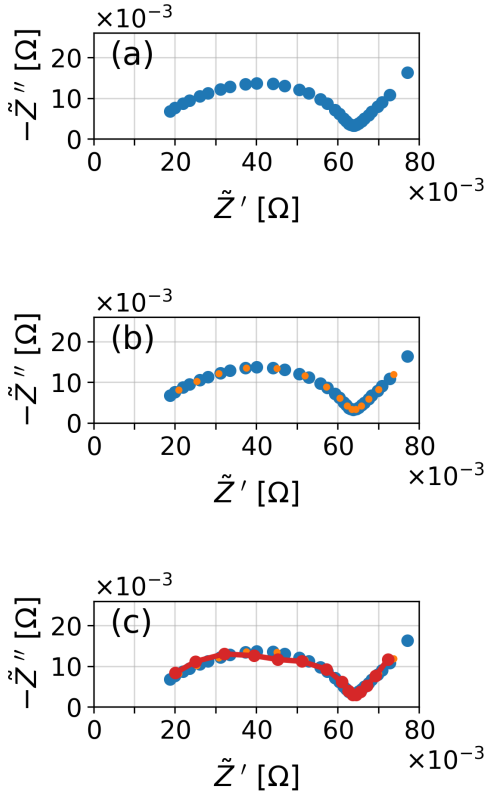

Figure 4.4: Nyquist plots of the (a) raw experimental spectra, (b) interpolated fit points, and (c) best matching simulated spectra (m = 6230) from the 38,800 computed datasets. The average error between the simulated spectra and experimental data in (c) is 1.73% with a contact resistance of 4.2 mΩ and superficial area of 300.32 cm^2.

frequencies are quadratically interpolated to match the simulated frequencies (Figure 4.4b) and then the process described above determines the simulated spectra from the dataset with the lowest residual error (Figure 4.4c). The resulting closest match for this example spectra and the P2D dataset described above has a run index, m, of 6230, a superficial area, A_{sup}, of 300.3 cm^2, a contact resistance, $R_{contact}$, of 4.21 mΩ, and an average residual error, E, of 1.73%. In this case, the positive electrode provides the limiting capacity. The parameters which generate the closest match are returned to the user in the web tool and are shown in Table A4.2 in the Appendix. It should be noted that the experimental dataset used here has the data truncated at a moderate frequency and, thus, the spectrum contains negligible

influence from the inductance often found experimentally at high frequencies. For datasets that contain higher frequencies, there may need to be a simple inductive element added to the contact resistance parameter in Equation 4.5 to capture these experimental artifacts.

4.3.4 Exploring the remaining solutions

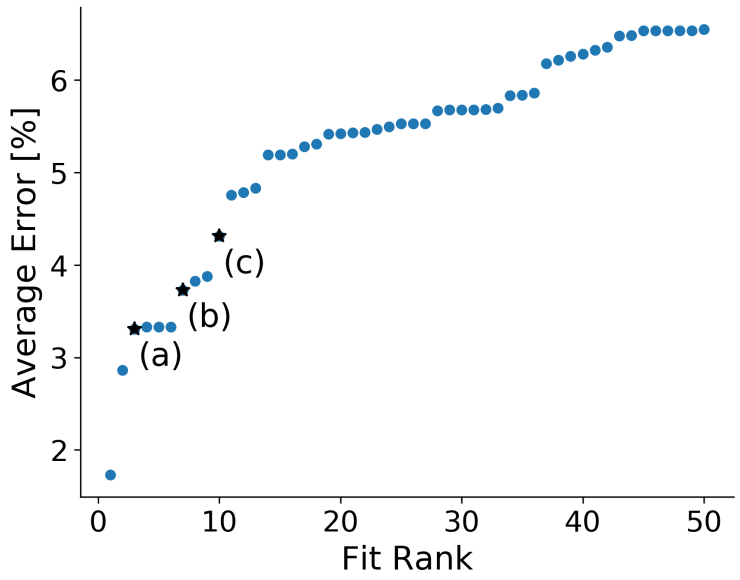

Figure 4.5: Plot of the top 50 ranked residual average errors between the experimental data set and the 38,800 simulated spectra. The letters denote (a) 3rd, (b) 7th, and (c) 10th ranked fitting errors corresponding to the spectra in Figure 4.6.

One of the benefits of the dataset-based approach taken in this work is that the nearby "nearly-matching" solutions can also be explored. Quickly visualizing the many spectra that are close to matching the experimental spectrum enables an experimentalist to begin piecing together a better understanding of the interacting physicochemical processes in the complex electrochemical system. Figure 4.5 shows the residual errors calculated using Equation 4.5 for the top 50 simulated spectra as a function of the spectra's rank. Multiple results with the same residual error occur when the only change in the input parameter set is a parameter that the linear impedance response is insensitive to (such as the charge transfer coefficients, α_a

and α_c, for example, where only their sum appears in the governing equations and boundary conditions). The steepness of the drop-off at low rankings (best fitting spectra) indicates that there is still potentially significant benefit to increasing the number of simulations in the dataset.

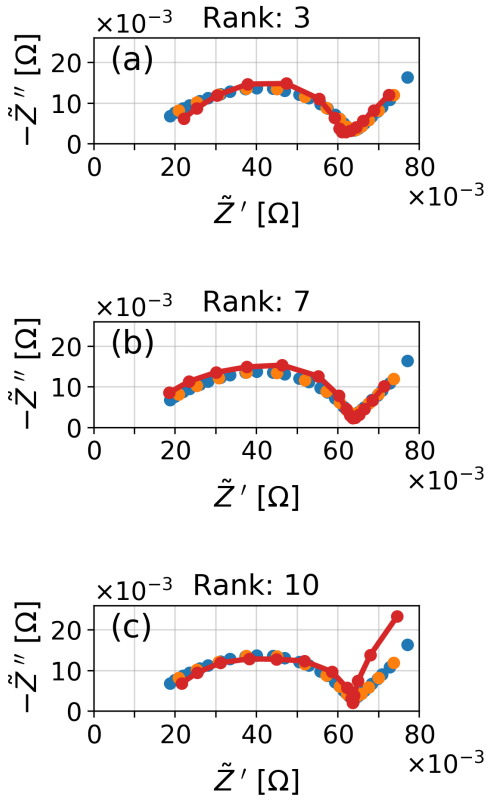

Figure 4.6: Nyquist plots of the (a) 3rd (m = 34560), (b) 7th (m = 4932), and (c) 10th (m = 32014) best matching spectra in the dataset of 38,000 simulated spectra.

To further demonstrate the different variations by which the simulated spectra fail to match the experimental data and how we can learn from them, the three spectra in Figure 4.6 show the starred 3rd, 7th, and 10th closest matching spectra in the dataset from Figure 4.5. For example, while Figure 4.6a (m = 34560) matches well in the low-frequency region, it fails at matching in the high-frequency regime. Conversely, the spectrum in Figure 4.6b (m = 4932) qualitatively matches, but has the timescales for kinetics shifted, while the spectra

shown in Figure 4.6c (m= 32014) has a qualitatively similar response in the high-frequency regime, but fails at low frequencies. Interactively exploring these nearby solutions is made easy in the ImpedanceAnalyzer via an "Explore P2D" modal where a user can mouse over the residual points and interactively see the corresponding spectrum and parameter values. Clicking on a residual point allows the comparison of multiple spectra and a download of the selected parameters is made available. The three parameter sets for the spectra in Figure 4.6 are presented in Table A4.3. We see that the qualitative improvement in the low-frequency response of the 3rd best spectra is likely due to the decreasing solid-phase diffusion coefficient in the negative electrode, $D_{s,neg}$, while further decreasing the diffusion coefficients many more orders of magnitude leads to the very poor match at low-frequencies for the 10th best spectrum. Additionally, decreasing the magnitudes of the open circuit potential derivatives leads to a smaller low-frequency tail between the 3rd and 7th best matching spectra. For the mid-frequency response, the lower negative exchange current density, $i_{0,neg}$, leads to similar time constants between electrodes resulting in a single, narrower arc for the 3rd ranked spectrum with respect to the best match. Decreased double-layer capacitances (increasing the characteristic frequency of both electrodes) broadens the mid-frequency response of the 7th ranked spectrum into a single, flatter kinetic arc, while increasing the positive electrode capacitance (lowering the characteristic frequency) and decreasing the negative electrode capacitance (increasing the characteristic frequency) removes the separation between the two electrode arcs in the 10th best fit.

The limiting electrode (i.e. the electrode which has the computed area of 1500mAh according to Eq 4.4) in each of the simulations shown in Figure 4.6 is the positive electrode except for the 10th best match. Interestingly, due to the symmetry of the P2D model, it is possible to switch the labels of pos and neg parameters and compute an identical spectrum. Additionally, the estimated superficial area for each of these nearly matching spectra vary more than 100 cm^2. Consequently, including additional information about the battery (including any known physicochemical or geometric ranges of parameters) will be useful for improving the matching process by filtering the dataset. Adding this feature is currently

under development.

4.3.5 Matched spectra as an initial guess for local optimization

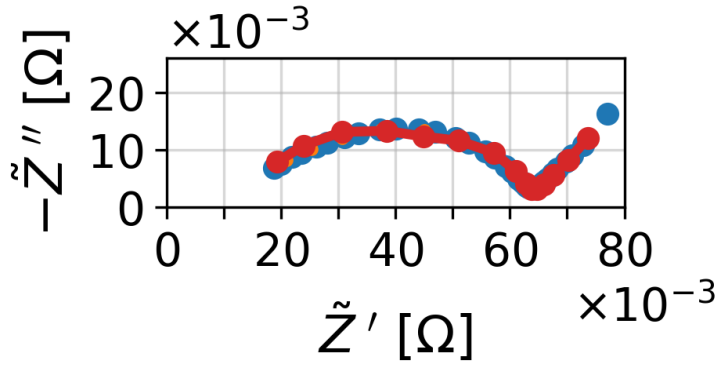

Figure 4.7: Nyquist plot comparing the experimental data with a two parameter locally optimized P2D simulated spectrum. A 20% increase in the double layer capacitance, $C_{dl,neg}$, and a 50% decrease in the solid diffusion coefficient, $D_{s,neg}$, resulted in a spectrum with a 1.25% error (33% lower than the best matching spectra in the 38,800 member dataset).

Sampling across a large range of physical parameters enables a fit such as that shown in Figure 4.4c, but, because we used parameters associated with a wide range of different battery chemistries, states-of-charge, etc., the 38,800 member EIS library is not a dense covering of the parameter space. Moreover, for any finite number of simulations, the global nature of the sampling process makes it likely that the resulting match is not a best-fit to the experimental spectrum. However, if there is low experimental noise, the selected spectrum makes a good starting point for further local optimization of the physics-based model. In the case of the spectrum shown in Figure 4.4c, the largest contributions to the remaining 1.73% error are in the low-frequency tail as well as the kinetic arc at high frequencies. Using conventional understanding of impedance spectra, the width of the high frequency arc can be attributed to the charge transfer resistance associated with the intercalation kinetics in both electrodes, while the time constants of the arcs (dictating their separation and shape) are also influenced by the double-layer capacitances. Thus, to change the shape of the kinetic arcs

without altering the total width, the double-layer capacitances can be varied. Additionally, because the time constants for kinetics and mass transport are separated by more than an order of magnitude, changes in either parameter group only affect the high-frequency arc and low-frequency tail, respectively. Figure 4.7 shows the consequence of a simple iterative reduction of residual error by varying the double-layer capacitances as well as the solid-phase diffusion coefficients and open circuit potential derivatives. For a 20% increase in double-layer capacitance, $C_{dl,neg}$, and a 50% decrease in the negative electrode solid diffusion coefficient, $D_{s,neg}$, the residual error decreased to 1.25%. Directly incorporating sophisticated local optimization in the vicinity of several highly ranked solutions found by global sampling is a functionality currently being explored for the ImpedanceAnalyzer.

4.4 Implications and concluding remarks

The physics-based nature of the P2D and other electrochemical models enables a wide set of physically relevant and interpretable impedance responses to be captured by simply varying the combinations of physicochemical parameter inputs. With a physics-based approach, it is transparent what phenomena are included in the model and what assumptions underpin the model. In contrast, equivalent circuits are reduced order models of (normally) complex physical and chemical processes, sometimes leading to ambiguous or incorrect interpretation of results.[59] While it is normally possible to fit some form of an equivalent circuit to an experimental spectrum, linking the fit to the underlying phenomena for anything but the simplest electrochemical systems remains a fraught exercise.

In the work described here, the P2D battery model was used to demonstrate the dataset-based approach for parameter estimation. As noted in the introduction, the high citation rate of the P2D model makes it the de facto "standard" continuum model for capturing the dynamics of the lithium-ion system. Moreover, significant research efforts have focused on adding additional physics to the system making it a good candidate for demonstration. That said, the open-source, dataset-based approach described here enables an opportunity to start statistically comparing electrochemical models as different physical processes are in-

cluded or removed. Combining the sampling scheme with methods for performing a global, variance-based sensitivity analysis[125] of the simulated dataset can provide information on the parameters most responsible for variations in the impedance spectra at a given frequency. It has been shown that parameter identifiability is an important consideration in fitting electrochemical models to experimental data.[126] Comparing the parameter sensitivity as more complex physical interactions are sequentially added to models can provide statistical insight into the tradeoff between a more descriptive physical representation of the system and potentially worse parameter identifiability as additional parameters are added. Additionally, comparing an experimental spectrum to the nearest matching spectra within a single dataset can enable a bootstrap approach to establishing confidence intervals in the estimated parameters. Several additional benefits arise from the dataset-based approach described here. The computational time is spent upfront during the generation of the dataset, significantly reducing the time an experimentalist waits to find a best matching spectrum. The time needed to identify the best matching fit to experimental data is unchanged by the complexity of the model. Only the size of the library affects the estimation time. Of course, a more complex model will take longer to compute the library of spectra; however, separating the model complexity from the time required to estimate the parameters becomes increasingly important as the quest for deeper insight into complex electrochemical systems grows. Furthermore, the open-source nature of the platform enables the inclusion of additional electrochemical data such as higher order harmonic responses,[75] spectra at multiple states (depths-of-discharge or temperatures), as well as (dis) charge curves or cyclic voltammetry.

The power of open-source software like this lies in the opportunity for subsequent contributor to add features, additional simulated or experimental data sets, etc., thereby evolving the tool to a more useful form. To that end, the ImpedanceAnalyzer is simply the start of a platform to which others are encouraged to contribute. The code is openly available on GitHub and users of the software can cite the version released at the time of this manuscript.[113] Other open software and open data products being actively built by the electrochemical data science community are also available for those interested in collaborative

development.[127] Data and the analysis code for this paper can be found online.[114]

Appendix

Table A4.1: Physicochemical and geometric parameter ranges for simulated dataset

Physicochemical Parameters

Name	**Units**	**Lower Limit**	**Upper Limit**
$Brugg$	—	4	4
$C_{dl,neg}$	$\mu F/cm^2$	1	100
$C_{dl,pos}$	$\mu F/cm^2$	1	100
c_0	mol/m^3	100	5000
D	m^2/s	10^{-11}	10^{-9}
$D_{s,neg}$	m^2/s	10^{-19}	10^{-10}
$D_{s,pos}$	m^2/s	10^{-17}	10^{-10}
$\frac{\partial U_{neg}}{\partial c^s}$	$V \cdot cm^3/mol$	-100	0
$\frac{\partial U_{pos}}{\partial c^s}$	$V \cdot cm^3/mol$	-100	0
$i_{0,neg}$	A/m^2	1	20
$i_{0,pos}$	A/m^2	1	200
t_+^0	—	0.2	0.99
$\alpha_{a,neg}$	—	0.2	0.8
$\alpha_{a,pos}$	—	0.2	0.8
κ	S/m	0.1	8
σ_{neg}	S/m	30	4000
σ_{pos}	S/m	4	30

Geometric Parameters

Name	**Units**	**Fresh Cell**	**Aged Cell**
l_{neg}	μm	15	1200
l_{sep}	μm	8	40
l_{pos}	μm	15	1200
$R_{p,neg}$	μm	.25	20
$R_{p,pos}$	μm	1	15
$\epsilon_{f,neg}$	—	0.0	0.12
$\epsilon_{f,pos}$	—	0.0	0.12
ϵ_{neg}	—	0.2	0.5
ϵ_{sep}	—	0.35	0.8
ϵ_{pos}	—	0.2	0.5

Table A4.2: Physicochemical and geometric parameters for best matching spectra

Physicochemical Parameters

Name	**Value [Units]**
$C_{dl,neg}$	79.8 $[\mu F/cm^2]$
$C_{dl,pos}$	86.5 $[\mu F/cm^2]$
c_0	1485.3 $[mol/m^3]$
D	7.68 $\times 10^{-10}$ $[m^2/s]$
$D_{s,neg}$	9.09 $\times 10^{-12}$ $[m^2/s]$
$D_{s,pos}$	4.34 $\times 10^{-16}$ $[m^2/s]$
$\frac{\partial U_{neg}}{\partial c^s}$	-40.5 $[V \cdot cm^3/mol]$
$\frac{\partial U_{pos}}{\partial c^s}$	-9.60 $[V \cdot cm^3/mol]$
$i_{0,neg}$	19.42 $[A/m^2]$
$i_{0,pos}$	1.56 $[A/m^2]$
t_+^0	.45 [—]
$\alpha_{a,neg}$	.58 [—]
$\alpha_{a,pos}$	.41 [—]
κ	1.42 $[S/m$
σ_{neg}	1986 $[S/m]$
σ_{pos}	19.6 $[S/m]$

Fit Parameters

Name	**Value [Units]**
A_{sup}	300.3 $[cm^2]$
$R_{contact}$	4.2 $[m\Omega]$

Geometric Parameters

Name	**Value [Units]**
l_{neg}	319.9 $[\mu m]$
l_{sep}	35.9 $[\mu m]$
l_{pos}	159.1 $[\mu m]$
$R_{p,neg}$	19.3 $[\mu m]$
$R_{p,pos}$	1.49 $[\mu m]$
$\epsilon_{f,neg}$	0.062 [—]
$\epsilon_{f,pos}$	0.075 [—]
ϵ_{neg}	0.366 [—]
ϵ_{sep}	0.680 [—]
ϵ_{pos}	0.354 [—]

Table A4.3: Parameters for nearly matching spectra shown in Figure 4.6

Fit Parameters

Name	Units	Rank: 3 Run: 34560	Rank: 7 Run: 4932	Rank: 10 Run: 32014
A_{sup}	cm^2	313.9	268.7	218.4
$R_{contact}$	$m\Omega$	10.1	4.9	8.0

Physicochemical Parameters

Name	Units	Rank: 3 Run: 34560	Rank: 7 Run: 4932	Rank: 10 Run: 32014
$C_{dl,neg}$	$\mu F/cm^2$	31.0	57.2	32.3
$C_{dl,pos}$	$\mu F/cm^2$	30.7	47.3	97.3
c_0	mol/m^3	4635	4921	986.5
D	m^2/s	8.547×10^{-10}	7.588×10^{-10}	1.943×10^{-11}
$D_{s,neg}$	m^2/s	2.465×10^{-13}	9.989×10^{-18}	2.793×10^{-19}
$D_{s,pos}$	m^2/s	3.214×10^{-15}	8.104×10^{-15}	2.205×10^{-17}
$\frac{\partial U_{neg}}{\partial c^s}$	$V \cdot cm^3/mol$	-0.1593	-0.1937	-2.976
$\frac{\partial U_{pos}}{\partial c^s}$	$V \cdot cm^3/mol$	-43.03	26.77	-0.02543
$i_{0,neg}$	A/m^2	2.619	19.68	6.163
$i_{0,pos}$	A/m^2	1.616	1.934	1.937
t_+^0	—	0.984	0.483	0.942
$\alpha_{a,neg}$	—	0.524	0.528	0.348
$\alpha_{a,pos}$	—	0.632	0.269	0.264
κ	S/m	5.726	7.024	6.544
σ_{neg}	S/m	356.1	173.7	2484
σ_{pos}	S/m	10.63	5.638	22.71

Physicochemical Parameters

Name	Units	Rank: 3 Run: 34560	Rank: 7 Run: 4932	Rank: 10 Run: 32014
l_{neg}	μm	422.6	262.1	286.7
l_{sep}	μm	17.85	8.422	28.35
l_{pos}	μm	150.1	142.9	336.4
$R_{p,neg}$	μm	2.447	18.45	6.418
$R_{p,pos}$	μm	6.117	6.23	2.384
$\epsilon_{f,neg}$	—	0.094	0.041	0.069
$\epsilon_{f,pos}$	—	0.011	0.028	0.033
ϵ_{neg}	—	0.234	0.331	0.332
ϵ_{sep}	—	0.479	0.757	0.494
ϵ_{pos}	—	0.411	0.262	0.271

Chapter 5

ADDITIONAL PROJECTS

5.1 Initial datasets and exploration of parameter sensitivity

5.1.1 Introduction

Physics-based models have often been used to interpret the whole cell response of lithium-ion batteries.[122] In particular, the pseudo-two-dimensional (P2D) battery model has been used to understand,[89] design,[90,91] and control[92] lithium-ion batteries for many decades. Many results have demonstrated that the equations representing coupled mass transport, thermodynamic, and reaction processes in the P2D model are flexible enough to capture a significant amount of the variation seen in experimental data. A handful of examples using the frequency domain solutions have also demonstrated that experimental measurements of the linear and nonlinear harmonic response of a battery can also be represented by the P2D model.[59,98] Despite the widespread use of these models in interpreting battery performance, accurately capturing the internal state of these systems for use in next-generation battery management and control also requires a robust understanding of parameter identifiability and model validation.[126] In particular, to be used in long-term aging predictions the model and parameters must not only be required to reproduce the cell voltage response reliably, but also accurately predict the internal states of the battery.

Impedance-based measurements can provide additional information to be used in estimating accurate parameters;[59,75] however, understanding the increase in information content and parameter identifiability has only begun to be explored.[126] In one example, Bizeray et al. use the single-particle model to demonstrate that the linear EIS impedance model is only uniquely defined if the open circuit potential is non-zero; that is, the local thermodynamics of the system can dictate the identifiability of mass transport parameters in the low-frequency

impedance response.[126] To begin further exploring the parameter sensitivity of the linear EIS and second harmonic NLEIS response of our previously described P2D model,[75] we describe the results of an initial sensitivity analysis. The sensitivity indices for the linear EIS and second harmonic NLEIS response are a first step in determining the experimental conditions under which particular parameters can be reliably measured and .

5.1.2 Global sensitivity analyses

For a deterministic model, $y = f(x_1, x_2, \ldots, x_k)$ where f is a complex relationship between input parameters, $\mathbf{x} = x_1, x_2, \ldots, x_k$, and model output, y, a sensitivity analysis can provide insight into how changes in the parameters influence the output.[125] Sensitivity analyses can be either local (based on the derivatives of f evaluated around a base case $\mathbf{x} = \mathbf{x}_0$) or global (parameters are allowed to vary across a significant range of interest). Local sensitivity is typically straightforward and computationally efficient to implement, however, the utility is limited to either linear systems or in regimes very close to a known set of base parameters. Global sensitivity analyses, on the other hand, explore the full parameter space and provide a more complete exploration of parameter interactions and model nonlinearity, albeit at the cost of a somewhat more challenging implementation.[125]

A good method for approaching a global sensitivity analysis is to start by treating our input parameters as a random variable, $\mathbf{X}$, with a given distribution, such that the model output $Y = f(\mathbf{X})$ is also a random variable with an unknown distribution. This treatment, known as probabilistic sensitivity analysis,[128] is useful because it allows us to think about how each parameter (or interactions between parameters) affects the output variance (or uncertainty) of the model. Those parameters which affect the output variance significantly are "sensitive" whereas parameters which contribute little to the output variance are "insensitive".

To quantify the relative importance of each parameter, X_i, we can look at how much the expected value of the output given a known value of the parameter $X_i = X_*$ varies across all values of X_* in the parameter range,

$$V_{X_i}\left(E_{\mathbf{X}_{\sim i}}\left(Y|X_i\right)\right) \tag{5.1}$$

where V is the variance, E is the expected value, and $\mathbf{X}_{\sim i}$ includes all factors except for X_i. Normalizing the variance in Equation 5.1 by the total variance in the model output, $V(Y)$, gives us the first-order sensitivity index,[125]

$$S_i = \frac{V_{X_i}\left(E_{\mathbf{X}_{\sim i}}\left(Y|X_i\right)\right)}{V(Y)} \tag{5.2}$$

where S_i is a number always between 0 and 1 and a high value indicates that a parameter is important.

It should be noted that, for an additive model (one in which there are no interactions amongst parameters), the first-order sensitivity indices, S_i, sum to 1. However, when there are more complex interactions between parameters,[125]

$$\sum_i S_i + \sum_i \sum_{j>i} S_{ij} + \sum_i \sum_{j>i} \sum_{l>j} S_{ijl} + \cdots + S_{123\ldots k} = 1 \tag{5.3}$$

where S_{ij} and S_{ijl} are the sensitivity indices associated with second- and third-order interactions between parameters. That is, the total sensitivity can be partitioned into the first- and higher-order contributions from individual and interactions between parameters. While calculating all of the individual higher-order terms is theoretically interesting, we are likely more concerned with the computationally tractable job of estimating the total effect, S_{Ti}, of a parameter, *i.e.* the sum of all of the sensitivity indices which include the parameter X_i. For example, for a generic three-factor model,[125]

$$S_{T1} = S_1 + S_{12} + S_{13} + S_{123}. \tag{5.4}$$

Calculating this total effect is made easier by the fact that we know from Equation 5.3 that all of the indices sum to 1. By subtracting out only the indices which *do not* contain, the

parameter X_i, we arrive at the total effect sensitivity index,[125]

$$S_{Ti} = 1 - \frac{V_{\mathbf{X}_{\sim i}}\left(E_{\mathbf{X}_i}\left(Y|\mathbf{X}_{\sim i}\right)\right)}{V(Y)}. \tag{5.5}$$

While the statistical definitions of S_i and S_{Ti} (Equations 5.2 and 5.5) are useful in computing a measure of sensitivity, a physical representation of these measures can be easier to connect to the analysis of a linear EIS or second-harmonic NLEIS spectrum. Specifically, the first-order sensitivity indices, S_i, can be thought of as the amount of variance that is removed from the model output if we could precisely measure X_i, while the total-effect indices, S_{Ti}, represent the amount of variance we would expect to remain if all factors, except X_i could be fixed. The relative difference in the two measures indicates the level to which the parameter interacts with other parameters.

5.1.3 Selecting physical parameter ranges for lithium-ion batteries

Unlike a local sensitivity analysis based on derivatives around a set of base parameters, a global sensitivity analysis requires that the parameters be sampled across some "global" parameter space. Determining the parameter space that captures the realistic behavior of the linear EIS and nonlinear second-harmonic NLEIS response across the full variation of lithium-ion battery chemistries and geometries presents a trade-off between a huge parameter space requiring an exceedingly large dataset (and lots of computational time) to sufficiently sample the space vs. a narrower parameter range which may only capture a subset of the battery behavior. Additionally, the frequency range and spacing, an independent variable in the model, also affects the computational time required to generate a dataset. As a result, several datasets were created as a part of this thesis in response to this trade-off.

In addition to the dataset described in Chapter 4 used for matching experimental spectra as a part of the ImpedanceAnalyzer, several other datasets of impedance spectra were created. In particular, a dataset containing 6000 spectra over 41 frequencies and a narrower parameter range (see Table A5.1) was generated to explore the full frequency dependence and better

capture timescales seen in experimental data.

Once the parameter range was determined, the SALib[121] Python package was used to generate a Sobol' sampling sequence[120] in order to efficiently explore the high dimensional parameter space. To generate the final dataset, a COMSOL model was solved for each of the sampled combinations of parameters, frequencies, and harmonics using LiveLink for MATLAB and the resulting linear EIS and second harmonic NLEIS spectra were saved. The sensitivity index and bootstrapped confidence interval for each parameter and at each frequency was estimated using the `SALib.sobol.analyze` method.[121] It should be noted that to calculate the sensitivity index at a given frequency the complex impedance response, $Z_i = Z_i' + jZ_i''$, must be reduced to a single output value. The natural choices for this reduction are to use the real (Z_i') or imaginary (Z_i'') components or the magnitude ($|Z_i|$) or phase angle (ϕ_{Z_i}). Here, we show the results for the phase angle (ϕ_{Z_1} and ϕ_{Z_2}) since it is the most sensitive.

Geometric parameters The physical properties of a battery's construction, such as electrode and separator thickness, porosity, tortuosity, and particle size, play a critical role in determining the performance of the overall system.[91,129] The widely-varying applications and form factors of today's lithium-ion batteries result in a large range in the geometric parameters.[130,131] In particular, a battery meant to provide relatively low power for a long time — an "energy" cell — typically has large particle sizes, low porosity, and thick electrodes to maximize the amount of active electrode material, while a battery used for high-power bursts — a "power" cell — would typically have thinner electrodes, smaller particles, and higher porosity to facilitate transport.[132]

In the positive electrode materials, the variance in parameters across materials is particularly significant with $LiFePO_4$ (LFP) particles typically requiring small particle sizes to overcome low bulk conductivity and solid-state diffusion limitations.[133] For other common positive electrode materials, $LiCoO_2$ (LCO) and $LiNi_{1/3}Mn_{1/3}Co_{1/3}O_2$ (NMC) for example, the high surface area and electrochemically favorable breakdown of electrolyte at high po-

tentials means that micron-sized particles are more favored.[130] In commercial electrodes, the LCO and NMC particle sizes tend to be in the 2–12 μm range while LFP is less than 1 μm particles.[130,134,135] Anode materials are typically carbon based with more tightly constrained particle sizes.

Research into thick electrodes for increased energy density pushes the upper limit on electrode thickness,[136,137] while high-power cells can be significantly thinner.[131] The thickness of the separator effectively determines the internal resistance of the battery and the standardized, commercial separators used in today's cells tend to have a narrower range of thicknesses and porosities.[138,139] Finally, the porosity and tortuosity of the electrode affects battery performance by altering the effective transport, kinetic, and conductivity parameters.[140]

Physicochemical parameters Along with the physical construction of the battery, the physicochemical parameters dictate the timescales and relative importance of different kinetic, transport, and thermodynamic processes governing battery performance. In particular, the exchange current density, i_0, of a material dictates the overpotential required to drive the intercalation reaction, while the solid- and solution-phase conductivities determine the magnitude of the voltage drop across the cell. Moreover, the ratio of the exchange current density to the ohmic resistance determines the characteristic penetration depth of the reaction zone.[122]

The exchange current density can vary several orders of magnitude across electrode materials as well as the battery state-of-charge (i_0 is typically concentration dependent).[141,142] Even more variation is seen in the solid-phase diffusion coefficients which can be 10 orders of magnitude smaller for LFP particles than the carbon anode or other positive electrode materials.[10,143,144] The double-layer capacitance range is set by the typical time constants seen in experimental EIS spectra and the local open circuit voltage gradient values for each electrode are constrained by realistic bounds found in the literature for multiple chemistries.

5.1.4 Initial results and discussion

Total effect sensitivity indices

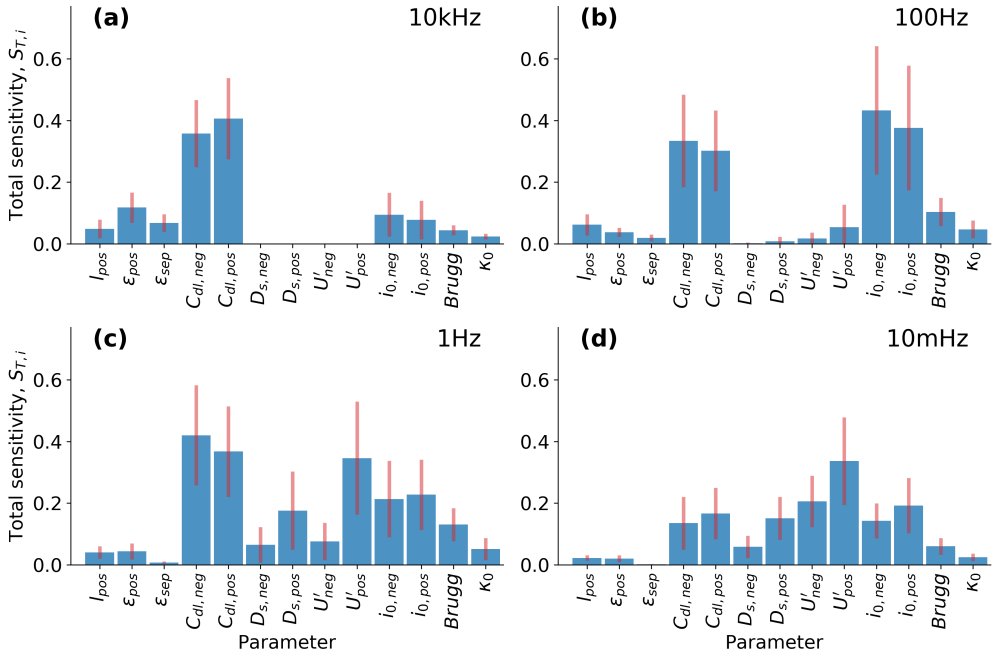

Figure 5.1: Significant total sensitivity indices, $S_{T,i}$, for the phase of the simulated EIS response, Z_1. Only parameters with $S_{T,i} > 0.1$ are shown.

Figure 5.1 shows the total-effect sensitivity indices, $S_{T,i}$, for the phase of the simulated linear EIS response at four different frequencies. The different sensitivities at each of the four frequencies (10 kHz, 100 Hz, 1 Hz, and 10 mHz) demonstrate the differing timescales of the interfacial, transport, and thermodynamic physicochemical processes governing the response. For the linear EIS response, the typical timescales of EIS for a lithium-ion battery are captured by these total-effect sensitivity measures. For example, in Figure 5.1a, the thickness, l, porosity, ϵ, and conductivity, κ_0, which contribute to the ohmic resistance of the cell (Equation 4.2) are sensitive at high frequencies. Interestingly, the double-layer capacitance, $C_{dl,i}$, shows a relatively strong sensitivity across the entire spectrum in this dataset. $C_{dl,i}$ effectively sets the timescale of the interfacial response and its importance

across all of the frequencies is a reflection of the wide parameter range chosen. As the frequency is lowered the exchange current densities, $i_{0,i}$, are more sensitive in the mid-frequency, kinetics regime (Figure 5.1b), and diffusion coefficients, D and $D_{s,i}$, and open-circuit potential derivatives, U_i' are sensitive at the low-frequencies (Figure 5.1c).

The results shown in Figure 5.1 also demonstrate the dependence of the computed indices on the parameter ranges that are sampled over. For example, although the high frequency ohmic response of the battery clearly depends on the porosities and thicknesses of both electrodes and the separator through Equation 4.2, the model is less sensitive to l_{neg} and l_{sep} than l_{pos} due to the range of positive electrode conductivities (σ_{neg} are always relatively high) and separator thicknesses (l_{sep} has a much smaller range than l_i). These ranges effectively ensure that the largest variations in the ohmic response are from the widely varying positive electrode parameters; however, if the ranges changed (*e.g.* either the positive electrode conductivity lower bound was increased or the separator thickness range was increased) the resulting indices would change. This dependence on parameter ranges can be thought of in the same way as a Bayesian prior and allows the reality of today's battery materials to be embedded into the analysis. Unlike specifying an actual prior distribution, however, the Sobol' method assumes a uniform distribution over the parameter space, meaning that including a very large parameter range (say to try and cover both research lab and commercially available batteries across many different chemistries) can tend to highlight the extreme combinations of parameters more than they would likely occur in the real world. Consequently, generating a dataset where parameters are sampled from a nonuniform distribution may more realistically reflect the real parameter space. In particular, methods for calculating sensitivity which do not rely on a predefined sampling scheme, such as the Delta method,[145] have briefly been explored and future work should consider these alternative sampling schemes and sensitivity methods.

For the second harmonic sensitivities shown in Figure 5.2, the general trend of parameter sensitivity in the different frequency regimes is similar to the linear response, however, the magnitude of the sensitivity measures is generally increased. A higher total-effect sensitivity

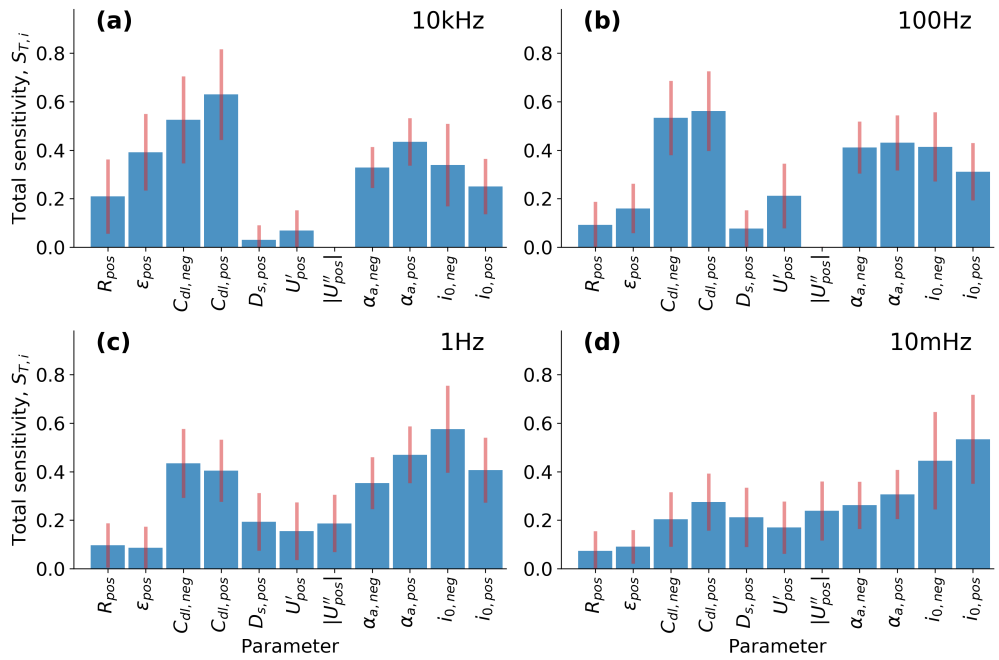

Figure 5.2: Significant total sensitivity indices, $S_{T,i}$, for the phase of the simulated second harmonic response, Z_2. Only parameters with $S_{T,i} > 0.2$ are shown.

index could arise either from a parameter which is now uniquely sensitive or from increased interactions with the other parameters. Several significant differences in the second harmonic parameter sensitivity indices reflect new information about the system that can be measured. Specifically, Figure 5.2 shows that the transfer coefficients, $\alpha_{a,i}$, which govern the symmetry of the charge transfer reaction are sensitive across much of the second-harmonic frequency range, while being completely insensitive in the linear response. Similarly, both the magnitude and sign of the second derivatives in open circuit poential, $|U_i''|$ and $\text{sgn}(U_i)$ are only sensitive in the second harmonic response. These increases in individual parameter sensitivities, along with the increased average total sensitivity (attributable to the additional parameter mixing due to nonlinear interactions), demonstrates statistically the breaking of degeneracy through the second harmonic NLEIS spectra.

5.1.5 Appendix

Table A5.1: Parameter ranges for global sensitivity analysis

Physicochemical Parameters

Name	Units	Lower Limit	Upper Limit
$Brugg$	—	1	5
$C_{dl,neg}$	$\mu F/cm^2$	1	10^5
$C_{dl,pos}$	$\mu F/cm^2$	1	10^5
c_0	mol/m^3	100	5000
D	m^2/s	5×10^{-11}	1×10^{-9}
$D_{s,neg}$	m^2/s	1×10^{-16}	1×10^{-10}
$D_{s,pos}$	m^2/s	1×10^{-22}	1×10^{-11}
$\frac{\partial U_{neg}}{\partial c^s}$	$V \cdot cm^3/mol$	-1000	0
$\frac{\partial U_{pos}}{\partial c^s}$	$V \cdot cm^3/mol$	-1000	0
$\frac{\partial^2 U_{neg}}{\partial {c^s}^2}$	$V \cdot cm^6/mol^2$	-10^5	10^5
$\frac{\partial^2 U_{pos}}{\partial {c^s}^2}$	$V \cdot cm^6/mol^2$	-10^5	10^5
$i_{0,neg}$	A/m^2	0.05	320
$i_{0,pos}$	A/m^2	0.05	75
t_+^0	—	0.2	0.95
$\alpha_{a,neg}$	—	0.2	0.8
$\alpha_{a,pos}$	—	0.2	0.8
κ	S/m	0.01	2
σ_{neg}	S/m	50	2000
σ_{pos}	S/m	0.1	20

Geometric Parameters

Name	Units	Lower Limit	Upper Limit
l_{neg}	μm	20	350
l_{sep}	μm	15	60
l_{pos}	μm	20	350
$R_{p,neg}$	μm	0.1	20
$R_{p,pos}$	μm	0.015	20
$\epsilon_{f,neg}$	—	0.0	0.12
$\epsilon_{f,pos}$	—	0.0	0.12
ϵ_{neg}	—	0.2	0.7
ϵ_{sep}	—	0.35	0.8
ϵ_{pos}	—	0.2	0.7

Constants

Name	Units	Value
T	K	298.15
F	C/mol	96487
R	$J/mol \cdot K$	8.314

5.2 Equivalent circuits for linear EIS and second harmonic NLEIS spectra

5.2.1 Introduction

Electrochemical impedance spectroscopy (EIS) is a widely used technique for the characterization of complex electrochemical systems due to its noninvasive and sensitive probing of the underlying physicochemical processes.[1–3] Typically, both quantitative interpretation of an experimental EIS spectrum involve the fitting of an equivalent circuit model to extract parameters that capture the system response. While EIS has been a powerful tool for characterizing many systems,[4–16] the use of small amplitude perturbations required by EIS limits the technique to probing only a linearized view of the full nonlinear physics that govern the system. A moderate-amplitude extension to EIS, called nonlinear EIS, has been used to provide a more sensitive signature for many electrochemical systems.[19] To date, however, interpreting NLEIS spectra for lithium-ion batteries, has relied on complex, full physics mathematical models which are not always easily implemented.[75]

Here we extend the widely used Randles equivalent circuit model[118] to include a second harmonic NLEIS response. Contributions from the nonlinear kinetics and thermodynamics can be captured by additional circuit elements that are fit to a second harmonic NLEIS spectrum in conjunction with the standard linear EIS Randles circuit. In particular, the second-harmonic analog to a charge-transfer resistance depends not only on the exchange current density (like the normal linear charge transfer resistance), but also on the symmetry of the reaction. Using simulations of a previously developed full physics linear EIS and NLEIS model, we show the applicability of equivalent circuits to the impedance of a porous electrode and describe the relationship between EIS and NLEIS spectra. Experimentally measured linear EIS and second harmonic NLEIS spectra of a Samsung 1.5 Ah LiNMC|C cell show variations in charge transfer symmetry as the state-of-charge (SoC) is varied. Ultimately, the equivalent circuits described in this work can be easily implemented via an open-source Python package and made available to anyone for easy-to-use parameter estimation from linear EIS and second harmonic NLEIS spectra.

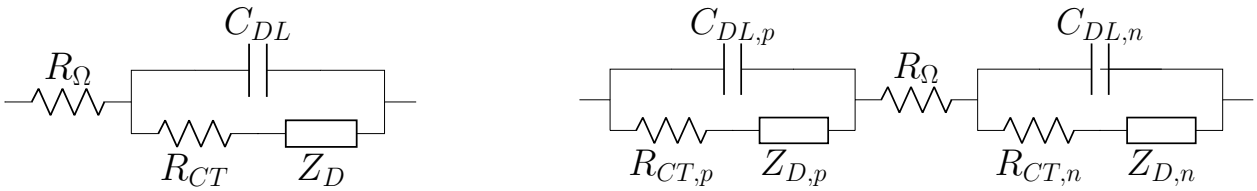

(a) Single-electrode circuit **(b) Two-electrode circuit**

Figure 5.3: Randles equivalent circuit models for linear EIS

5.2.2 Equivalent circuit models

Linear EIS Randles model

The Randles circuit is a commonly used equivalent circuit for many electrochemical systems.[118] Shown in Figure 5.3a, the Randles equivalent circuit captures the ohmic, interfacial, and mass transport phenomena in an electrochemical system via a network of circuit elements. In particular, the simple circuit is comprised of an ohmic resistance, R_Ω, in series with a parallel combination of charge transfer resistance, R_{CT}, and double-layer capacitance, C_{DL}, representing the faradaic and non-faradaic interfacial processes, respectively. Typically, a diffusional impedance, Z_D, is also included.

The Randles circuit elements can be defined in terms of physicochemical parameters. The ohmic resistance, R_Ω, is given by the sum of the ohmic resistances in each region of the cell,

$$R_\Omega = \left[\frac{l_{pos}}{\sigma_{eff,pos} + \kappa_{eff,pos}}\right] + \left[\frac{l_{sep}}{\kappa_{eff,sep}}\right] + \left[\frac{l_{neg}}{\sigma_{eff,neg} + \kappa_{eff,neg}}\right] \tag{5.6}$$

where l_i is the thickness of the region, and $\sigma_{eff,i}$ and $\kappa_{eff,i}$ are the effective solid- and solution-phase conductivities, respectively.

The charge transfer resistance, R_{CT}, can be easily calculated using Butler-Volmer kinetics,

$$R_{CT} = \frac{RT}{i_0(\alpha_a + \alpha_c)F} \tag{5.7}$$

where i_0 is the exchange current density, R is the gas constant, T is the temperature, F

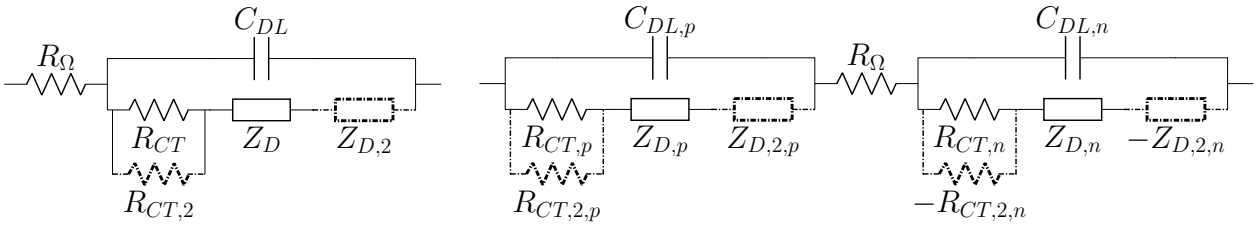

(a) Single-electrode circuit **(b) Two-electrode circuit**

Figure 5.4: The additional elements ($R_{CT,2}$ and $Z_{D,2}$) for a nonlinear EIS Randles equivalent circuit model (a) arise from nonlinearities in the kinetic and mass transport. The dotted elements indicate elements that respond at the 2× the perturbation frequency, ω_1, and are fit to the second harmonic NLEIS response.

is Faraday's constant, and α_a and α_c are the anodic and cathodic transfer coefficients, respectively. The parallel combination of R and C results in a characteristic time constant, $\tau_{int} = R_{CT}C_{DL}$, for the interfacial response.

The impedance response of solid-phase lithium transport in spherical particles can be described by,[9,146]

$$Z_D = \left(-\frac{\partial U}{\partial c_s}\bigg|_{c_s^0} \frac{R_p}{F D_s} \right) \left(\frac{\tanh\sqrt{j\tilde{\omega}}}{\sqrt{j\tilde{\omega}} - \tanh\sqrt{j\tilde{\omega}}} \right) \tag{5.8}$$

where $\frac{\partial U}{\partial c_s}\Big|_{c_s^0}$ is the derivative of the open circuit potential with respect to the solid phase concentration, $\tilde{\omega}$ is a characteristic diffusion frequency, $\tilde{\omega} = \frac{\omega {R_p}^2}{D_s}$, R_p is the particle radius, D_s is the solid-phase diffusivity, ω is the perturbation frequency, and j is the imaginary unit.

The linear impedance response is additive,[3] such that for a full battery cell with two electrodes, the two half cell and separator impedances can be added in series to create a two electrode Randles circuit (Figure 5.3b).

Second harmonic NLEIS model

We have previously described the process for deriving the full dynamics of the second harmonic impedance response for a lithium-ion battery using the pseudo-two-dimensional (P2D) battery model;[75] however, here we derive the local nonlinear kinetic response of the Butler-

Volmer equation,

$$j = i_0 \left[\exp\left(\alpha_a f\eta\right) - \exp\left(-\alpha_c f\eta\right)\right] \tag{5.9}$$

where $f = \frac{F}{RT}$. To derive the second harmonic charge transfer "resistance," we take the first two terms of the Taylor series expansion around $\eta = 0$,

$$\frac{j}{i_0} \approx \left(\alpha_a + \alpha_c\right) f\eta + \frac{1}{2}\left(\alpha_a^2 - \alpha_c^2\right) f^2\eta^2. \tag{5.10}$$

We can then solve for η using quadratic equation (only positive branch of $\pm$ is physical),

$$\eta \approx -\frac{(\alpha_a + \alpha_c)}{(\alpha_a^2 - \alpha_c^2)f} + \frac{(\alpha_a + \alpha_c)}{(\alpha_a^2 - \alpha_c^2)f}\sqrt{1 + \frac{2j(\alpha_a^2 - \alpha_c^2)}{i_0(\alpha_a + \alpha_c)^2}}. \tag{5.11}$$

Expanding square root via Taylor series expansion around $j = 0$ and perturbing the current, $j = \Delta j \cos\omega t$,

$$\eta \approx \left(\frac{1}{i_0(\alpha_a + \alpha_c)f}\right)\Delta j \cos\omega t - \left(\frac{(\alpha_a^2 - \alpha_c^2)}{4i_0^2(\alpha_a + \alpha_c)^3 f}\right)\Delta j^2\left[1 + \cos\omega t\right] \tag{5.12}$$

results in,

$$R_{CT,2} = \frac{-(\alpha_a^2 - \alpha_c^2)}{4i_0^2(\alpha_a + \alpha_c)^3 f}$$

While $R_{CT,2}$ is clearly not a resistance (it has units of $\frac{\Omega}{A} - m^4$), it serves an analogous purpose to the charge transfer resistance in that it relates the nonlinearly generated second harmonic voltage response to the input perturbation. Consequently, when the reaction is symmetric ($\alpha_a = \alpha_c = 0.5$) no second harmonic voltage response will be generated.

The second harmonic diffusional impedance, $Z_{D,2}$, for spherical particles is similar to the form of Equation 5.8 since Fickian diffusion is a linear equation. However, instead of the response being generated by the first derivative of the open circuit potential, $\left.\frac{\partial^2 U}{\partial {c_s}^2}\right|_{c_s^0}$, multiplied by the oscillating solid phase concentration, the second harmonic is driven by the square of the oscillating concentration times the second derivative of the open circuit

potential with respect to the solid phase concentration, $\left.\frac{\partial^2 U}{\partial {c_s}^2}\right|_{c_s^0}$,

$$Z_{D,2} = \left(-\left.\frac{\partial^2 U}{\partial {c_s}^2}\right|_{c_s^0} \frac{{R_p}^2}{F^2 {D_s}^2}\right)\left(\frac{\tanh\sqrt{j\tilde{\omega}}}{\sqrt{j\tilde{\omega}} - \tanh\sqrt{j\tilde{\omega}}}\right)^2. \tag{5.13}$$

Unlike $\left.\frac{\partial^2 U}{\partial {c_s}^2}\right|_{c_s^0}$ which is typically less than or equal to zero, $\left.\frac{\partial^2 U}{\partial {c_s}^2}\right|_{c_s^0}$ can be both positive, negative, or zero and typically varies significantly across the potential window of an electrode. This increased variability leads to second harmonic impedance spectra which can vary significantly at low frequencies.

The driving force for both the first and second harmonic charge transfer response is the voltage perturbation across the interface indicating the impedances of the two elements should be added in parallel (*i.e.* the admittances are in series). Thus, in the second harmonic Randles circuit shown in Figure 5.4 the impedance elements (Z_{CT} and $Z_{CT,2}$) are in parallel. Conversely, the current passing through the diffusional impedances is the common driving force for the diffusional elements, and thus the diffusional impedance elements (Z_D and $Z_{D,2}$) are in series in Figure 5.4.

In order to calculate the overall second harmonic impedance response, the local kinetic and diffusional impedances must be referenced only to the driving current that is passing through the interfacial branch of the equivalent circuit,

$$Z_2 = (Z_{CT,2} + Z_{D,2})\left(\frac{Z_1 - Z_\Omega}{Z_{CT} + Z_D}\right) \tag{5.14}$$

where Z_1 is the total, half cell impedance.

Another interesting note about the second harmonic impedance is that, while the individual linear EIS electrode impedances sum to the total impedance, the total second harmonic impedance is given by the difference between the individual electrode impedances. This potentially nonintuitive result can be demonstrated by looking at the definition of the total

and individual impedances,

$$Z_m^i = \frac{V_m^i}{\Delta I^m} \tag{5.15}$$

where m is a positive integer, V_m is the harmonic voltage response at $m\times$ the input frequency, i is *neg* or *pos*, and ΔI is the perturbation amplitude such that $\Delta I = I_1^+ = -I_1^-$. The second harmonic impedance is then defined as,

$$Z_2 = \frac{V_2^+}{(I_1^+)^2} - \frac{V_2^-}{(-I_1^-)^2} = Z_2^+ - Z_2^- \tag{5.16}$$

Equation 5.16 clearly demonstrates that there is no second harmonic NLEIS response for a purely symmetric cell and that small changes in asymmetry can lead to a relatively distinct response. Practically, representing the total second harmonic impedance as the difference of two half cell responses is captured by the negative signs in Figure 5.4b.

Equivalent circuit fitting and confidence intervals

All of the equivalent circuits in this work were fit using SciPy's least squares fitting methods.[147] The linear EIS and second harmonic NLEIS spectra are fit sequentially the model shown in Figure 5.4b where the solid line circuit is first fit to the linear EIS spectrum and the dashed lines indicate elements which are then fit to the second harmonic NLEIS spectrum. To evaluate the goodness of fit an average residual error can be calculated via,

$$E_m = \frac{1}{N}\sum_j^N \sqrt{\left(Z'_{m,model}(\omega_j) - Z'_{m,data}(\omega_j)\right)^2 + \left(Z''_{m,model}(\omega_j) - Z''_{m,data}(\omega_j)\right)^2} \tag{5.17}$$

where $Z'_{m,model}(\omega_j)$ and $Z''_{m,model}(\omega_j)$ are the real and imaginary components of the equivalent circuit values for either the linear EIS ($m = 1$) or second harmonic NLEIS ($m = 2$) response at frequencies ω_j, $Z'_{m,data}(\omega_j)$ and $Z''_{m,data}(\omega_j)$ are the experimentally measured real and imaginary impedance data at frequencies ω_j, and N is the total number of frequencies being fit.

5.2.3 *Initial Results and Discussion*

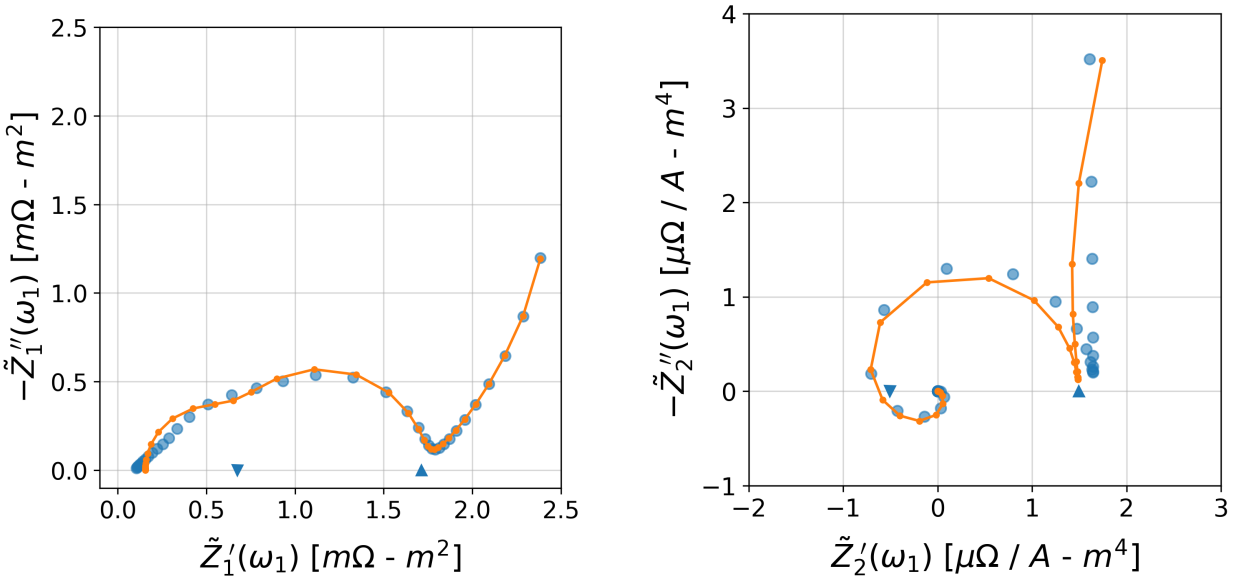

(a) Linear EIS **(b) Second Harmonic NLEIS**

Figure 5.5: Nyquist plots of simulated (a) linear EIS and (b) second harmonic NLEIS spectra and the best fitting Randles equivalent circuits shown in Figures 5.3 and 5.4. The estimated kinetic arc widths from the Randles model fits are indicated by ▲.

Figure 5.5 shows representative linear (a) and second harmonic (b) impedance spectra simulated using the previously described P2D battery model[75] and physicochemical and geometric parameters given in Table A5.3. The spectra cover a wide range of frequencies from 10 kHz to 1 mHz logarithmically sampled with 5 points per decade. The typical linear EIS spectrum shown in Figure 5.5a comprises of a high-frequency real intercept and 45-degree line, a mid-frequency interfacial kinetics and double-layer capacitance regime with two depressed arcs, and a low-frequency, mass transport and thermodynamics dominated tail. In Figure 5.5b, the second harmonic NLEIS spectrum goes to the origin at high-frequencies since the ohmic resistance is a linear process. The asymmetry in the kinetics ($\alpha_{a,pos}$ and $\alpha_{a,neg}$ are not 0.5 here) results in a mid-frequency kinetic arc while the asymmetric diffusional impedance generates a low-frequency tail in the second harmonic NLEIS spectrum. A much

more detailed description of the underlying physicochemical processes that govern the linear and nonlinear harmonic response can be found in previous work.[75]

To interpret and extract quantifiable information from the spectra, the linear EIS and second harmonic NLEIS Randles models, shown in Figures 5.3b and 5.4b, respectively, are fit to the spectra in Figure 5.5. As shown in Figure 5.5a, the linear EIS and second harmonic NLEIS Randles circuits capture the overall impedance responses well with an average error (given by Equation 5.17) of 2.75×10^{-5} and 2.87×10^{-7}, respectively. Specifically, the low-frequency tail is captured well by the spherical particle diffusional impedance elements in the Randles circuit. The depressed kinetic arcs in the experimental mid-frequency response are not perfectly represented by the semicircular Randles circuit fit, although the width of the charge transfer loops (given by the ▲ in Figure 5.5a) is well captured. The second harmonic equivalent of the depressed arcs in the linear EIS spectrum are given by a spiraling $Z_2(\omega_1)$ response in in the mid-frequency regime in Figure 5.5b. These depressed spiraling arcs are also not perfectly represented by the shape of the second harmonic Randles circuit; however, the arc width is captured reasonably well. At high frequencies, the second harmonic NLEIS response goes to the origin, while the linear EIS response goes to the positive real axis via a 45-degree response not captured at all by the Randles circuit. This Gerischer-like effect is a result of the ohmic-kinetic controlled nature of a porous electrode at high frequencies.[148] Here, we will ignore this poorly fitting high frequency regime, however, in the Appendix, we show that so long as the equivalent circuit can adequately capture the arc widths of the kinetic response, the effective length scales used to extract physically meaningful parameters can be accounted for.

The anodic transfer coefficient, α_a, in Equation 5.9 can be extracted from the model fit parameters, by taking the ratio of $R_{CT,2}$ and ${R_{CT}}^2$,

$$\alpha_a = \frac{1}{2}\left(1 - \frac{4F}{RT}\frac{R_{CT,2}}{{R_{CT}}^2}\right) \tag{5.18}$$

Using this equation and the fit shown in Figure 5.5, the anodic charge transfer coefficients

of the positive and negative electrode are estimated as $\alpha_{a,pos} = 0.40$ and $\alpha_{a,neg} = 0.40$, respectively. These values are within the same as the known input parameter value in Table A5.3.

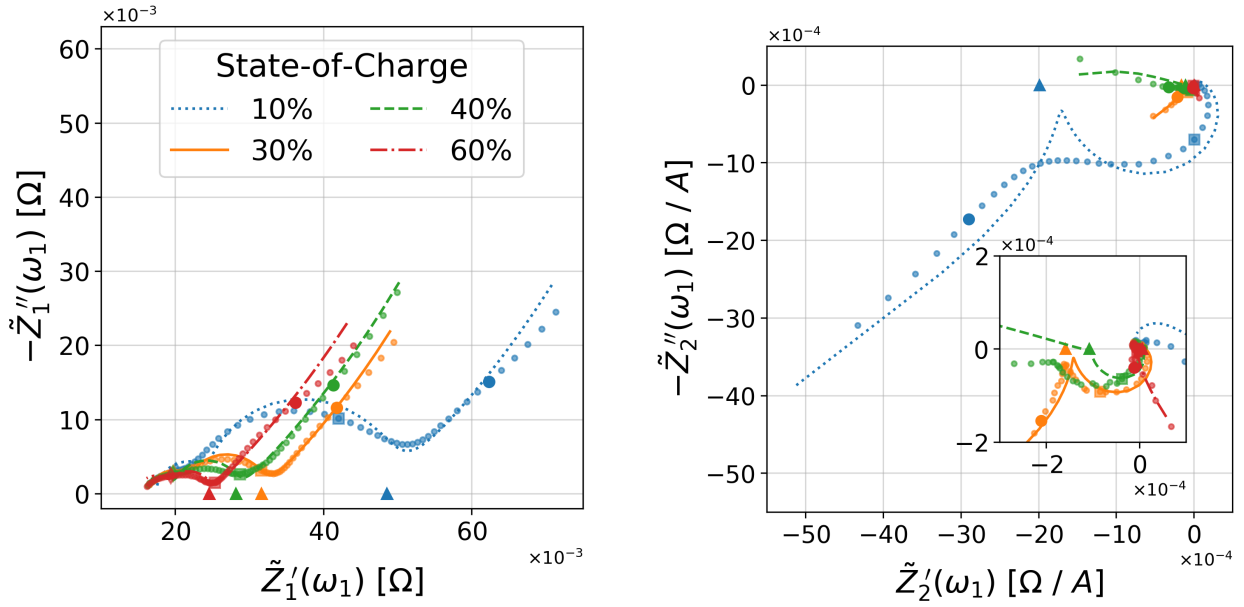

(a) Linear EIS **(b) Second Harmonic NLEIS**

Figure 5.6: Nyquist plots of experimentally measured linear EIS, $\tilde{Z}_1(\omega_1)$, second harmonic NLEIS, $\tilde{Z}_2(\omega_1)$, and their associated Randles circuit fits for an "aged" commercial, 1.5 Ah LiNMC|C cell at several states-of-charge. The data at 1 Hz (■) and 10 mHz (●) are labeled for clarity. The estimated kinetic arc widths from the Randles model fits are indicated by ▲. *Data courtesy of Victor Hu.*

Figure 5.6 shows experimentally measured linear EIS and second harmonic NLEIS spectra for a commercially available, 1.5 Ah LiNMC|C cell at several states-of-charge (SoC). The cell was cycled at constant current, constant voltage at 2C for 100 cycles leading to an overall capacity loss of 0.8%. The spectra shown in Figure 5.6a all have a qualitatively similar shape to the simulated spectra in Figure 5.5a, with a high-frequency real intercept, two depressed kinetic arcs, and a low-frequency tail. As the SoC is decreased the width of the lower frequency kinetic arc (previously associated with the NMC electrode[101]) increases leading to a higher charge transfer resistance, R_{CT}, captured by the Randles circuit fit. Increasing R_{CT}

typically indicates that the exchange current density is decreasing (*i.e.* a higher overpotential is required to drive current at the interface).

A much more diverse set of responses for the second harmonic NLEIS spectra shown in Figure 5.6b when compared to the linear EIS spectra in Figure 5.6a. For example, the ratio of the kinetic arc width at 10% SoC versus 30% SoC is significantly larger in second harmonic NLEIS than in the linear EIS spectra. Moreover, the low-frequency tails of the second harmonic NLEIS spectra point into multiple different quadrants. Analysis of the low-frequency second harmonic NLEIS "tail" is outside the scope of this manuscript, but analysis of the mass-transport and thermodynamics governing these variations will be reported soon.

The idealized semicircular, Randles circuit fits, again, do not fit perfectly to the depressed linear EIS arcs and second harmonic NLEIS spirals in the data; however, the arc widths remain reasonably well captured. Using Equation 5.18, the transfer coefficients of the positive electrode at different SoC are shown in Table A5.2. These measures of asymmetry show that, in addition to the decrease in exchange current density, the charge transfer reaction is more asymmetric in the positive electrode at low SoC. The noninvasive, sensitive nature of the second harmonic NLEIS spectrum could provide a significant opportunity to measure the charge transfer asymmetry in an *in situ* application.

5.2.4 Appendix

Table A5.2: Positive electrode charge transfer coefficients, $\alpha_{a,pos}$, as a function of state-of-charge (SoC) for an aged battery.

SoC	10%	30%	40%	60%
$\alpha_{a,pos}$	0.68	0.59	0.58	0.49

A1 Modifying Randles circuit to account for electrode utilization

The charge transfer resistance described in Equation 5.7 is defined for a planar electrode; however, the porous electrode nature of today's lithium-ion batteries means that specific area, a, and electrode length, l, must be included,

$$R_{CT} = \frac{RT}{ali_0(\alpha_a + \alpha_c)F}. \tag{A5.1}$$

However, the characteristic length may not be equal to the electrode depth when the electrode is not fully utilized. For an underutilized electrode, the characteristic length of the reaction zone is given by the balance between charge transfer and ohmic resistances,[122]

$$l^* = \sqrt{\frac{RT}{ai_0(\alpha_a + \alpha_c)F} \Big/ \left(\frac{1}{\kappa_{eff}} + \frac{1}{\sigma_{eff}}\right)} \tag{A5.2}$$

Thus, for a reaction with fast kinetics and low conductivity, the characteristic reaction zone is small, while for slow kinetics and high conductivity the reaction proceeds across the entire depth of the electrode. The characteristic reaction zone, l^* can be substituted in for l in Equation A5.1,

$$R^*_{CT} = \left(\frac{RT}{Fai_0}\left(\frac{1}{\kappa_{eff}} + \frac{1}{\sigma_{eff}}\right)\right)^{\frac{1}{2}} \tag{A5.3}$$

It should be noted that l^* is a characteristic reaction depth and therefore can be aphysical (i.e. $l^* > l$) under certain conditions. The following section explores the parameter dependence of the charge transfer resistance in a porous electrode to understand when l^* versus l should be used.

A2 Charge transfer resistance parameter dependence

The Bernoulli approximation can be used to write the local dependence of the kinetic arc width on each of the the physicochemical parameters, p, in Equations A5.1 and A5.3 as,

$$\text{arc width} = m_p \epsilon_p + B_p \tag{A5.4}$$

where the arc width is measured from the impedance spectrum, ϵ_p is the normalized change in parameter ($\frac{\Delta p}{p_0}$), and m_p is the local parameter dependence.

For example, the expected local dependence of the kinetic arc width on the exchange current density in either electrode, i_0^i, can be calculated based on R_{CT} from Equation A5.1,

$$\text{arc width} = -\epsilon_{i_0^\pm} \left(\frac{RT}{Fa^\pm l^\pm i_0^\pm} \right) + f(i_0^\pm, i_0^\mp) \tag{A5.5}$$

as well as based on R_{CT}^* from Equation A5.3,

$$\text{arc width} = -\frac{1}{2} \epsilon_{i_0^\pm} \left(\frac{RT}{Fa^\pm i_0^\pm} \left(\frac{1}{\kappa_{eff}} + \frac{1}{\sigma_{eff}} \right) \right)^{\frac{1}{2}} + f(i_0^\pm, i_0^\mp) \tag{A5.6}$$

Consequently we can expect that when normalized by either $-R_{CT}$ or $-R_{CT}^*$ the local dependence on i_0 should go to 1 or $\frac{1}{2}$, respectively.

Figure 5.7 shows varying arc width dependence on the exchange current densities as a function of the relative penetration depth, $\frac{l^*}{l}$, given by Equation A5.2. The charge transfer resistance dependence on i_0 is different for small and large relative penetration depths, $\frac{l^*}{l}$. As expected, the normalized dependence goes to 1 at high ($\frac{l^*}{l} > 1$) relative penetration depths (*i.e.* a fully utilized electrode) and to $\frac{1}{2}$ at low ($\frac{l^*}{l} < 0.1$) relative penetration depths (*i.e.* a underutilized electrode). Thus, R_{CT} should be used to interpret the kinetic arc width when the electrode is fully utilized, and R_{CT}^* should be used when the electrode is very underutilized. Between these two extremes, a model capable of capturing the distribution of current through the electrode depth is required.

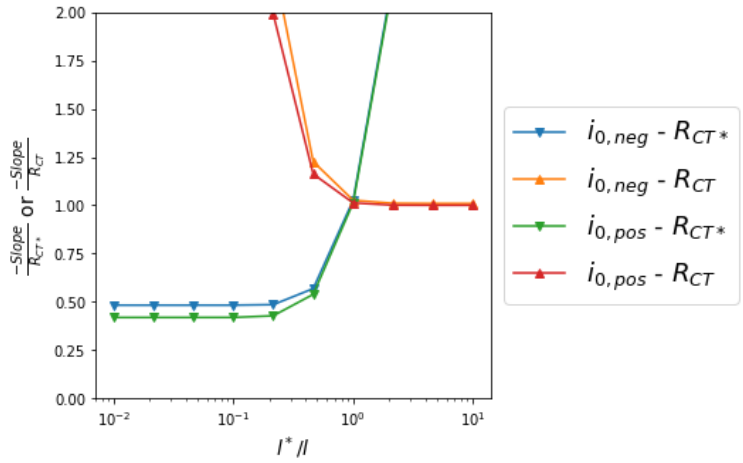

Figure 5.7: Charge transfer width dependence, m_{i_0}, on exchange current density, i_0, as a function of the relative penetration depth, $\frac{l^*}{l}$.

Secondary current distribution in a porous electrode

One further step towards capturing the interacting physics that govern the porous electrode impedance response is to use a full secondary current distribution model. Here, the impedance response of coupled ohmic and kinetic processes is captured by replacing the ohmic and interfacial impedance elements in the Randles circuit with the secondary current distribution porous electrode impedance, Z_{PE},[148]

$$Z_{PE} = \frac{l}{\kappa_{eff} + \sigma_{eff}} \left(\left(\frac{\sigma_{eff}}{\kappa_{eff}} + \frac{\kappa_{eff}}{\sigma_{eff}} \right) \frac{\coth \beta}{\beta} + \frac{2}{\beta \sinh \beta} + 1 \right) \tag{A5.7}$$

where, β, is a ratio of ohmic to kinetic processes,

$$\beta = \sqrt{\frac{\omega_{CT} + j\omega}{\omega_{\Omega}}} \tag{A5.8}$$

and ω_{Ω} is a characteristic ohmic frequency, $\frac{\kappa_{eff}\sigma_{eff}}{aC_{DL}(\kappa_{eff}+\sigma_{eff})l^2}$, and ω_{CT} is a characteristic interfacial frequency, $\frac{i_0 F}{C_{DL}RT}$.

Table A5.3: Physicochemical and geometric parameters for simulated linear EIS and second harmonic NLEIS spectra shown in Figure 5.5.

Physicochemical Parameters

Name	**Value [Units]**
$Brugg$	2.24 $[\mu F/cm^2]$
$C_{dl,neg}$	58.23 $[\mu F/cm^2]$
$C_{dl,pos}$	10.31 $[\mu F/cm^2]$
c_0	1915.9 $[mol/m^3]$
D	2.77 $\times 10^{-10}$ $[m^2/s]$
$D_{s,neg}$	1.56 $\times 10^{-16}$ $[m^2/s]$
$D_{s,pos}$	3.91 $\times 10^{-15}$ $[m^2/s]$
$\frac{\partial U_{neg}}{\partial c^s}$	-.208 $[V \cdot cm^3/mol]$
$\frac{\partial U_{pos}}{\partial c^s}$	-133.1 $[V \cdot cm^3/mol]$
$i_{0,neg}$	6.53 $[A/m^2]$
$i_{0,pos}$	0.19 $[A/m^2]$
t_+^0	0.357 [—]
$\alpha_{a,neg}$	0.41 [—]
$\alpha_{a,pos}$	0.37 [—]
κ	1.57 $[S/m$
σ_{neg}	810.3 $[S/m]$
σ_{pos}	18.8 $[S/m]$

Geometric Parameters

Name	**Value [Units]**
l_{neg}	173.8 $[\mu m]$
l_{sep}	17.1 $[\mu m]$
l_{pos}	140.1 $[\mu m]$
$R_{p,neg}$	14.3 $[\mu m]$
$R_{p,pos}$	1.25 $[\mu m]$
$\epsilon_{f,neg}$	0.18 [—]
$\epsilon_{f,pos}$	0.13 [—]
ϵ_{neg}	0.585 [—]
ϵ_{sep}	0.526 [—]
ϵ_{pos}	0.425 [—]

Chapter 6

CONCLUSIONS AND FUTURE RESEARCH ACTIVITIES

6.1 Thesis Summary

Linear and nonlinear EIS can noninvasively provide information-rich signatures sensitive to the internal state of lithium-ion batteries. Extracting information from these spectra relies on the development and use of physically interpretable models. In this thesis, the theoretical framework for understanding and interpreting the harmonic response of a lithium-ion battery to a moderate-amplitude perturbation was developed. The widely used pseudo-two-dimensional (P2D) battery model was extended to include the efficient computation of nonlinear harmonic impedance spectra given a set of geometric and physicochemical parameters. The model has been useful for exploring the effects of kinetic, transport, and thermodynamic parameters (Chapter 2), interpreting experimental measurements (Chapters 3 and 4 as well as Section 5.2), and understanding model sensitivities and limitations (Section 5.1). To facilitate the use, feedback, and improvement of the model by others, all of the COMSOL, MATLAB, and Python codes developed and used in this work have been released openly under the MIT license.[98,149]

In concert with developing a theoretical framework for the physics-based interpretation of EIS and NLEIS battery spectra, the groundwork for experimentally measuring NLEIS spectra of lithium-ion batteries played a large role in the first several years of this thesis. Development and analysis of diagnostic tests for different potentiostats were performed to understand the capabilities and limitations of today's commercially available instruments. The low-impedance (difficult to control), highly linear (requiring perturbation amplitudes close to the upper limit of potentiostat capabilities) nature of a lithium-ion battery presents a challenge to these instruments. From more flexible software to lower noise signal generation

and measurement, improvements in potentiostat performance have the opportunity to push the limits of what is measurable in a lithium-ion battery.

Initial experimental measurements have demonstrated the significant opportunity for second harmonic NLEIS to increase our ability to noninvasively probe the internal state of lithium-ion batteries. In particular, we have shown that second harmonic NLEIS spectra are a sensitive and specific probe to measure charge transfer asymmetry. Furthermore, a second harmonic extension to the Randles equivalent circuit was developed and used as an easy-to-implement method for extracting parameters from experimental spectra. In particular, NLEIS shows that fresh cells have high symmetry charge transfer ($\alpha_a = \alpha_c = 0.5$) and that a shift toward kinetics that favor oxidation on the positive electrode ($\alpha_{a,pos} > 0.5$, $\alpha_{c,pos} < 0.5$) occurs as the cell is aged. NLEIS measurements also indicate that positive electrode charge transfer is more asymmetric at low states-of-charge. These initial measurements are just the beginning of applying NLEIS to characterize the lithium-ion battery system and significant opportunities exist for further probing the nonlinearities of mass transport (*e.g.* concentration dependent diffusion coefficients), thermodynamics, double-layer capacitance, and even electrode structure. We are just at the beginning of truly leveraging the full power of the noninvasive, sensitive and specific signatures of nonlinear EIS spectra!

The final theme of this thesis centers on building open-software tools to make the work in this thesis more accessible and reproducible. In particular, the ImpedanceAnalyzer (Chapter 4) is a web-based interface for fitting impedance spectra. It provides a convenient GUI for analyzing EIS spectra using physics-based battery models as well as traditional equivalent circuits. Another project, `impedance.py`, is a Python package for fitting experimental impedance spectra. Currently, it provides a scikit-learn-like API[150] to make fitting, predicting, and visualizing equivalent circuit models. Improvements over the closed-source, proprietary software included with most potentiostat instruments include the ability to fully customize the circuits as well as better error analysis, confidence intervals, etc. Further improvements to these tools will be an exciting part of future work.

6.2 Characterizing lithium kinetics with NLEIS

6.2.1 Introduction

The widespread adoption of lithium-ion batteries in long-lasting, capital intensive applications such as electric vehicles and stationary energy storage requires a more accurate and sophisticated characterization of battery lifetime. Many studies of battery aging have demonstrated that multiple modes of battery degradation affect battery state-of-health;[151] however, the plating of lithium at the anode is particularly important to characterize because it not only decreases the performance of the cells,[152,153] but can also be a safety hazard.[154] At the same time, the US Department of Energy has identified charging time as a critical barrier to the widespread adoption of electric vehicles and has set a goal of a 15 minute charging time.[155] Lithium plating — the deposition of metallic lithium instead of intercalation into the anode — is typically caused by fast charging rates, high states-of-charge (SOC), and operation at low temperatures.[156–158] Consequently, developing methods for characterizing the plating of lithium is an important advance for the continued improvement of battery performance.

Lithium plating can be detected via both *in situ* and *ex situ* measurements.[159,160] Typically, *ex situ* methods involve physically opening up the cell post-testing to detect the presence of deposited lithium on the anode after cycling; however, this can be a time-consuming process since the full lifetime of tests needs to occur before the characterization is possible. On the other hand, *in situ* methods can be used to detect lithium plating without opening up the cell. In particular, previously deposited lithium can be detected electrochemically by a high voltage plateau during the subsequent discharge.[156,161] Other methods for detecting the plating of lithium during charging such as directly measuring the anode potential (plating occurs when the anode potential drops below 0 V vs. lithium) or visualizing the plating of lithium via optical or x-ray methods are limited by the required specialized equipment (synchrotron sources) or unique cell designs (reference electrodes or fiber optic cables inserted in cells).

Electrochemical methods for characterizing plating include measuring the coulombic efficiency of the charge/discharge or microcalorimitry; however, early detection of lithium plating is a challenge for these techniques. Moreover, the plating of lithium-ion batteries can be both a reversible and irreversible process[159] and multiple morphologies of the deposited lithium metal have been characterized.[162] Bulk electrochemical methods have a challenge in determining between these types of lithium deposits or even if the signature is indicative of Li plating versus another side reaction.

Electrochemical impedance spectroscopy (EIS) has also been used as a diagnostic method for detecting lithium plating.[163,164] In particular, Schindler et al. demonstrated that the impedance spectrum changed during the voltage relaxation period and they were able to correlate that change to the presence of lithium plating via stripping measurements. Pastor-FernÃąndez et al. compared EIS to typical current-voltage methods and found that with an accurate model several different methods of degradation (loss of lithium versus loss of active material) could be characterized. Unfortunately, these methods are not sufficient as a signature for detecting the presence of lithium deposition due to their lack of sensitivity and specificity.

6.2.2 NLEIS is particularly well suited to probe lithium plating

As described and demonstrated in Chapters 2 and 3 as well as Sections 5.2 and 5.1, the second harmonic NLEIS response is sensitive to charge transfer symmetry. The kinetics of lithium deposition have been found to be asymmetric with transfer coefficients, α, ranging from 0.52 to 0.72.[165,166]

Figure 6.1 describes a schematic of initial experiments using a symmetric $LiC_6|LiC_6$ cell which could provide a second harmonic NLEIS signature of lithium plating. Initially, the symmetry of the cell would produce no second harmonic response at any frequency (Figure 6.1a). Slowly charging the cell would shift the symmetry of the lithium concentration in the electrodes leading to a second harmonic "tail" at low-frequencies (Figure 6.1b) due to asymmetric thermodynamic and mass transport. If the cell was instead charged to the

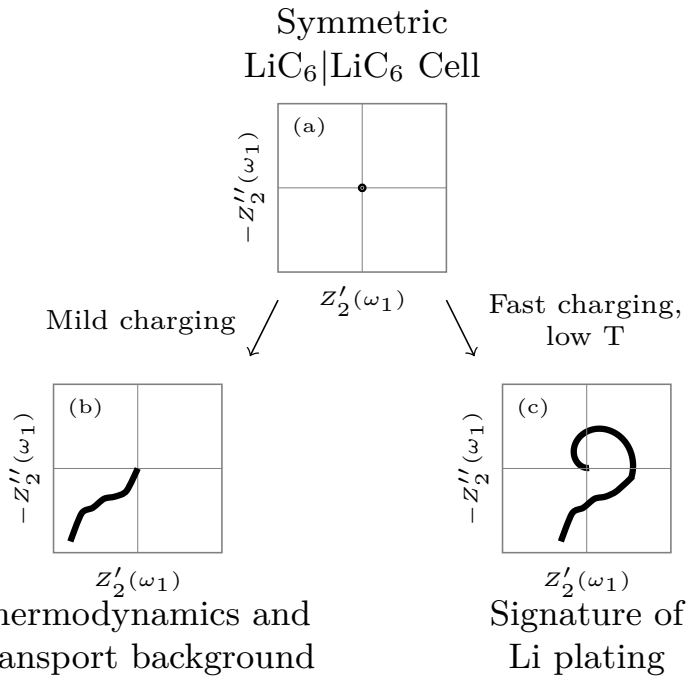

Figure 6.1: Example experiment to determine the second harmonic NLEIS signature of deposited lithium.

same concentration asymmetry, but under fast charge conditions and at low temperature to induce lithium plating, the resulting second harmonic NLEIS spectrum would contain both the low-frequency "tail" and potentially a kinetic arc signature of lithium plating. Additional experiments at different temperatures and charging rates could explore the detection limits and sensitivity to deposit structure (*i.e.* mossy vs. dendritic). Advances in potentiostat and FRA equipment to reduce harmonic distortion in the input perturbations while increasing the signal-to-noise ratio of measurements could significantly improve these efforts by enabling measurements to be made at higher frequencies.

The ultimate power of a second harmonic NLEIS based signature for lithium plating could ultimately come in the form of an *in situ* and *in operando* diagnostic in which an appropriate frequency (or range of frequencies) is applied and monitored during charging. Charging rate could then respond to the signature for lithium plating ensuring that the charging happens

as fast as possible while avoiding safety or lifetime issues. Coupled with a physics-based model, controlling a battery during fast charging via an internal state sensitive measurement would be a significant improvement to battery management.

BIBLIOGRAPHY

[1] J. Ross Macdonald, editor. *Impedance Spectroscopy: Emphasizing Solid Materials and Systems*. Wiley, New York, 1987. ISBN 978-0-471-83122-8.

[2] Evgenij Barsoukov and J. Ross Macdonald, editors. *Impedance Spectroscopy: Theory, Experiment, and Applications*. Wiley-Interscience, Hoboken, N.J, 2nd ed edition, 2005. ISBN 978-0-471-64749-2.

[3] Mark E. Orazem and Bernard Tribollet. *Electrochemical Impedance Spectroscopy*. The Electrochemical Society series. Wiley, Hoboken, N.J, 2008. ISBN 978-0-470-04140-6.

[4] Francisco Fabregat-Santiago, Juan Bisquert, Germà Garcia-Belmonte, Gerrit Boschloo, and Anders Hagfeldt. Influence of electrolyte in transport and recombination in dye-sensitized solar cells studied by impedance spectroscopy. *Solar Energy Materials and Solar Cells*, 87(1-4):117–131, May 2005. ISSN 09270248. DOI: 10.1016/j.solmat.2004.07.017.

[5] Qing Wang, Jacques-E. Moser, and Michael Grätzel. Electrochemical Impedance Spectroscopic Analysis of Dye-Sensitized Solar Cells. *The Journal of Physical Chemistry B*, 109(31):14945–14953, August 2005. ISSN 1520-6106, 1520-5207. DOI: 10.1021/jp052768h.

[6] Digby D. Macdonald, Silvia Real, Stuart I. Smedley, and Mirna Urquidi-Macdonald. Evaluation of Alloy Anodes for Aluminum-Air Batteries IV . Electrochemical Impedance Analysis of Pure Aluminum in at 25°C. *Journal of The Electrochemical Society*, 135(10):2410–2414, January 1988. ISSN 0013-4651, 1945-7111. DOI: 10.1149/1.2095348.

[7] Digby D. Macdonald. Reflections on the history of electrochemical impedance spectroscopy. *Electrochimica Acta*, 51(8-9):1376–1388, January 2006. ISSN 00134686. DOI: 10.1016/j.electacta.2005.02.107.

[8] M. D. Levi and D. Aurbach. Simultaneous measurements and modeling of the electrochemical impedance and the cyclic voltammetric characteristics of graphite electrodes doped with lithium. *The Journal of Physical Chemistry B*, 101(23):4630–4640, 1997. DOI: 10.1021/jp9701909.

[9] E. Warburg. Ueber das Verhalten sogenannter unpolarisirbarer Elektroden gegen Wechselstrom. *Annalen der Physik und Chemie*, 303(3):493–499, 1899. ISSN 00033804, 15213889. DOI: 10.1002/andp.18993030302.

[10] M. D. Levi and D. Aurbach. Diffusion coefficients of lithium ions during intercalation into graphite derived from the simultaneous measurements and modeling of electrochemical impedance and potentiostatic intermittent titration characteristics of thin graphite electrodes. *The Journal of Physical Chemistry B*, 101(23):4641–4647, 1997. DOI: 10.1021/jp9701911.

[11] Robert De Levie. Electrochemical response of porous and rough electrodes. *Advances in electrochemistry and electrochemical engineering*, 6:329–397, 1967.

[12] Marco Musiani, Mark Orazem, Bernard Tribollet, and Vincent Vivier. Impedance of blocking electrodes having parallel cylindrical pores with distributed radii. *Electrochimica Acta*, 56(23):8014–8022, September 2011. ISSN 00134686. DOI: 10.1016/j.electacta.2010.12.004.

[13] N. Fouquet, C. Doulet, C. Nouillant, G. Dauphin-Tanguy, and B. Ould-Bouamama. Model based PEM fuel cell state-of-health monitoring via ac impedance measurements. *Journal of Power Sources*, 159(2):905–913, September 2006. ISSN 03787753. DOI: 10.1016/j.jpowsour.2005.11.035.

[14] R. Onanena, L. Oukhellou, D. Candusso, F. Harel, D. Hissel, and P. Aknin. Fuel cells static and dynamic characterizations as tools for the estimation of their ageing time. *International Journal of Hydrogen Energy*, 36(2):1730–1739, January 2011. ISSN 03603199. DOI: 10.1016/j.ijhydene.2010.10.064.

[15] Pritpal Singh, Ramana Vinjamuri, Xiquan Wang, and David Reisner. Fuzzy logic modeling of EIS measurements on lithium-ion batteries. *Electrochimica Acta*, 51(8-9): 1673–1679, January 2006. ISSN 00134686. DOI: 10.1016/j.electacta.2005.02.143.

[16] B. Saha, K. Goebel, S. Poll, and J. Christophersen. Prognostics Methods for Battery Health Monitoring Using a Bayesian Framework. *IEEE Transactions on Instrumentation and Measurement*, 58(2):291–296, February 2009. ISSN 0018-9456, 1557-9662. DOI: 10.1109/TIM.2008.2005965.

[17] Guofeng Cui, Hong Liu, Gang Wu, Jianwei Zhao, Shuqin Song, and Pei Kang Shen. Electrochemical Impedance Spectroscopy and First-Principle Investigations on the Oxidation Mechanism of Hypophosphite Anion in the Electroless Deposition System of Nickel. *The Journal of Physical Chemistry C*, 112(12):4601–4607, March 2008. ISSN 1932-7447, 1932-7455. DOI: 10.1021/jp7097119.

[18] J. Segalini, B. Daffos, P.L. Taberna, Y. Gogotsi, and P. Simon. Qualitative Electrochemical Impedance Spectroscopy study of ion transport into sub-nanometer carbon pores in Electrochemical Double Layer Capacitor electrodes. *Electrochimica Acta*, 55 (25):7489–7494, October 2010. ISSN 00134686. DOI: 10.1016/j.electacta.2010.01.003.

[19] J.R. Wilson, D.T. Schwartz, and S.B. Adler. Nonlinear electrochemical impedance spectroscopy for solid oxide fuel cell cathode materials. *Electrochimica Acta*, 51(8-9): 1389–1402, January 2006. ISSN 00134686. DOI: 10.1016/j.electacta.2005.02.109.

[20] Stephen Fletcher. Tables of Degenerate Electrical Networks for Use in the Equivalent-Circuit Analysis of Electrochemical Systems. *Journal of The Electrochemical Society*, 141(7):1823–1826, 1994. DOI: 10.1149/1.2055011.

[21] K. Darowicki. Linearization in impedance measurements. *Electrochimica Acta*, 42(12): 1781–1788, 1997. ISSN 0013-4686. DOI: 10.1016/S0013-4686(96)00377-5.

[22] K. Darowicki and J. Majewska. The effect of a polyharmonic structure of the perturbation signal on the results of harmonic analysis of the current of a first-order electrode reaction. *Electrochimica acta*, 44(2):483–490, 1998. DOI: 10.1016/S0013-4686(98)00062-0.

[23] M. Kiel, O. Bohlen, and D.U. Sauer. Harmonic analysis for identification of nonlinearities in impedance spectroscopy. *Electrochimica Acta*, 53(25):7367–7374, October 2008. ISSN 00134686. DOI: 10.1016/j.electacta.2008.01.089.

[24] Bryan Hirschorn, Bernard Tribollet, and Mark E. Orazem. On Selection of the Perturbation Amplitude Required to Avoid Nonlinear Effects in Impedance Measurements. *Israel Journal of Chemistry*, 48(3-4):133–142, December 2008. ISSN 00212148, 18695868. DOI: 10.1560/IJC.48.3-4.133.

[25] J.J. Giner-Sanz, E.M. Ortega, and V. Pérez-Herranz. Total harmonic distortion based method for linearity assessment in electrochemical systems in the context of EIS. *Electrochimica Acta*, 186:598–612, December 2015. ISSN 00134686. DOI: 10.1016/j.electacta.2015.10.152.

[26] J. J. Giner-Sanz, E. M. Ortega, and V. Pérez-Herranz. Harmonic Analysis Based Method for Perturbation Amplitude Optimization for EIS Measurements. *Journal of The Electrochemical Society*, 164(13):H918–H924, 2017. DOI: 10.1149/2.1451713jes.

[27] Fathima Fasmin and Ramanathan Srinivasan. Review—Nonlinear Electrochemical Impedance Spectroscopy. *Journal of The Electrochemical Society*, 164(7):H443–H455, 2017. ISSN 0013-4651, 1945-7111. DOI: 10.1149/2.0391707jes.

[28] L. Marrucci, D. Paparo, G. Cerrone, C. De Lisio, E. Santamato, S. Solimeno, S. Ardizzone, and P. Quagliotto. Probing interfacial properties by optical second-harmonic generation. *Optics and lasers in engineering*, 37(5):601–610, 2002. DOI: 10.1016/S0143-8166(01)00113-0.

[29] Jie Shan, Ajay Nahata, and Tony F. Heinz. Tetrahertz Time-domain Spectroscopy Based on Nonlinear Optics. *Journal of Nonlinear Optical Physics & Materials*, 11(01): 31–48, March 2002. ISSN 0218-8635, 1793-6624. DOI: 10.1142/S0218863502000845.

[30] Kazimierz Darowicki. Fundamental-harmonic impedance of first-order electrode reactions. *Electrochimica Acta*, 39(18):2757–2762, December 1994. ISSN 0013-4686. DOI: 10.1016/0013-4686(94)00302-5.

[31] Kazimierz Darowicki. Corrosion rate measurements by non-linear electrochemical impedance spectroscopy. *Corrosion Science*, 37(6):913–925, 1995. DOI: 10.1016/0010-938X(95)00004-4.

[32] Kazimierz Darowicki. The amplitude analysis of impedance spectra. *Electrochimica Acta*, 40(4):439–445, March 1995. ISSN 00134686. DOI: 10.1016/0013-4686(94)00303-I.

[33] K. Darowicki and J. Orlikowski. Fast method for the determination of the charge transfer coefficient of an electrode reaction. *Electrochimica Acta*, 44(2):433–436, September 1998. ISSN 0013-4686. DOI: 10.1016/S0013-4686(98)00052-8.

[34] J. P. Diard, B. Le Gorrec, and C. Montella. Deviation from the polarization resistance due to non-linearity I - theoretical formulation. *Journal of Electroanalytical Chemistry*, 432(1):27–39, July 1997. ISSN 1572-6657. DOI: 10.1016/S0022-0728(97)00213-1.

[35] J. P. Diard, B. Le Gorrec, and C. Montella. Deviation of the polarization resistance due to non-linearity II. Application to electrochemical reactions. *Journal of Electroanalytical Chemistry*, 432(1):41–52, July 1997. ISSN 1572-6657. DOI: 10.1016/S0022-0728(97)00234-9.

[36] J. P. Diard, B. Le Gorrec, and C. Montella. Deviation of the polarization resistance due to non-linearity. III—Polarization resistance determination from non-linear impedance measurements. *Journal of Electroanalytical Chemistry*, 432(1):53–62, July 1997. ISSN 1572-6657. DOI: 10.1016/S0022-0728(97)00233-7.

[37] J.-P. Diard, B. Le Gorrec, and C. Montella. Corrosion rate measurements by non-linear electrochemical impedance spectroscopy. Comments on the paper by K. Darowicki, Corros. Sci. 37, 913 (1995). *Corrosion science*, 40(2):495–508, 1998. DOI: 10.1016/S0010-938X(97)00125-X.

[38] J. Devay and L. Mészáros. Study of the Rate of Corrosion of Metals by a Faradaic Distortion Method. *Acta Chim. Acad. Sci. Hung.*, 100:183, 1979.

[39] L. Mészáros, G. Mészáros, and B. Lengyel. Application of Harmonic Analysis in the Measuring Technique of Corrosion. *Journal of The Electrochemical Society*, 141(8): 2068–2071, January 1994. ISSN 0013-4651, 1945-7111. DOI: 10.1149/1.2055062.

[40] Kazimierz Darowicki and Joanna Majewska. Harmonic Analysis Of Electrochemical and Corrosion Systems-A Review. *Corrosion reviews*, 17(5-6):383–400, 1999. DOI: 10.1515/CORRREV.1999.17.5-6.383.

[41] Satoshi Nakata, Kenichi Yoshikawa, and Takehisa Matsuda. Voltage-dependent capacitance as a probe for albumin adsorption onto a solid surface. *Biophysical Chemistry*, 42(2):213–220, February 1992. ISSN 03014622. DOI: 10.1016/0301-4622(92)85011-R.

[42] Satoshi Nakata, Rie Takitani, and Yoko Hirata. Discrimination of glucose from its interferences using an amperometric sensor based on electrochemical nonlinearity. *Analytical Chemistry*, 70(20):4304–4308, 1998. DOI: 10.1021/ac980442h.

[43] Satoshi Nakata, Kaori Takemura, and Kayoko Neya. Chemical Sensor Based on Nonlinearity: Principle and Application. *Analytical Sciences*, 17(3):365–373, 2001. ISSN 0910-6340, 1348-2246. DOI: 10.2116/analsci.17.365.

[44] Vadim F. Lvovich and Matthew F. Smiechowski. Non-linear impedance analysis of industrial lubricants. *Electrochimica Acta*, 53(25):7375–7385, October 2008. ISSN 0013-4686. DOI: 10.1016/j.electacta.2007.12.014.

[45] Matthew F. Smiechowski, Vadim F. Lvovich, Sowmya Srikanthan, and Roy L. Silverstein. Non-linear impedance characterization of blood cells-derived microparticle biomarkers suspensions. *Electrochimica Acta*, 56(23):7763–7771, September 2011. ISSN 0013-4686. DOI: 10.1016/j.electacta.2011.03.116.

[46] D. T. Schwartz, P. Stroeve, and B. G. Higgins. Fourier Transform Methods in Hydrodynamic Modulation Voltammetry. *Journal of The Electrochemical Society*, 136(6): 1755–1764, June 1989. DOI: 10.1149/1.2097006.

[47] J. Antonio Medina and Daniel T. Schwartz. Nonlinear dynamics of modulated flow between a porous injector and an impermeable substrate. *Physics of Fluids (1994-present)*, 8(11):2895–2905, 1996. DOI: 10.1063/1.869129.

[48] J. Antonio Medina and Daniel T. Schwartz. Nonlinear Dynamics of Limiting Current in the Flow-Modulated Uniform-Injection Cell. *Journal of the Electrochemical Society*, 144(1):155–164, 1997. DOI: 10.1149/1.1837378.

[49] Jamie Wilson. Measurement and Prediction of Nonlinear Harmonics as a Tool Dynamic Characterization of Electrochemical Systems, 2007.

[50] Thomas Kadyk, Richard Hanke-Rauschenbach, and Kai Sundmacher. Nonlinear frequency response analysis of dehydration phenomena in polymer electrolyte membrane fuel cells. *International Journal of Hydrogen Energy*, 37(9):7689–7701, May 2012. ISSN 03603199. DOI: 10.1016/j.ijhydene.2012.01.148.

[51] Boris Bensmann, Menka Petkovska, Tanja Vidaković-Koch, Richard Hanke-Rauschenbach, and Kai Sundmacher. Nonlinear Frequency Response of Electrochemical Methanol Oxidation Kinetics: A Theoretical Analysis. *Journal of The Electrochemical Society*, 157(9):B1279–B1289, January 2010. ISSN 0013-4651, 1945-7111. DOI: 10.1149/1.3446836.

[52] Nina Harting, Nicolas Wolff, Fridolin Röder, and Ulrike Krewer. Nonlinear Frequency Response Analysis (NFRA) of Lithium-Ion Batteries. *Electrochimica Acta*, 248:133–139, September 2017. ISSN 0013-4686. DOI: 10.1016/j.electacta.2017.04.037.

[53] Nina Harting, René Schenkendorf, Nicolas Wolff, and Ulrike Krewer. State-of-Health Identification of Lithium-Ion Batteries Based on Nonlinear Frequency Response Analysis: First Steps with Machine Learning. *Applied Sciences*, 8(5):821, May 2018. DOI: 10.3390/app8050821.

[54] Nina Harting, Nicolas Wolff, and Ulrike Krewer. Identification of Lithium Plating in Lithium-Ion Batteries using Nonlinear Frequency Response Analysis (NFRA). *Electrochimica Acta*, 281:378–385, August 2018. ISSN 0013-4686. DOI: 10.1016/j.electacta.2018.05.139.

[55] Nicolas Wolff, Nina Harting, Marco Heinrich, Fridolin Röder, and Ulrike Krewer. Nonlinear Frequency Response Analysis on Lithium-Ion Batteries: A Model-Based Assessment. *Electrochimica Acta*, 260:614–622, January 2018. ISSN 0013-4686. DOI: 10.1016/j.electacta.2017.12.097.

[56] Bernard Tribollet. The Modulated Flow at a Rotating Disk Electrode. *Journal of The Electrochemical Society*, 130(10):2016, 1983. ISSN 00134651. DOI: 10.1149/1.2119512.

[57] Qingzhi Guo and Ralph E. White. A Steady-State Impedance Model for a PEMFC Cathode. *Journal of The Electrochemical Society*, 151(4):E133, 2004. ISSN 00134651. DOI: 10.1149/1.1648024.

[58] Jeremy P. Meyers, Marc Doyle, Robert M. Darling, and John Newman. The impedance response of a porous electrode composed of intercalation particles. *Journal of The Electrochemical Society*, 147(8):2930–2940, 2000. DOI: 10.1149/1.1393627.

[59] Marc Doyle, Jeremy P. Meyers, and John Newman. Computer simulations of the impedance response of lithium rechargeable batteries. *Journal of The Electrochemical Society*, 147(1):99–110, 2000. DOI: 10.1149/1.1393162.

[60] Sheba Devan, Venkat R. Subramanian, and R. E. White. Analytical Solution for the Impedance of a Porous Electrode. *Journal of The Electrochemical Society*, 151(6): A905, 2004. ISSN 00134651. DOI: 10.1149/1.1739218.

[61] Dennis Dees, Evren Gunen, Daniel Abraham, Andrew Jansen, and Jai Prakash. Alternating Current Impedance Electrochemical Modeling of Lithium-Ion Positive Electrodes. *Journal of The Electrochemical Society*, 152(7):A1409, 2005. ISSN 00134651. DOI: 10.1149/1.1928169.

[62] D.P. Abraham, S. Kawauchi, and D.W. Dees. Modeling the impedance versus voltage characteristics of LiNi0.8Co0.15Al0.05O2. *Electrochimica Acta*, 53(5):2121–2129, January 2008. ISSN 00134686. DOI: 10.1016/j.electacta.2007.09.018.

[63] David A. C. Beck, James M. Carothers, Venkat R. Subramanian, and Jim Pfaendtner. Data science: Accelerating innovation and discovery in chemical engineering. *AIChE Journal*, 62(5):1402–1416, May 2016. ISSN 00011541. DOI: 10.1002/aic.15192.

[64] Sijmen de Jong, Barry M. Wise, and N. Lawrence Ricker. Canonical partial least squares and continuum power regression. *Journal of Chemometrics*, 15 (2):85–100, February 2001. ISSN 0886-9383, 1099-128X. DOI: 10.1002/1099-128X(200102)15:2<85::AID-CEM601>3.0.CO;2-9.

[65] Kevin P. Murphy. *Machine Learning: A Probabilistic Perspective*. Adaptive computation and machine learning series. MIT Press, Cambridge, MA, 2012. ISBN 978-0-262-01802-9.

[66] https://www.nb.uw.edu/mvsa/multivariate-surface-analysis-homepage.

[67] O. D. Sanni, M. S. Wagner, D. Briggs, D. G. Castner, and J. C. Vickerman. Classification of adsorbed protein static ToF-SIMS spectra by principal component analysis and neural networks. *Surface and Interface Analysis*, 33(9):715–728, September 2002. ISSN 0142-2421, 1096-9918. DOI: 10.1002/sia.1438.

[68] William A. Steen, Kavita M. Jeerage, and Daniel T. Schwartz. Raman spectroscopy of redox activity in cathodically electrodeposited nickel hexacyanoferrate thin films. *Applied spectroscopy*, 56(8):1021–1029, 2002. DOI: 10.1366/000370202760249756.

[69] Neal Dawson-Elli, Seong Beom Lee, Manan Pathak, Kishalay Mitra, and Venkat R. Subramanian. Data Science Approaches for Electrochemical Engineers: An Introduction through Surrogate Model Development for Lithium-Ion Batteries. *Journal of The Electrochemical Society*, 165(2):A1–A15, January 2018. ISSN 0013-4651, 1945-7111. DOI: 10.1149/2.1391714jes.

[70] Wesley Beckner, Coco M. Mao, and Jim Pfaendtner. Statistical models are able to predict ionic liquid viscosity across a wide range of chemical functionalities and experimental conditions. *Molecular Systems Design & Engineering*, 3(1):253–263, February 2018. ISSN 2058-9689. DOI: 10.1039/C7ME00094D.

[71] Janet Matsen, Song Yang, Lisa Stein, David Beck, and Marina Kalyuzhanaya. Global Molecular Analyses of Methane Metabolism in Methanotrophic Alphaproteobacterium, Methylosinus trichosporium OB3b. Part I: Transcriptomic Study. *Frontiers in Microbiology*, 4:40, 2013. ISSN 1664-302X. DOI: 10.3389/fmicb.2013.00040.

[72] Blake R. Hough, Daniel T. Schwartz, and Jim Pfaendtner. Detailed Kinetic Modeling of Lignin Pyrolysis for Process Optimization. *Industrial & Engineering Chemistry Research*, 55(34):9147–9153, August 2016. ISSN 0888-5885, 1520-5045. DOI: 10.1021/acs.iecr.6b02092.

[73] Matthew D. Murbach and Daniel T. Schwartz. Analysis of Li-ion battery electrochemical impedance spectroscopy data: An easy-to-implement approach for physics-based parameter estimation using an open-source tool. *Journal of The Electrochemical Society*, 165(2):A297–A304, 2018. DOI: 10.1149/2.1021802jes.

[74] Blake Hough, Chris Fu, and Swapil Paliwal. Savvy: Visualize High Dimensionality Sensitivity Analysis Data. Updated With Full Sensitivity Analysis From Ligpy Model. May 2016. DOI: 10.5281/zenodo.53099.

[75] Matthew D. Murbach and Daniel T. Schwartz. Extending Newman's Pseudo-Two-Dimensional Lithium-Ion Battery Impedance Simulation Approach to Include the Nonlinear Harmonic Response. *Journal of The Electrochemical Society*, 164(11):E3311–E3320, 2017. DOI: 10.1149/2.0301711jes.

[76] MGSR Thomas, P. G. Bruce, and J. B. Goodenough. AC Impedance Analysis of Polycrystalline Insertion Electrodes: Application to $Li_{1-x}CoO_2$. *Journal of The Electrochemical Society*, 132(7):1521–1528, 1985. DOI: 10.1149/1.2114158.

[77] D. Andre, M. Meiler, K. Steiner, Ch. Wimmer, T. Soczka-Guth, and D.U. Sauer. Characterization of high-power lithium-ion batteries by electrochemical impedance spectroscopy. I. Experimental investigation. *Journal of Power Sources*, 196(12):5334–5341, June 2011. ISSN 03787753. DOI: 10.1016/j.jpowsour.2010.12.102.

[78] Johannes Landesfeind, Johannes Hattendorff, Andreas Ehrl, Wolfgang A. Wall, and Hubert A. Gasteiger. Tortuosity Determination of Battery Electrodes and Separators by Impedance Spectroscopy. *Journal of The Electrochemical Society*, 163(7):A1373–A1387, 2016. DOI: 10.1149/2.1141607jes.

[79] B. Saha, K. Goebel, and J. Christophersen. Comparison of prognostic algorithms for estimating remaining useful life of batteries. *Transactions of the Institute of Measurement and Control*, 31(3-4):293–308, June 2009. ISSN 0142-3312. DOI: 10.1177/0142331208092030.

[80] Evgenij Barsoukov, Jong Hyun Kim, Jong Hun Kim, Chul Oh Yoon, and Hosull Lee. Effect of Low-Temperature Conditions on Passive Layer Growth on Li Intercalation Materials In Situ Impedance Study. *Journal of The Electrochemical Society*, 145(8): 2711–2717, 1998. DOI: 10.1149/1.1838703.

[81] Ping Yu, Branko N. Popov, James A. Ritter, and Ralph E. White. Determination of the lithium ion diffusion coefficient in graphite. *Journal of The Electrochemical Society*, 146(1):8–14, 1999. DOI: 10.1149/1.1391556.

[82] Uwe Tröltzsch, Olfa Kanoun, and Hans-Rolf Tränkler. Characterizing aging effects of lithium ion batteries by impedance spectroscopy. *Electrochimica Acta*, 51(8-9):1664–1672, January 2006. ISSN 00134686. DOI: 10.1016/j.electacta.2005.02.148.

[83] R. Fathi, J. C. Burns, D. A. Stevens, Hui Ye, Chao Hu, Gaurav Jain, Erik Scott, Craig Schmidt, and J. R. Dahn. Ultra High-Precision Studies of Degradation Mechanisms in Aged LiCoO2/Graphite Li-Ion Cells. *Journal of The Electrochemical Society*, 161(10): A1572–A1579, January 2014. ISSN 0013-4651, 1945-7111. DOI: 10.1149/2.0321410jes.

[84] Seong Jin An, Jianlin Li, Claus Daniel, Debasish Mohanty, Shrikant Nagpure, and David L. Wood. The state of understanding of the lithium-ion-battery graphite solid electrolyte interphase (SEI) and its relationship to formation cycling. *Carbon*, 105: 52–76, August 2016. ISSN 00086223. DOI: 10.1016/j.carbon.2016.04.008.

[85] Godfrey Sikha and Ralph E. White. Analytical Expression for the Impedance Response of an Insertion Electrode Cell. *Journal of The Electrochemical Society*, 154(1):A43, 2007. ISSN 00134651. DOI: 10.1149/1.2372695.

[86] Godfrey Sikha and Ralph E. White. Analytical Expression for the Impedance Response for a Lithium-Ion Cell. *Journal of The Electrochemical Society*, 155(12):A893, 2008. ISSN 00134651. DOI: 10.1149/1.2976359.

[87] Rik-Wouter Bosch and W. F. Bogaerts. Instantaneous corrosion rate measurement with small-amplitude potential intermodulation techniques. *Corrosion*, 52(3):204–212, 1996. DOI: 10.5006/1.3292115.

[88] R. W. Bosch, Juliaan Hubrecht, W. F. Bogaerts, and B. C. Syrett. Electrochemical frequency modulation: A new electrochemical technique for online corrosion monitoring. *Corrosion*, 57(1):60–70, 2001. DOI: 10.5006/1.3290331.

[89] Marc Doyle, John Newman, Antoni S. Gozdz, Caroline N. Schmutz, and Jean-Marie Tarascon. Comparison of modeling predictions with experimental data from plastic lithium ion cells. *Journal of the Electrochemical Society*, 143(6):1890–1903, 1996. DOI: 10.1149/1.1836921.

[90] Marc Doyle, Thomas F. Fuller, and John Newman. Modeling of galvanostatic charge and discharge of the lithium/polymer/insertion cell. *Journal of the Electrochemical Society*, 140(6):1526–1533, 1993. DOI: 10.1149/1.2221597.

[91] Thomas F. Fuller, Marc Doyle, and John Newman. Simulation and optimization of the dual lithium ion insertion cell. *Journal of the Electrochemical Society*, 141(1):1–10, 1994. DOI: 10.1149/1.2054684.

[92] Manan Pathak, Dayaram Sonawane, Shriram Santhanagopalan, Richard D. Braatz, and Venkat R. Subramanian. (Invited) Analyzing and Minimizing Capacity Fade through Optimal Model-based Control - Theory and Experimental Validation. *ECS Transactions*, 75(23):51–75, April 2017. ISSN 1938-6737, 1938-5862. DOI: 10.1149/07523.0051ecst.

[93] Daniel T. Schwartz. Measurements of Steady Axial Streaming at a Rotating Disc with Torsional Oscillations. *Proceedings of the Royal Society of London A: Mathematical, Physical and Engineering Sciences*, 442(1915):397–407, August 1993. DOI: 10.1098/rspa.1993.0110.

[94] Jamie R. Wilson, Stuart B. Adler, and Daniel T. Schwartz. Full-spectrum nonlinear response of a sinusoidally modulated rotating disk electrode. *Physics of Fluids*, 17(6): 063601, 2005. ISSN 10706631. DOI: 10.1063/1.1920547.

[95] Paul WC Northrop, Venkatasailanathan Ramadesigan, Sumitava De, and Venkat R. Subramanian. Coordinate transformation, orthogonal collocation, model reformulation and simulation of electrochemical-thermal behavior of lithium-ion battery stacks. *Journal of The Electrochemical Society*, 158(12):A1461–A1477, 2011. DOI: 10.1149/2.058112jes.

[96] Ning Xu and D. Jason Riley. Nonlinear analysis of a classical system: The Faradaic process. *Electrochimica Acta*, 94:206–213, April 2013. ISSN 00134686. DOI: 10.1016/j.electacta.2013.01.141.

[97] C. Heubner, M. Schneider, and A. Michaelis. Investigation of charge transfer kinetics of Li-Intercalation in LiFePO4. *Journal of Power Sources*, 288:115–120, August 2015. ISSN 03787753. DOI: 10.1016/j.jpowsour.2015.04.103.

[98] Matthew D. Murbach[‡], Victor W. Hu[‡], and Daniel T. Schwartz. Nonlinear electrochemical impedance spectroscopy of lithium-ion batteries: Experimental approach, analysis, and initial findings. *Open Science Framework*, 2018. DOI: https://osf.io/tdnwa/.

[99] Michel Armand and J.-M. Tarascon. Building better batteries. *Nature*, 451(7179): 652–657, 2008. DOI: 10.1038/451652a.

[100] S. S. Zhang, K. Xu, and T. R. Jow. EIS study on the formation of solid electrolyte interface in Li-ion battery. *Electrochimica Acta*, 51(8):1636–1640, January 2006. ISSN 0013-4686. DOI: 10.1016/j.electacta.2005.02.137.

[101] James A. Gilbert, Javier Bareño, Timothy Spila, Stephen E. Trask, Dean J. Miller, Bryant J. Polzin, Andrew N. Jansen, and Daniel P. Abraham. Cycling Behavior of NCM523/Graphite Lithium-Ion Cells in the 3–4.4 V Range: Diagnostic Studies of Full Cells and Harvested Electrodes. *Journal of The Electrochemical Society*, 164(1): A6054–A6065, January 2017. ISSN 0013-4651, 1945-7111. DOI: 10.1149/2.0081701jes.

[102] Tetsuya Osaka, Daikichi Mukoyama, and Hiroki Nara. Review—Development of Diagnostic Process for Commercially Available Batteries, Especially Lithium Ion Battery, by Electrochemical Impedance Spectroscopy. *Journal of The Electrochemical Society*, 162(14):A2529–A2537, 2015. DOI: 10.1149/2.0141514jes.

[103] Qing Mao and Ulrike Krewer. Sensing methanol concentration in direct methanol fuel cell with total harmonic distortion: Theory and application. *Electrochimica Acta*, 68: 60–68, April 2012. ISSN 0013-4686. DOI: 10.1016/j.electacta.2012.02.018.

[104] Anup Barai, Gael H. Chouchelamane, Yue Guo, Andrew McGordon, and Paul Jennings. A study on the impact of lithium-ion cell relaxation on electrochemical impedance spectroscopy. *Journal of Power Sources*, 280:74–80, April 2015. ISSN 03787753. DOI: 10.1016/j.jpowsour.2015.01.097.

[105] Matthew D. Murbach, Victor W. Hu, and Daniel T. Schwartz. Data and Supplementary Notebook for "Lithium-Ion Battery Characterization with Nonlinear Electrochemical Impedance Spectroscopy: Experimental approach, insights, and initial findings". 2018. DOI: 10.17605/OSF.IO/TDNWA.

[106] M. Schönleber, D. Klotz, and E. Ivers-Tiffée. A Method for Improving the Robustness of linear Kramers-Kronig Validity Tests. *Electrochimica Acta*, 131:20–27, June 2014. ISSN 0013-4686. DOI: 10.1016/j.electacta.2014.01.034.

[107] Salim Erol and Mark E. Orazem. The influence of anomalous diffusion on the impedance response of LiCoO2|C batteries. *Journal of Power Sources*, 293:57–64, October 2015. ISSN 03787753. DOI: 10.1016/j.jpowsour.2015.05.047.

[108] Jean-Marcel Atebamba, Joze Moskon, Stane Pejovnik, and Miran Gaberscek. On the Interpretation of Measured Impedance Spectra of Insertion Cathodes for Lithium-Ion Batteries. *Journal of The Electrochemical Society*, 157(11):A1218, 2010. ISSN 00134651. DOI: 10.1149/1.3489353.

[109] Manan Pathak, Matthew D. Murbach, Chintan Pathak, Tae-Jin Jang, Yanbo Qi, Daniel T. Schwartz, and Venkat R. Subramanian. Fast Impedance Simulation of

Lithium-Ion Batteries with Pseudo-Two Dimensional Electrochemical Models. *Journal of The Electrochemical Society*, 165(7):A1324–A1337, January 2018. ISSN 0013-4651, 1945-7111. DOI: 10.1149/2.0831805jes.

[110] K. Shah, S. J. Drake, D. A. Wetz, J. K. Ostanek, S. P. Miller, J. M. Heinzel, and A. Jain. Modeling of steady-state convective cooling of cylindrical Li-ion cells. *Journal of Power Sources*, 258:374–381, July 2014. ISSN 0378-7753. DOI: 10.1016/j.jpowsour.2014.01.115.

[111] S. J. Drake, M. Martin, D. A. Wetz, J. K. Ostanek, S. P. Miller, J. M. Heinzel, and A. Jain. Heat generation rate measurement in a Li-ion cell at large C-rates through temperature and heat flux measurements. *Journal of Power Sources*, 285:266–273, July 2015. ISSN 0378-7753. DOI: 10.1016/j.jpowsour.2015.03.008.

[112] Jun-qiu Li, Linlin Fang, Wentong Shi, and Xin Jin. Layered thermal model with sinusoidal alternate current for cylindrical lithium-ion battery at low temperature. *Energy*, 148:247–257, April 2018. ISSN 0360-5442. DOI: 10.1016/j.energy.2018.01.024.

[113] Matthew D. Murbach and Daniel T. Schwartz. Beta release of the ImpedanceAnalyzer (v0.9.0-beta). . DOI: 10.5281/zenodo.1043571.

[114] Matthew D Murbach and Daniel T. Schwartz. Data and code for "Analysis of Li-ion battery electrochemical impedance spectroscopy data: An easy-to-implement approach for physics-based parameter estimation using an open-source tool" (Version v1.0). . DOI: 10.5281/zenodo.1043583.

[115] Vadim F. Lvovich. *Impedance Spectroscopy: Applications to Electrochemical and Dielectric Phenomena*. Wiley, Hoboken, N.J, 2012. ISBN 978-0-470-62778-5.

[116] R. J. Sheppard, B. P. Jordan, and E. H. Grant. Least squares analysis of complex data with applications to permittivity measurements. *Journal of Physics D: Applied Physics*, 3(11):1759, 1970.

[117] Bernard A. Boukamp. A Nonlinear Least Squares Fit procedure for analysis of immittance data of electrochemical systems. *Solid State Ionics*, 20(1):31–44, February 1986. ISSN 0167-2738. DOI: 10.1016/0167-2738(86)90031-7.

[118] John Edward Brough Randles. Kinetics of rapid electrode reactions. *Discussions of the faraday society*, 1:11–19, 1947.

[119] Reports — Most-Cited Articles as of February 1, 2017 – updated monthly. http://jes.ecsdl.org/reports/most-cited.

[120] Ilya M. Sobol'. On the distribution of points in a cube and the approximate evaluation of integrals. *USSR Computational Mathematics and Mathematical Physics*, 7(4):86–112, January 1967. ISSN 00415553. DOI: 10.1016/0041-5553(67)90144-9.

[121] Jon Herman and Will Usher. SALib: An open-source Python library for Sensitivity Analysis. *The Journal of Open Source Software*, 2(9):97, January 2017. ISSN 2475-9066. DOI: 10.21105/joss.00097.

[122] John S. Newman and Karen E. Thomas-Alyea. *Electrochemical Systems*. J. Wiley, Hoboken, N.J, 3rd ed edition, 2004. ISBN 978-0-471-47756-3.

[123] Saurabh Saxena, Christopher Hendricks, and Michael Pecht. Cycle life testing and modeling of graphite/LiCoO2 cells under different state of charge ranges. *Journal of Power Sources*, 327:394–400, September 2016. ISSN 03787753. DOI: 10.1016/j.jpowsour.2016.07.057.

[124] CALCE Battery Group - Data. http://www.calce.umd.edu/batteries/data/.

[125] A. Saltelli, Marco Ratto, Terry Andres, Francesca Campolongo, Jessica Cariboni, Debora Gatelli, Michaela Saisana, and Stefano Tarantola. *Global Sensitivity Analysis: The Primer*. Wiley, New York, NY, 2008. ISBN 978-0-470-05997-5.

[126] A. M. Bizeray, J. H. Kim, S. R. Duncan, and D. A. Howey. Identifiability and Parameter Estimation of the Single Particle Lithium-Ion Battery Model. *IEEE Transactions on Control Systems Technology*, pages 1–16, 2018. ISSN 1063-6536. DOI: 10.1109/TCST.2018.2838097.

[127] Matthew D Murbach, Christopher Hendricks, Wesley A. Beckner, Jerry Chen, Mary Yess, Daniel T Schwartz, David A. C. Beck, Chockkalingam Karuppaiah, Patrick Stanley, S Ramanathan, Steven C. DeCaluwe, Lynza Sprowl, Lok-kun Tsui, Yuanchao Liu, Tridip Das, and Marm Dixit. ECS Data Science Hack Day 2017. https://osf.io/z4xkn/, April 2017.

[128] Jeremy E. Oakley and Anthony O'Hagan. Probabilistic sensitivity analysis of complex models: A Bayesian approach. *Journal of the Royal Statistical Society: Series B (Statistical Methodology)*, 66(3):751–769, 2004. DOI: 10.1111/j.1467-9868.2004.05304.x.

[129] Yanbo Qi, Taejin Jang, Venkatasailanathan Ramadesigan, Daniel T. Schwartz, and Venkat R. Subramanian. Is There a Benefit in Employing Graded Electrodes for Lithium-Ion Batteries? *Journal of The Electrochemical Society*, 164(13):A3196–A3207, January 2017. ISSN 0013-4651, 1945-7111. DOI: 10.1149/2.1051713jes.

[130] Nupur Nikkan Sinha and N. Munichandraiah. The effect of particle size on performance of cathode materials of Li-ion batteries. *Journal of the Indian Institute of Science*, 89 (4):381–392, 2009.

[131] Rui Zhao, Jie Liu, and Junjie Gu. The effects of electrode thickness on the electrochemical and thermal characteristics of lithium ion battery. *Applied Energy*, 139:220–229, February 2015. ISSN 03062619. DOI: 10.1016/j.apenergy.2014.11.051.

[132] Honghe Zheng, Jing Li, Xiangyun Song, Gao Liu, and Vincent S. Battaglia. A comprehensive understanding of electrode thickness effects on the electrochemical performances of Li-ion battery cathodes. *Electrochimica Acta*, 71:258–265, June 2012. ISSN 00134686. DOI: 10.1016/j.electacta.2012.03.161.

[133] M Gaberscek, R Dominko, and J Jamnik. Is small particle size more important than carbon coating? An example study on LiFePO4 cathodes. *Electrochemistry Communications*, 9(12):2778–2783, December 2007. ISSN 13882481. DOI: 10.1016/j.elecom.2007.09.020.

[134] MTI Corporation. LiFePO4 Powder MSDS, October 2017.

[135] Sigma-Aldrich. Product No. 759546: Lithium Iron(II) Phosphate Powder Product Specification, March 2017.

[136] John S. Wang, Ping Liu, Elena Sherman, Mark Verbrugge, and Harshad Tataria. Formulation and characterization of ultra-thick electrodes for high energy lithium-ion batteries employing tailored metal foams. *Journal of Power Sources*, 196(20):8714–8718, October 2011. ISSN 03787753. DOI: 10.1016/j.jpowsour.2011.06.071.

[137] Madhav Singh, Jörg Kaiser, and Horst Hahn. A systematic study of thick electrodes for high energy lithium ion batteries. *Journal of Electroanalytical Chemistry*, 782:245–249, December 2016. ISSN 15726657. DOI: 10.1016/j.jelechem.2016.10.040.

[138] Sheng Shui Zhang. A review on the separators of liquid electrolyte Li-ion batteries. *Journal of Power Sources*, 164(1):351–364, January 2007. ISSN 03787753. DOI: 10.1016/j.jpowsour.2006.10.065.

[139] Pankaj Arora and Zhengming (John) Zhang. Battery Separators. *Chemical Reviews*, 104(10):4419–4462, October 2004. ISSN 0009-2665, 1520-6890. DOI: 10.1021/cr020738u.

[140] Gen Inoue and Motoaki Kawase. Numerical and experimental evaluation of the relationship between porous electrode structure and effective conductivity of ions and electrons in lithium-ion batteries. *Journal of Power Sources*, 342:476–488, February 2017. ISSN 0378-7753. DOI: 10.1016/j.jpowsour.2016.12.098.

[141] Jishi Zhao, Li Wang, Xiangming He, Chunrong Wan, and Changyin Jiang. Kinetic investigation of $LiCOO_2$ by electrochemical impedance spectroscopy (EIS). *Int. J. Electrochem. Sci*, 5:478–488, 2010.

[142] Agnieszka Swiderska-Mocek and Andrzej Lewandowski. Kinetics of Li-ion transfer reaction at LiMn2O4, LiCoO2, and LiFePO4 cathodes. *Journal of Solid State Electrochemistry*, 21(5):1365–1372, May 2017. ISSN 1432-8488, 1433-0768. DOI: 10.1007/s10008-016-3499-6.

[143] Pier Paolo Prosini, Marida Lisi, Daniela Zane, and Mauro Pasquali. Determination of the chemical diffusion coefficient of lithium in LiFePO 4. *Solid State Ionics*, 148(1): 45–51, 2002. DOI: https://doi.org/10.1016/S0167-2738(02)00134-0.

[144] M. D. Levi, G. Salitra, B. Markovsky, H. Teller, D. Aurbach, Udo Heider, and Lilia Heider. Solid-State Electrochemical Kinetics of Li-Ion Intercalation into $Li_{1-x}CoO_2$: Simultaneous Application of Electroanalytical Techniques SSCV, PITT, and EIS. *Journal of The Electrochemical Society*, 146(4):1279–1289, 1999. DOI: 10.1149/1.1391759.

[145] Elmar Plischke, Emanuele Borgonovo, and Curtis L. Smith. Global sensitivity measures from given data. *European Journal of Operational Research*, 226(3):536–550, May 2013. ISSN 0377-2217. DOI: 10.1016/j.ejor.2012.11.047.

[146] J. Song and M. Z. Bazant. Effects of Nanoparticle Geometry and Size Distribution on Diffusion Impedance of Battery Electrodes. *Journal of the Electrochemical Society*, 160 (1):A15–A24, November 2012. ISSN 0013-4651, 1945-7111. DOI: 10.1149/2.023301jes.

[147] Eric Jones, Travis Oliphant, Pearu Peterson, and others. SciPy: Open source scientific tools for Python. 2001. DOI: http://www.scipy.org/.

[148] G. Paasch, K. Micka, and P. Gersdorf. Theory of the electrochemical impedance of macrohomogeneous porous electrodes. *Electrochimica Acta*, 38(18):2653–2662, December 1993. ISSN 0013-4686. DOI: 10.1016/0013-4686(93)85083-B.

[149] Matthew D. Murbach and D. T. Schwartz. Initial release of ImpedanceAnalyzer-manuscript (v1.0). . DOI: 10.5281/zenodo.1043583.

[150] Lars Buitinck, Gilles Louppe, Mathieu Blondel, Fabian Pedregosa, Andreas Mueller, Olivier Grisel, Vlad Niculae, Peter Prettenhofer, Alexandre Gramfort, Jaques Grobler, Robert Layton, Jake Vanderplas, Arnaud Joly, Brian Holt, and Gaël Varoquaux. API design for machine learning software: Experiences from the scikit-learn project. *arXiv:1309.0238 [cs]*, September 2013.

[151] M. Broussely, Ph. Biensan, F. Bonhomme, Ph. Blanchard, S. Herreyre, K. Nechev, and R. J. Staniewicz. Main aging mechanisms in Li ion batteries. *Journal of Power Sources*, 146(1):90–96, August 2005. ISSN 0378-7753. DOI: 10.1016/j.jpowsour.2005.03.172.

[152] J. Vetter, P. Novák, M.R. Wagner, C. Veit, K.-C. Möller, J.O. Besenhard, M. Winter, M. Wohlfahrt-Mehrens, C. Vogler, and A. Hammouche. Ageing mechanisms in lithium-ion batteries. *Journal of Power Sources*, 147(1-2):269–281, September 2005. ISSN 03787753. DOI: 10.1016/j.jpowsour.2005.01.006.

[153] Zhe Li, Jun Huang, Bor Yann Liaw, Viktor Metzler, and Jianbo Zhang. A review of lithium deposition in lithium-ion and lithium metal secondary batteries. *Journal of Power Sources*, 254:168–182, May 2014. ISSN 03787753. DOI: 10.1016/j.jpowsour.2013.12.099.

[154] Simon F. Schuster, Tobias Bach, Elena Fleder, Jana Müller, Martin Brand, Gerhard Sextl, and Andreas Jossen. Nonlinear aging characteristics of lithium-ion cells under different operational conditions. *Journal of Energy Storage*, 1:44–53, June 2015. ISSN 2352-152X. DOI: 10.1016/j.est.2015.05.003.

[155] US DOE EERE. Enabling Fast Charging: A Technology Gap Assessment. Technical Report INL/EXT–17-41638, 1416167, October 2017.

[156] Mathias Petzl and Michael A. Danzer. Nondestructive detection, characterization, and quantification of lithium plating in commercial lithium-ion batteries. *Journal of Power Sources*, 254:80–87, May 2014. ISSN 03787753. DOI: 10.1016/j.jpowsour.2013.12.060.

[157] Thomas Waldmann, Marcel Wilka, Michael Kasper, Meike Fleischhammer, and Margret Wohlfahrt-Mehrens. Temperature dependent ageing mechanisms in Lithium-ion batteries – A Post-Mortem study. *Journal of Power Sources*, 262:129–135, September 2014. ISSN 0378-7753. DOI: 10.1016/j.jpowsour.2014.03.112.

[158] L. Somerville, J. Bareño, S. Trask, P. Jennings, A. McGordon, C. Lyness, and I. Bloom. The effect of charging rate on the graphite electrode of commercial lithium-ion cells: A post-mortem study. *Journal of Power Sources*, 335:189–196, December 2016. ISSN 0378-7753. DOI: 10.1016/j.jpowsour.2016.10.002.

[159] Qianqian Liu, Chunyu Du, Bin Shen, Pengjian Zuo, Xinqun Cheng, Yulin Ma, Geping Yin, and Yunzhi Gao. Understanding undesirable anode lithium plating issues in lithium-ion batteries. *RSC Advances*, 6(91):88683–88700, September 2016. ISSN 2046-2069. DOI: 10.1039/C6RA19482F.

[160] C. Uhlmann, J. Illig, M. Ender, R. Schuster, and E. Ivers-Tiffée. In situ detection of lithium metal plating on graphite in experimental cells. *Journal of Power Sources*, 279: 428–438, April 2015. ISSN 03787753. DOI: 10.1016/j.jpowsour.2015.01.046.

[161] M. C. Smart and B. V. Ratnakumar. Effects of electrolyte composition on lithium plating in lithium-ion cells. *Journal of The Electrochemical Society*, 158(4):A379–A389, 2011. DOI: 10.1149/1.3544439.

[162] Thomas Waldmann, Björn-Ingo Hogg, and Margret Wohlfahrt-Mehrens. Li plating as unwanted side reaction in commercial Li-ion cells – A review. *Journal of Power Sources*, 384:107–124, April 2018. ISSN 0378-7753. DOI: 10.1016/j.jpowsour.2018.02.063.

[163] Stefan Schindler, Marius Bauer, Mathias Petzl, and Michael A. Danzer. Voltage relaxation and impedance spectroscopy as in-operando methods for the detection of lithium plating on graphitic anodes in commercial lithium-ion cells. *Journal of Power Sources*, 304:170–180, February 2016. ISSN 03787753. DOI: 10.1016/j.jpowsour.2015.11.044.

[164] Carlos Pastor-Fernández, Kotub Uddin, Gael H. Chouchelamane, W. Dhammika Widanage, and James Marco. A Comparison between Electrochemical Impedance Spectroscopy and Incremental Capacity-Differential Voltage as Li-ion Diagnostic Techniques to Identify and Quantify the Effects of Degradation Modes within Battery Management Systems. *Journal of Power Sources*, 360:301–318, August 2017. ISSN 03787753. DOI: 10.1016/j.jpowsour.2017.03.042.

[165] Ran Tao, Xuanxuan Bi, Shu Li, Ying Yao, Feng Wu, Qian Wang, Cunzhong Zhang, and Jun Lu. Kinetics Tuning the Electrochemistry of Lithium Dendrites Formation in Lithium Batteries through Electrolytes. *ACS Applied Materials & Interfaces*, 9(8): 7003–7008, March 2017. ISSN 1944-8244, 1944-8252. DOI: 10.1021/acsami.6b13859.

[166] Mark W. Verbrugge and Brian J. Koch. Microelectrode investigation of ultrahigh-rate lithium deposition and stripping. *Journal of Electroanalytical Chemistry*, 367(1-2): 123–129, 1994. DOI: 10.1016/0022-0728(93)03047-S.

CV

Matthew D. Murbach

Last update on August 16, 2018

mmurbach@uw.edu • www.mattmurbach.com • orcid.org/0000-0002-6583-5995

Education

University of Washington — Seattle, Washington
Ph.D. in Chemical Engineering + Adv. Data Science Option — *2013 – present*
Thesis: *Linear and Nonlinear Electrochemical Impedance Spectroscopy for Lithium-ion Batteries*
Advisor: Professor Daniel T. Schwartz
Committee: Prof. David Beck, Prof. Venkat Subramanian, and Prof. Devin MacKenzie

University of California, San Diego — La Jolla, California
B.S. in Chemical Engineering — *Cum Laude* — *2009 – 2013*

Research Interests

(Nonlinear) Electrochemical Impedance Spectroscopy, Lithium-ion batteries, Model Validation, Physics-based modeling, Reproducibility, Open Data and Analysis

Awards and Honors

- **2018 Lawrence Award**, UW Chemical Engineering — *June 2018*
- **2018 CEI Clean Energy Prize**, Environmental Innovation Challenge — *March 2018*
- **Forbes' 30 Under 30 2018: Energy**, Forbes — *November 2017*
- **Best Clean Energy Research Poster**, UW Graduate Student Symposium — *September 2016*
- **"Judges Also Really Liked" Award**, Environmental Innovation Challenge — *April 2016*
- **Student Training and Exploration Grant**, UW Clean Energy Institute — *October 2015*
- **Popular Vote Best Poster Award**, UW Graduate Student Symposium — *September 2015*
- **Honorable Mention**, Environmental Innovation Challenge — *April 2015*
- **Data Science IGERT Fellowship**, US National Science Foundation — *August 2014*
- **GAANN Fellowship**, US Department of Education — *March 2014*
- **Clean Energy Institute Fellowship**, UW Clean Energy Institute — *December 2013*
- **Huppert Memorial Outstanding Senior**, UCSD Chemical Engineering — *June 2013*

Publications and Presentations

Peer-Reviewed Journals

J5. **M. D. Murbach**,[=] V. W. Hu,[=] and D. T. Schwartz. Nonlinear electrochemical impedance spectroscopy of lithium-ion batteries: Experimental approach, analysis, and initial findings. Journal of The Electrochemical Society (accepted, 2018).

J4. M. Pathak, **M. D. Murbach**, C. Pathak, T. Jang, Y. Qi, D. T. Schwartz, and V. R. Subramanian. Fast Impedance Simulation of Lithium-Ion Batteries with Pseudo-Two Dimensional Electrochemical Models. Journal of The Electrochemical Society 165, A1324–A1337 (2018). doi: 10.1149/2.0831805jes.

J3. **M. D. Murbach** and D. T. Schwartz. Analysis of Li-ion battery electrochemical impedance spectroscopy data: An easy-to-implement approach for physics-based parameter estimation using an open-source tool. Journal of The Electrochemical Society 165, A297–A304 (2018). doi: 10.1149/2.1021802jes.

J2. **M. D. Murbach** and D. T. Schwartz. Extending Newman's Pseudo-Two-Dimensional Lithium-Ion Battery Impedance Simulation Approach to Include the Nonlinear Harmonic Response. Journal of The Electrochemical Society 164, E3311–E3320 (2017). doi: 10.1149/2.0301711jes.

J1. M. R. Sarker, **M. D. Murbach**, D. T. Schwartz and M. A. Ortega-Vazquez. Optimal Operation of a Battery Energy Storage System: Trade-off between Grid Economics and Storage Health. Electric Power Systems Research 152, 342–349 (2017). doi: 10.1016/j.epsr.2017.07.007.

Peer-Reviewed Journals (in preparation)

J6. **M. D. Murbach** and D. T. Schwartz. Evaluating linear and nonlinear equivalent circuit models for lithium-ion batteries using the pseudo-two-dimensional model.

Patents

P1. **M. D. Murbach** and D. T. Schwartz, Electrochemical cell diagnostic systems and methods using second order and higher harmonic components, US App. No. PCT/US2016/022119, filed on March 11, 2016.

Oral Presentations

C8. **M. D. Murbach** and D. T. Schwartz, "Data science tools for the physics-based analysis of lithium-ion battery impedance spectra", UW Chemical Engineering Department Seminar (Seattle, WA) February 2018

C7. **M. D. Murbach**, V. W. Hu, and D. T. Schwartz, "The Impedance Analyzer: An Open-Source, Web-Based Tool for Sophisticated Interrogation of Experimental EIS Spectra.", 232nd Electrochemical Society Meeting (National Harbor, MD) October 2017

C6. **M. D. Murbach** and D. T. Schwartz, "A data science approach to lithium-ion battery impedance measurements.", 10^{th} ChemE Graduate Student Symposium (Seattle, WA) September 2017

C5. **M. D. Murbach** and D. T. Schwartz, "Commercializing battery management and diagnostics: From UW research to clean tech startup.", 2+2 Clean Energy Forum (Chengdu, Sichuan, China) September 2017

C4. **M. D. Murbach** and D. T. Schwartz, "Unlocking Insights into Battery Systems: A Data Science Approach to Impedance Analysis.", 231st Electrochemical Society Meeting (New Orleans, LA) May 2017

C3. **M. D. Murbach** and D. T. Schwartz, "Data Science Tools for Incorporating Physics-Based Models into Analysis of Impedance Spectra.", 231st Electrochemical Society Meeting (New Orleans, LA) May 2017

C2. **M. D. Murbach** and D. T. Schwartz, "Linear and Nonlinear Electrochemical Impedance Spectroscopy: A Data Science Perspective.", 230th Electrochemical Society Meeting (Honolulu, HI) October 2016

C1. **M. D. Murbach** and D. T. Schwartz, "Probing Nonlinear Dynamics to Unlock New Insights into Battery Systems.", 229th Electrochemical Society Meeting (San Diego, CA) May 2016

Teaching and Mentorship

Teaching Assistant, University of Washington *Winter and Spring 2015*

CHEM E 497: Special Projects in Chemical Engineering Design

- Undergraduate special senior design course using Chemical Engineering principles to design businesses and products by commercializing lab research.
- Prepared and taught weekly lectures, mentored students in lab research, organized group meetings, evaluated coursework and research progress, and led teams participating in multiple UW business plan competitions. Directly mentored 4 students (16 total).

Additional Undergraduate Researchers Mentored at UW:

- Matthew Canin (Undergraduate, University of Washington) *Summer 2017*
- Stephanie Reusch (Undergraduate, University of Washington) *Fall 2015–Spring 2017*
- Cleo Tsang (Undergraduate, Cornell University) *Summer 2016*
- Alek Lazarski (Undergraduate, University of Texas, El Paso) *Summer 2016*

Undergraduate Assistant, UC San Diego *2012 – 2013*

ENG 100D and 100L: Global TIES Design for Development and Lab

- Interdisciplinary humanitarian engineering course and labs focused on designing, building, testing, and delivering solutions to real-world problems experienced by nonprofit clients and the communities they serve around the world.
- Organized weekly meetings (K-12 Environmental Education and One Village Philippines teams), co-ordinated with clients, and evaluated coursework and presentations.

Outreach and Service

Co-organizer, Electrochemical Society Data Science Hack Week *May 2018*

- ECS Hack Week was a week-long event at the 233rd ECS Meeting in Seattle, WA focused on building an electrochemical data sciences and open source community through a mix of introductory and advanced tutorials as well as open-source project "hacking" to create new tools and data sets. (OSF Page)
- Organized invited speakers, ran attendee application and selection, and developed Python and Open Science curriculum.

Instructor, Software Carpentry *May 2018 – present*

Co-organizer, Electrochemical Society Hack Day 2017 *October 2017*

- Co-organized the inaugural day-long data science event where 30 participants came together from a wide variety of backgrounds to learn open science, reproducibility, and programming skills and "hack" together on open source projects that benefit the electrochemical community.

Founding Chair, ECS@UW (Electrochemical Society Student Chapter) *2015 – 2017*

- Started an ECS student chapter at the UW with the mission of bringing together students, postdocs, and faculty interested in electrochemistry and solid-state science across campus.
- Organized biweekly educational meetings where students teach students, professional development events to help students prepare for academic and non-academic jobs, as well as "Enginearrings" demonstrations to increase excitement in STEM at local science fairs.

Organizer, UW Distinguished Young Seminar Speaker Program *Summer 2015*

Outreach Committee + Webmaster, (ACES) Assoc. of ChemE Grad Students *2014 – 2016*

- Coordinated exhibits at UW Engineering Discovery Days to introduce young students to the fun of science and engineering
- Redesigned and maintained the ACES website and e-mail accounts

---

Additional Memberships

Diversity in Clean Energy • Women in Chemical Engineering • The Electrochemical Society • Materials Research Society | UW Chapter